Particle acceleration in plasmas: non-linear wakefields for leptons and magnetic vortices for spin-polarized protons

Inaugural-Dissertation

zur Erlangung des Doktorgrades
der Mathematisch-Naturwissenschaftlichen Fakultät
der Heinrich-Heine-Universität Düsseldorf

vorgelegt von

Lars Reichwein
aus Düsseldorf

Düsseldorf, August 2022

aus dem Institut für Theoretische Physik I
der Heinrich-Heine-Universität Düsseldorf

Gedruckt mit Genehmigung der
Mathematisch-Naturwissenschaftlichen Fakultät der
Heinrich-Heine-Universität Düsseldorf

Berichterstatter:

1. Prof. Dr. Alexander Pukhov

2. Prof. Dr. Dr. Carsten Müller

3. Prof. Dr. Olga Rosmej

Tag der mündlichen Prüfung: 10.11.2022

Abstract

Plasma-based accelerators are considered a promising alternative to large and expensive conventional accelerator structures since the higher field strengths that can be applied allow for more compact designs. This is of high interest since research in fundamental physics requires high energies for e.g. the discovery of new particles. Still, a lot of research must be performed in order to make these setups competitive in areas like energy, charge and general beam quality.

In the first part of this thesis, we investigate the so-called wakefield acceleration for leptons where a particle beam or a laser pulse drives a plasma wave that has accelerating and focusing fields for electrons. Within this part, we develop new models for the description of the cavities in wakefield acceleration that better incorporate properties of the longitudinal electric field, and that are self-consistent. Positron acceleration is generally more problematic, as their opposite charge renders the field regions used for electron wakefield acceleration useless. We present a setup driven by both a particle and a laser beam which allows for the acceleration of positron rings. The proposed setup is investigated using both analytical methods as well as particle-in-cell simulations. Besides the more general wakefield investigations, we also look into the inner structure of the accelerated electron beam in the case of finite emittance. Lastly for this chapter, we examine the influence of structured plasma in the form of clustered Hydrogen on the acceleration mechanisms in laser-plasma interaction.

In the second part of this thesis, we study the acceleration of protons by Magnetic Vortex Acceleration. More specifically, we examine the acceleration of spin-polarized particle beams that are of interest i.a. for probing the nuclear structure of the proton or polarized fusion. We start by studying the influence of a density-down ramp at the end of the plasma target with which the laser pulse interacts on beam quality. Finally, we present a setup consisting of two laser pulses propagating side-by-side that yields better spin polarization and beam quality compared to a single-pulse setup.

Zusammenfassung

Plasma-basierte Beschleuniger werden als aussichtsreiche Alternative zu großen und kostenintensiven herkömmlichen Beschleunigern angesehen, da die höheren Feldstärken, die genutzt werden können, kompaktere Designs erlauben. Dies ist von großem Interesse, da Forschung in der Fundamentalphysik hohe Energien erfordert, z.B. für die Entdeckung neuer Teilchen. Dennoch muss weiterhin viel Forschung betrieben werden um die Aufbauten in Punkten wie Energie, Ladung und genereller Strahlqualität wettbewerbsfähig zu machen.

Im ersten Teil dieser Arbeit untersuchen wir die sogenannte Wakefield-Beschleunigung für Leptonen, bei der ein Teilchen-Strahl oder ein Laserpuls eine Plasmawelle antreibt, welche beschleunigende und fokussierende Felder für Elektronen aufweist. In diesem Teil entwickeln wir neue Modelle zur Beschreibung der Kavitäten in der Wakefield-Beschleunigung, welche die Eigenschaften des longitudinalen elektrischen Feldes besser erfassen, und die selbst-konsistent sind. Positronen-Beschleunigung ist generell problematischer, da ihre entgegengesetzte Ladung die für Elektronen-Wakefieldbeschleunigung genutzten Feldregionen unbrauchbar macht. Wir präsentieren einen Aufbau, welcher durch sowohl einen Teilchen- als auch einen Laserstrahl angetrieben wird, und die Beschleunigung von Positronen-Ringen ermöglicht. Dieser Aufbau wird sowohl mithilfe analytischer Methoden als auch mit Particle-in-cell-Simulationen untersucht. Neben den eher generellen Untersuchungen zum Wakefield betrachten wir auch die innere Struktur des beschleunigten Elektronenstrahls im Fall endlicher Emittanz. Schließlich erforschen wir den Einfluss strukturierten Plasmas in Form von Wasserstoff-Clustern auf die Beschleunigungsmechanismen in der Laser-Plasma-Wechselwirkung in diesem Kapitel.

Im zweiten Teil dieser Arbeit studieren wir die Beschleunigung von Protonen mittels Magnetic Vortex Acceleration. Genauer untersuchen wir die Beschleunigung spin-polarisierter Teilchenstrahlen, die u.a. für die Erforschung der nuklearen Struktur des Protons oder für polarisierte Fusion von Interesse sind. Wir beginnen mit der Untersuchung des Effekts, den Dichtegradienten am Ende des Plasma-Targets, mit dem der Laser wechselwirkt, auf die Strahlqualität haben. Schließlich präsentieren wir einen Aufbau, welcher aus zwei nebeneinander propagierenden Laserpulsen besteht, und bessere Spin-Polarisation und Strahlqualität liefert als ein Ein-Puls-Setup.

Contents

Chapter 1

Introduction

The field of particle physics continually requires the acceleration of particles to high energies. Collisions of such particle beams with a second, counter-propagating particle beam can induce the creation of secondary particles in order to test the Standard Model of particle physics [1]. Current accelerator structures like the Stanford Linear Collider (SLAC) or the Large Hadron Collider (LHC) at CERN are huge in size and expensive [2, 3]. The reason for their size is the mechanism for particle acceleration. When wanting to accelerate particles to even higher energies, two options are available, the first being to increase the strength of the electric field. For a specific material only a certain field strength may be applied before breakdown occurs. Then, longer acceleration distances are required. The radiofrequency-based accelerators are limited to field strengths in the vicinity of a couple 100 MV/m [4, 5]. As the creation of heavier particles requires higher energy, future plans for circular accelerators (and similarly linear accelerators) would need to be significantly larger than the 27 km circumference of the LHC.

It is, however, possible to perform particle acceleration also in plasma, a state of matter where the electrons are separated from the nuclei. This has the advantage that fields orders of magnitude stronger than achievable in conventional accelerators can be applied (approx. 100 GV/m), allowing for much shorter accelerator designs [6].

In the case of electron acceleration, one prominent mechanism is the so-called laser-driven plasma wakefield acceleration (LWFA). It was first proposed by Tajima and Dawson in 1979 in the form that a high intensity laser pulse expels electrons due to its ponderomotive force and induces a plasma wave [7]. Electrons can be injected and trapped by the plasma wave. Due to the prevalent fields, the electrons can be accelerated to high energies. Back then, the required laser intensity could not be obtained from a single pulse. Thus, setups like beatwave acceleration were suggested that use the interaction of two pulses with one another [8]. This has changed significantly with the advent of chirped-pulse amplification [9] which paved the way for higher-intensity lasers that are available today. Another

option is using a particle driver instead of the laser pulse. This particle beam-driven plasma wakefield acceleration (PWFA) similarly benefits from the excitation of a plasma wave due to the driver propagating through the plasma [10].

Over the years, the two schemes have been investigated both experimentally and theoretically. Depending on the intensity of the laser (or the density of the driving beam) the wakefield can reach a non-linear regime [11]. In particular, the laser-plasma parameters can be chosen in such a fashion that an almost spherical cavity void of electrons is formed. This is called the "bubble regime". In the regime it was shown that the energy spectrum of the accelerated electrons is quasi-monoenergetic and that the bubble can propagate over several Rayleigh lengths [12–14]. Similarly, for PWFAs the "blowout" regime was found which is subject to on-going research as well [15, 16].

Both of the wakefield schemes still need to be further optimized, however, to be competitive to facilities like SLAC and LHC. Currently, the record energy achieved using wakefield acceleration is 8 GeV [17]. Besides the maximum energy, several other aspects are in need of improvement: not only should the electron bunch be of high energy, but it should also have the desired charge [18] and be of high quality in the sense that momentum spread of the particles is minimized. For this reason, several alterations of the wakefield mechanism have been proposed.

One example is the method of density down-ramp injection where the change in plasma wave velocity in a density gradient is used for improved injection into the wake [19]. Another interesting mechanism is the so-called Trojan Horse Acceleration [20]. There, a particle driver first excites a wakefield. Using a laser pulse, atoms inside the cavity can be ionized. The ionized electrons are "born" directly in the blowout and therefore have lower momentum spread (i.e. ultra-low emittance in the range of μm mrad).

Another area of active research is the acceleration of ions from laser-plasma interaction [21, 22]. As ions are significantly heavier than the leptonic electrons, different mechanisms for acceleration have to be employed due to the generally higher required field strength. In the near future, facilities like ELI [23] or XCELS [24], that promise currently unparalleled laser intensities, should significantly push this area of research forward. More specifically, the acceleration of spin-polarized ion (and also electron) beams is interesting for several reasons. This includes probing the nuclear proton structure [25] as well as fusion. For the latter it has been shown in [26] that polarizing the particles can improve upon the cross section for fusion. While for conventional circular accelerators polarization can be built up over time via the Sokolov-Ternov effect [27], different methods must be used to obtain spin-polarized beams from laser-plasma interaction due to the shorter time scale. The plasma target needs to be pre-polarized for which setups using a ^{3}He or an HCl target have been proposed [28, 29]. The Helium target has been built at Forschungszentrum

Jülich and has been first tested at the end of 2021 at GSI Darmstadt; the results are currently still being evaluated. More work, both theoretically and experimentally, needs to be done here to optimize the setups for spin-polarization, energy and general beam quality as currently researchers are essentially limited to gaseous targets. This rules out several common methods of ion acceleration that utilize solid-state targets [30, 31] and leaves them with schemes like Magnetic Vortex Acceleration [32, 33]. In particular, the laser fields can induce strong depolarization of the particle beam which is why research concerning the optimization of these setups is important.

The present thesis is essentially divided into two parts with respect to acceleration mechanism. The first part is concerned with wakefield acceleration of leptons, specifically models describing the structure of highly non-linear blowouts for electrons, as well as the acceleration of positrons. In the second part, we investigate the acceleration of spin-polarized proton beams using Magnetic Vortex Acceleration and propose a setup using two laser pulses for improved results.

1.1 Outline

In the following chapter we will give a rough theoretical basis for the work throughout this thesis. This includes some basic theory regarding plasma physics, with the focus lying on wakefield acceleration and ion acceleration. In chapter 3 we then will introduce the basic notion of particle-in-cell (PIC) simulations which are a valuable tool when – as it is often the case for these schemes – analytical theory is not sufficient. After that, we will present the results for our works concerning electron and positron acceleration in chapter 4. In particular, we will further develop the analytical models that describe the boundary of the cavity in beam-driven wakefield acceleration as well as an laser-augmented blowout structure which gives us an option to accelerate positrons. The microscopic structure of the accelerated electron bunch is also discussed. Lastly, we investigate the role of clusterized targets for electron acceleration in the scope of an experimental collaboration.

In chapter 5, we then go over to the acceleration of ion beams. More specifically, we study the acceleration of spin-polarized beams from Magnetic Vortex Acceleration (MVA). Here, we investigate the effect of density down-ramps on beam quality, and present a setup consisting of two laser pulses which greatly improves upon single-pulse MVA.

The general results of this thesis are summarized in chapter 6.

1.2 List of publications

Over the course of the PhD studies, the following publications were authored or co-authored by the author.

1.2.1 Publications in peer-reviewed journals

The publications in this subsection have passed a peer-review process. The specific contributions are given at the end of the summary of each chapter.

1. L. Reichwein, J. Thomas, and A. Pukhov, *Finite-emittance Wigner crystals in the bubble regime*, Laser Part. Beams **38**(3), pp. 176-180 (2020).

2. L. Reichwein, J. Thomas, A. A. Golovanov, I. Yu. Kostyukov, and A. Pukhov, *Fixing E-field divergence in strongly non-linear wakefields in homogeneous plasma*, Plasma Phys. Control. Fusion **62**, 115017 (2020).

3. A. A. Golovanov, I. Yu. Kostyukov, L. Reichwein, J. Thomas, and A. Pukhov, *Excitation of strongly nonlinear plasma wakefield by electron bunches*, Plasma Phys. Control. Fusion **63**, 085004 (2021).

4. L. Reichwein, A. Hützen, M. Büscher, and A. Pukhov, *On the robustness of spin polarization for magnetic vortex accelerated proton bunches in density down-ramps*, Plasma Phys. Control. Fusion **63**, 085011 (2021).

5. B. Aurand, L. Reichwein, K. Schwind, E. Aktan, M. Cerchez, V. Kaymak, L. Lessmann, R. Prasad, J. Thomas, T. Toncian, A. Khoukaz, A. Pukhov, and O. Willi, *Spatial profile of accelerated electrons from ponderomotive scattering in hydrogen cluster targets*, New J. Phys. **24**, 033006 (2022).

6. L. Reichwein, A. Golovanov, I. Yu. Kostyukov, and A. Pukhov, *Positron acceleration via laser-augmented blowouts in two-column plasma structures*, Phys. Rev. E **105**, 055207 (2022).

1.2.2 Preprints

Further, the following publication has recently been accepted.

7. L. Reichwein, M. Büscher, and A. Pukhov, *Acceleration of spin-polarized proton beams via two parallel laser pulses*, arXiv:2201.11534 (2022), accepted at Phys. Rev. Accel. Beams.

1.2.3 Proceedings

The following proceedings have been published/submitted:

8. L. Reichwein, A. Pukhov, and J. Thomas, *Wigner crystals in the bubble regime of wakefield acceleration*, News and reports from High Energy Density generated by heavy ion and laser beams : 2019, p. 42 (2021).

9. L. Reichwein, A. Hützen, M. Büscher, and A. Pukhov, *Spin-Polarized Particle Beams from Laser-Plasma Based Accelerators*, J. Phys.: Conf. Ser. **2249**, 012018 (2022).

10. L. Reichwein, M. Filipovic, X. F. Shen, K. Jiang, C. Baumann, and A. Pukhov, *Interaction of Extremely Intense Flows of Electromagnetic Energy and QED Processes in Supercritical Fields*, accepted for the NIC Series (2022).

11. L. Reichwein, A. Soloviev, and A. Pukhov, *Acceleration of spin-polarized proton beams from a dual-laser pulse setup*, submitted for the EPS Plasma Conference 2022 (2022).

For all of these proceedings based on the previously listed articles, L.R. has been the main author. The publication concerning QED processes is a summary of the group's results within a granting period of a computational project at the facility JUWELS. Thus, the contents of this publication are based on the results of many authors, as are the figures.

Chapter 2

General theory

Within this chapter we introduce the theoretical foundation necessary for the work following in later chapters. We start by describing relevant aspects of the state of plasma as well as laser pulses. With both of these described, we go over to the description of excited plasma waves, more specifically wakefields that are either driven by laser pulses or particle beams used for electron acceleration. Lastly, we introduce the mechanism of Magnetic Vortex Acceleration as an example of an ion acceleration scheme which is studied in the second part of the thesis. Throughout this chapter (and the following), we will be using the cgs system of units.

2.1 Plasma

Plasma is often called the "fourth state of matter". Fundamentally, this state is reached once passing the critical point of a certain material. In this state, the matter is – either partially or fully – ionized. This leads to a plethora of effects that make plasma worth studying in the scope of accelerator physics.

The first thing to consider is the effect of the so-called *Debye shielding*. A single, point-like particle of charge q will attract particles of opposing charge in a plasma due to the fact that, in a plasma, the electrons are not bound to the nuclei as they would be in the gaseous state. This will lead to the test-particles potential being shielded.

To describe this shielding [34], we start from the Poisson equation for the potential ϕ

$$\nabla^2\phi = -4\pi(q\delta(\mathbf{r}) + e(n_p - n_e)) \,, \tag{2.1}$$

where e is the elementary charge. The densities n_p and n_e denote the proton and electron density, respectively. The delta distribution $\delta(\mathbf{r})$ describes the point-like density of the

test particle. We assume that the electrons obey a Boltzmann distribution

$$n_e = n_0 \exp\left(\frac{e\phi}{k_B T}\right) \tag{2.2}$$

with n_0 being the unperturbed plasma density, k_B as Boltzmann's constant and T as the electron temperature. If the argument of the exponential function is small, we may Taylor expand in ϕ, leading to the rephrased Poisson problem

$$\left(\nabla^2 - \frac{1}{\lambda_D^2}\right)\phi = -4\pi q\delta(\mathbf{r}) \ . \tag{2.3}$$

Here,

$$\lambda_D = \sqrt{\frac{k_B T}{4\pi n_0 e^2}} \tag{2.4}$$

is the *Debye length*. The solution to the Poisson equation obtained from a Fourier transform thus is

$$\phi = \frac{q}{r}\exp\left(-\frac{r}{\lambda_D}\right) \ . \tag{2.5}$$

Two things must be noted here: firstly, the potential in plasma drops off quicker than the normal Coulomb potential, where $\phi \propto r^{-1}$. The Debye length is the characteristic length at which the potential has dropped off to $1/e$ of the normal Coulomb potential. Secondly, in order for shielding to occur, we must require that a lot of particles are present in the plasma. This is often written in form of the condition that the number of particles in the Debye sphere must be large, i.e. $N_D \gg 1$. Plasma therefore requires a lot of particles in order to be actually considered a plasma. Further, plasma exhibits charge differences at microscopic scales, whereas in the macroscopic picture, it would seem electrically neutral. For this reason, plasma is also called *quasi-neutral*.

Another important effect in plasma are oscillations. If we imagine that we displace a slab of electrons with respect to the ions, we induce an electric field. Without any additional applied forces, the electrons will swing back due to the ions' restoring force, thus leading to oscillatory behaviour. The characteristic frequency, the plasma frequency, can be defined with the help of the thermal velocity of the electrons,

$$v_{\text{th}} = \sqrt{\frac{k_B T}{m_e}} \ . \tag{2.6}$$

Dividing the thermal velocity by the previously derived Debye length, we obtain the

plasma frequency

$$\omega_p = \frac{v_{\text{th}}}{\lambda_D} = \sqrt{\frac{4\pi n_0 e^2}{m_e}} \,. \tag{2.7}$$

More precisely, this is the *electron* plasma frequency. Similarly, we could define an ion plasma frequency, but in the following, most of the time only the electron frequency is of interest due to the time scale of the processes at hand. We will therefore simply refer to it as "the plasma frequency".
Before going into plasma waves, we will first recapitulate properties of laser pulses as they are one of the possible drivers for such waves.

2.2 Laser pulses

The second ingredient for the later investigated laser-plasma interaction are laser pulses. While we will not cover the most basic laser theory here (see, e.g., the book by Svelto for that [35]), we need to introduce certain aspects of laser pulses that will become relevant within the scope of our research here.
Laser pulses (or rather, their electric field $\mathbf{E}$) fulfill the *wave equation* in vacuum [36],

$$\nabla^2 \mathbf{E} - \frac{1}{c^2}\frac{\partial^2 \mathbf{E}}{\partial t^2} = 0 \,. \tag{2.8}$$

In the paraxial ray approximation it is assumed that the phase of the wave mainly varies in the direction of propagation (here: z). Further assuming that our beam has cylinder symmetry, the wave equation can be rephrased as

$$\frac{\partial^2 E}{\partial r^2} + \frac{1}{r}\frac{\partial E}{\partial r} - 2ik\frac{\partial E}{\partial z} = 0 \,. \tag{2.9}$$

Here, r denotes the radial coordinate and k the wave number. One possible solution is that of a *Gaussian beam* with

$$E(r,z) = E_0 \frac{w_0}{w} \exp\left[\frac{-r^2}{w^2} - \frac{i\pi r^2}{\lambda_L R} + i\phi_0\right] \,, \tag{2.10}$$

E_0 being the peak electric field. The parameter

$$w = w_0 \sqrt{1 + \left(\frac{z}{z_R}\right)^2} \tag{2.11}$$

is the beam waist. As visible from the equation, we have a focused beam, i.e. w is

the smallest at $z = 0$. There it reaches the *focal spot size* w_0, which is one of the most commonly used parameters to characterize the capabilities of a laser system. How quickly the pulse widens depends on the *Rayleigh length* $z_R = \pi w_0^2/\lambda_L$, where λ_L is the laser wavelength. The choice of the Rayleigh length will become important in a later part of our studies (cf. section 4.8). Another important parameter is the *radius of curvature*, $R = (z^2 + z_R^2)/z$. The last parameter of the Gaussian beam is the *Gouy phase* $\tan(\phi_0) = \lambda_L z/(\pi w_0^2)$. Besides Gaussian beams there are several other solutions to the wave equation, for example Laguerre-Gaussian modes [37], which can prove useful in certain applications for acceleration.

As a parameter for the strength of the laser, often the normalized laser vector potential

$$a_0 = \frac{eE_0}{m_e c \omega_0} \tag{2.12}$$

is used. This value can be interpreted in the way that an electric field of strength E_0 accelerates an electron to the energy $a_0 m_e c^2$ over the distance $\lambda_L/(2\pi)$. In other cases, one might be more interested in stating the peak intensity which is related to a_0 via

$$I_0 = 1.37 \cdot \aleph \cdot \left(\frac{a_0}{\lambda_L \, [\mu\mathrm{m}]} \right)^2 \times 10^{18} \, \mathrm{W\,cm^{-2}} \, . \tag{2.13}$$

Here, $\aleph$ denotes the polarization of the laser pulse ($\aleph = 1$ for linear, $\aleph = 2$ for circular polarization). From the parameters at hand, we may also calculate the power of the laser pulse or – taking into account its duration τ_0 – the energy. Depending on the intensity of the laser pulse, additional effects might need to be considered, e.g. radiation reaction [38] or the production of electron-positron pairs [39]; these will not be investigated in the following. Further, it should be noted that the theoretical description of laser pulses is highly idealized, i.e. pulses are generally not Gaussian. For example, in experiments a pre-pulse will be present which can be on the time scale of picoseconds and can affect the plasma dynamics significantly (cf. section 4.8).

2.2.1 Self-focusing

As described in the previous section, Gaussian beams are focused, i.e. their beam waist varies. This is important as this can influence the effectiveness of the different acceleration schemes: if the pulse energy is distributed over too wide of an area, no sufficient acceleration can occur. We do, however, work with laser pulses propagating through plasma, where an effect known as *self-focusing* can occur. In the presence of plasma, the wave

equation is changed to

$$\nabla^2\mathbf{E} - \frac{\eta^2}{c^2}\frac{\partial^2\mathbf{E}}{\partial t^2} = 0 \,, \tag{2.14}$$

where η is the refractive index [36]. Whether a wave can propagate through a plasma is effectively decided by the dispersion relation

$$\omega_0^2 = \omega_p^2 + c^2k^2 \,. \tag{2.15}$$

If $\omega_0 > \omega_p$, the wave number k is real and the electromagnetic wave can propagate through the plasma [40]. By contrast, for $\omega_0 < \omega_p$, the wave becomes evanescent as k is imaginary. For the case where $\omega_0 = \omega_p$ one introduces the *critical density*

$$n_{\mathrm{cr}} = \frac{\omega_0^2 m_e}{4\pi e^2} \,. \tag{2.16}$$

If the plasma density is small compared to n_{cr} we call the plasma *underdense*, otherwise it is called *overdense*. It has to be noted though, that due to the relativistic nature of the processes that we look at, plasmas can become *relativistically underdense* [41], which can drastically change the occurring processes compared to an opaque target.

From the dispersion relation we can also calculate the phase velocity v_{ph} and the group velocity v_{g} of the wave as

$$v_{\mathrm{ph}} = \frac{\omega_0}{k} = \sqrt{c^2 + \frac{\omega_p^2}{k^2}} \,, \qquad\qquad v_{\mathrm{g}} = \frac{\mathrm{d}\omega_0}{\mathrm{d}k} = \frac{c^2}{v_{\mathrm{ph}}} \,, \tag{2.17}$$

which we will need i.a. in our discussion of the positron acceleration scheme in section 4.6. Back to the refractive index, we can approximate

$$\eta \approx 1 - \frac{\omega_p^2}{2\omega_0^2}\frac{n(r)}{n_0\gamma_\perp} \,, \tag{2.18}$$

where $\gamma_\perp = \sqrt{1 + (a_0^2/2)}$ is the transverse relativistic factor. In the two cases that either intensity decreases or that density increases radially, the refractive index becomes higher on the central axis. This, in turn, forces the pulse energy to be focused towards the central axis, which is where the term "self-focusing" originates from. One can then consider the beam waist evolution in dependence of the laser power [42]. Doing so leads to the notion of the *critical power*

$$P_{\mathrm{cr}} = \frac{m_e c^5 \omega_0^2}{e^2\omega_p^2} \,, \tag{2.19}$$

which is often referenced by using the approximate equation $P_{\mathrm{cr}} \approx 17(\omega_0/\omega_p)^2\,\mathrm{GW}$ [43]. In the case where the laser power P matches the critical power P_{cr}, a balance between self-focusing and diffraction such that the laser pulse can be guided. Strongly surpassing the critical power can lead to the filamentation of the laser pulse [44] which can often be observed in simulations concerning the acceleration of ions.

While self-focusing is an effect generally beneficial for driving wakefields over longer distances, there are also effects detrimental to focusing in plasma. One of those is the ionization-induced defocusing [45, 46]. Since the field strength of the lasers that atoms are subjected to depend on their radial position with respect to the optical axis, ionization occurs more frequently at the laser center than elsewhere (for a Gaussian mode). This, in turn, leads to a radial density gradient, which affects the refractive index

$$\eta(r,t) = \sqrt{1 - \frac{n_e(r,t)}{n_{\mathrm{cr}}}}\ . \tag{2.20}$$

For the region of highest electron density, $\eta(r,t)$ becomes minimal, acting defocusing for the remaining parts of the pulse. If we want to see when this effect becomes important, we can follow the derivation presented by Gibbon [46]. It is known from e.g. Born and Wolf [47] that a light ray's trajectory $\mathbf{r}(t)$ is subject to the differential equation

$$\frac{\mathrm{d}}{\mathrm{d}s}\left(\eta(\mathbf{r})\frac{\mathrm{d}\mathbf{r}}{\mathrm{d}s}\right) = \nabla\eta(\mathbf{r})\ . \tag{2.21}$$

Here, $\mathrm{d}s$ is infinitesimal distance along the trajectory. Again, using the paraxial approximation and taking $\mathrm{d}s \approx \mathrm{d}z$ [48], we can rewrite the problem to

$$\frac{\mathrm{d}\mathbf{r}}{\mathrm{d}z} = \frac{\mathbf{k}_\perp}{k(z)}\ , \qquad \frac{\mathrm{d}\mathbf{k}_\perp}{\mathrm{d}z} = k_0\nabla_\perp\eta(r,z)\ , \tag{2.22}$$

where $k_0 = \omega_0/c$. We introduce the angle $\theta = k_\perp/k_\parallel$ and can Taylor expand $\eta(r)$ for underdense plasmas. Then we arrive at the equation

$$\frac{\mathrm{d}\theta}{\mathrm{d}z} \approx -\frac{1}{2}\frac{\partial}{\partial r}\left(\frac{n_e(r)}{n_{\mathrm{cr}}}\right)\ . \tag{2.23}$$

The total deflection of the beam scales like $\theta_I \propto \int n_e(0)/(n_{\mathrm{cr}}w_0)\ \mathrm{d}z$. Since a Gaussian beam focused in vacuum is also diffraction-limited [46, 49], we have a counteracting $\theta_D = w_0/z_R$. Finally, comparing the two parameters, Gibbon finds that for

$$\frac{n_e}{n_{\mathrm{cr}}} > \frac{\lambda_L}{\pi z_R} \tag{2.24}$$

ionization defocusing becomes important. This effect will be of particular interest in our discussion of the stability of a positron acceleration scheme in section 4.6.

2.2.2 Ponderomotive force

One last important ingredient for laser-driven wakefield acceleration is the ponderomotive force which is responsible for expelling the electrons in transverse direction, leaving behind the cavity. Kruer derives the ponderomotive force in the non-relativistic limit $a_0 < 1$ the following way [50]: he assumes that the laser field has the form $\mathbf{E}(\mathbf{r}, t) = \mathbf{E}(\mathbf{r}) \sin(\omega t)$, where $\omega \geqslant \omega_p$. Further, the plasma is initially at rest ($\mathbf{u} = 0$) and no magnetic field is present ($\mathbf{B} = 0$). The force equation then is

$$\frac{\partial \mathbf{u}}{\partial t} + \mathbf{u} \cdot \nabla \mathbf{u} = -\frac{e}{m} \mathbf{E}(\mathbf{r}) \sin(\omega t) \ . \tag{2.25}$$

In the lowest order in $|\mathbf{E}|$, we have $\mathbf{u} = \tilde{\mathbf{u}}$ with

$$\frac{\partial \tilde{\mathbf{u}}}{\partial t} = -\frac{e}{m} \mathbf{E}(\mathbf{r}) \sin(\omega t) \ . \tag{2.26}$$

Integrating with respect to t and averaging the force equation over rapid oscillations yields

$$m \frac{\partial \langle \mathbf{u} \rangle_t}{\partial t} = -e \langle \mathbf{E} \rangle_t - m \langle \tilde{\mathbf{u}} \cdot \nabla \tilde{\mathbf{u}} \rangle_t \ . \tag{2.27}$$

Using the expression for $\tilde{\mathbf{u}}$ and the product rule of differentiation, Kruer then rearranges the equation to

$$m \frac{\partial \langle \mathbf{u} \rangle_t}{\partial t} = -e \langle \mathbf{E} \rangle_t - \frac{1}{4} \frac{e^2}{mc^2} \nabla \mathbf{E}^2(\mathbf{r}) \ , \tag{2.28}$$

where the ponderomotive force corresponds to the term

$$\mathbf{F}_p = -\frac{1}{4} \frac{e^2}{mc^2} \nabla \mathbf{E}^2(\mathbf{r}) \ . \tag{2.29}$$

A full derivation of the relativistic ponderomotive force can be found in the work by Quesnel and Mora [51]. There, the final form of the ponderomotive force is

$$\mathbf{F}_p = -m_e c^2 \nabla \bar{\gamma} \ , \tag{2.30}$$

with $\bar{\gamma}$ being the averaged Lorentz factor of the electron.

2.3 Plasma waves

Now we can look at the interaction of a laser pulse with a plasma. This interaction will lead to the excitation of a plasma wave. Depending on the strength of the laser, i.e. how large the normalized laser vector potential a_0 is, we can differentiate various regimes of wave excitation. As mentioned later, other laser parameters like pulse duration and focal spot size also determine the regime of plasma wave.

We start by looking at the linear regime, where $a_0 \ll 1$. Here we can make use of the cold fluid equations. For simplicity it is assumed that the plasma is initially uniform [11]. If the electrostatic wakefield ψ introduces a density perturbation $\delta n = n - n_0$, we can write

$$\left(\frac{\partial^2}{\partial t^2} + \omega_p^2\right)\frac{\delta n}{n_0} = c^2\nabla^2\frac{a^2}{2} , \qquad \left(\frac{\partial^2}{\partial t^2} + \omega_p^2\right)\psi = \omega_p^2\frac{a^2}{2} . \tag{2.31}$$

The solution for the density perturbation is of the form

$$\frac{\delta n}{n_0} = \frac{c^2}{\omega_p}\int_0^t \mathrm{d}t' \ \sin[\omega_p(t-t')]\nabla^2\frac{a^2(\mathbf{r},t')}{2} \tag{2.32}$$

and for the electric field one finds

$$\frac{\mathbf{E}}{E_0} = -c\int_0^t \mathrm{d}t' \ \sin[\omega_p(t-t')]\nabla\frac{a^2(\mathbf{r},t')}{2} . \tag{2.33}$$

These plasma waves have a frequency of ω_p and are of sinusoidal shape. The parameter $E_0 = m_e c\omega_p/e$ is the cold, non-relativistic wave breaking field. The solutions are valid if $|\mathbf{E}| \ll E_0$; otherwise wave breaking needs to be considered.

Now, considering that $|\mathbf{E}|$ may exceed E_0, we reach the non-linear regime ($a_0 > 1$). This is accompanied by a steepening of the wave to a sawtooth-like profile as well as an increase in wavelength. For a peak electric field $E_{\max}$ of the plasma wave, it is

$$\lambda_{\mathrm{nonlinear}} = \frac{2\lambda_p}{\pi}\frac{E_{\max}}{E_0} , \tag{2.34}$$

where λ_p is the plasma wavelength [42]. In the case of the linear regime the wavelength would simply correspond to λ_p. Due to the increase in wavelength, the density perturbations become more spiked. Once they become singular, the point of wave breaking is reached. The relativistic wave breaking field in 1D scales as

$$E_{\mathrm{WB}} = \sqrt{2}(\gamma_{\mathrm{ph}} - 1)^{1/2}E_0 , \tag{2.35}$$

where γ_{ph} is the Lorentz factor for the wave moving with phase velocity v_{ph} [42]. The

plasma waves or rather their electric fields are then capable of trapping particles as we will further describe over the next sections.

2.4 Wakefield acceleration

As seen in the previous section, plasma waves can be excited by laser pulses. The induced wakefields can trap electrons and accelerate them to high energies. Depending on the parameter range, more or less desirable features for high-quality electron beams are obtained. As we are going to discuss over the next few sections, there are several types of wakefield accelerators that can utilize different effects for injection and trapping of electrons into the wake.

2.4.1 Laser-driven wakefield acceleration

The method of using laser-plasma induced wakefields for particle acceleration was first introduced by Tajima and Dawson in 1979 [7]. It is aptly called *laser-driven plasma wakefield acceleration* or abbreviated to LWFA. For LWFA, a high-intensity ($\geqslant 10^{17}$ W/cm^2), short ($\leqslant 1$ ps) laser pulse penetrates a plasma target and induces a plasma wave. As described before, the ponderomotive force of the laser pulse pushes electrons in the transverse direction while the ions exert a restoring force. Plasma electrons can then be trapped in the structure and experience accelerating fields (more on that in section 2.4.3). The accelerated electrons are usually called "witness beam".
Different regimes of LWFA can be differentiated mainly by the normalized laser vector potential a_0. Of particular interest is the so-called *bubble regime*, where $a_0 > 4$, $w_0 > 2\lambda_L$ and the pulse fits perfectly into the first half of the plasma period [12, 14]. The "bubble" (i.e. the cavity) is nearly spherical and exhibits uniform accelerating fields. Further, the energy spectrum of the electrons in the witness beam is quasi-monoenergetic [13].
Particle acceleration via LWFA has, of course, also its limits. One important example of a process limiting the acceleration is *dephasing*. Since the plasma wave evolves with the laser's group velocity, the accelerated electrons will experience different parts of the accelerating field [40]. After some time, they will have reached a decelerating region of the field. The acceleration distance, after which this occurs has been calculated in several models for different dimensionality [52]. In 3D, the dephasing length is

$$L_d = \frac{4}{3}\frac{\omega_0^2}{\omega_p^2}\frac{\sqrt{a_0}}{k_p} \,. \tag{2.36}$$

Another limiting factor relevant to LWFA is that of *pump depletion*. When traversing the plasma, the laser pulse continuously loses energy to the plasma. After propagating the

pump depletion length, it cannot sustain a wakefield any longer. Again, considering the three-dimensional, non-linear case [40], the pump depletion length scales like

$$L_{\mathrm{pd}} = \frac{\omega_0^2}{\omega_p^2} c\tau_0 \ . \tag{2.37}$$

Beyond choosing the laser and plasma parameters in an optimal fashion for long acceleration distances, there is on-going research on how to e.g. overcome the dephasing limit by modulating the plasma density profile [53].

2.4.2 Particle beam-driven plasma wakefield acceleration

Besides LWFA, there is also the option to perform wakefield acceleration with a particle-beam driver instead of a laser pulse. This mechanism is called *particle-beam driven plasma wakefield acceleration* or PWFA for short. Here, the Coulomb force of the particle driver (e.g. consisting of electrons, or protons in the case of AWAKE [54]) takes over the role of the ponderomotive force in LWFA. The electric field of a relativistic particle beam is almost completely transverse: The electric field of a single electron in its rest frame is $E \propto r^{-2}$, i.e. radially symmetric. Now, performing a Lorentz transform to the laboratory frame yields $E_\perp = \gamma E_\parallel$, meaning that for $\gamma \to \infty$ we have a mostly transverse electric field [55].

The particle driver needs to be of high enough density to induce the corresponding plasma wave. The created structure looks similiar to LWFA, but is not completely the same due to the differences of the driver [56].

Similar to the case of laser-driven plasma waves, we can differentiate between a linear and a non-linear regime also for PWFA. The electric field created by a particle beam of density n_b can be calculated via Poisson's equation $\nabla \cdot \mathbf{E} = -4\pi e n_b$ [42]. We assume that the driving beam is relativistic ($v \approx c$) and has a radius r_b that is large compared to the plasma wavelength, i.e. $r_b k_p \gg 1$. Then, the amplitude of the wakefield is approximately $E_{\max}/E_0 = n_b/n_0$. A solution for the transverse wake structure has been obtained for various beam profiles [10]. Again, with the associated wakefield, electrons can be injected and accelerated. The particles' energy gain is, however, limited i.a. by the *transformer ratio* [42]. This is the ratio between the energy gained from the wakefield and the energy that the driver originally has, i.e. $R_t = \Delta\gamma/\gamma_b$. Similar to the laser pulse, the driving electron beam will be depleted of all its energy after having traversed some characteristic distance. This depletion length can be optimized, e.g. by tailoring the driver's axial profile [42, 57].

The transformer ratio as well as the maximum field strength of the wake can also be increased by going to the non-linear regime of PWFA, where $n_b \approx n_0$. If $r_b k_p < 1$ and

$n_b > 1$, the wakefield is mainly described by non-linear transverse plasma motion. Since close to all of the plasma electrons are expelled from the region of the driver, this regime is also called the "blowout" regime [15], although in some literature the terms "blowout" and "bubble" are used interchangeably.

PWFA has the advantage that some of the limiting factors of LWFA are not applicable since the driver consists of massive particles instead of a laser pulse. There are, however, other effects detrimental to it. One example would be the hosing instability [58]. During propagation through the plasma, the electrons in the driving beam can start to oscillate in a collective manner. This behaviour can induce an oscillation of the associated electromagnetic fields and thus reduce witness beam quality. In the worst case it can even lead to the loss of witness beam electrons. Active research to mitigate such instabilities is also being conducted [59, 60].

2.4.3 Particle trapping

Essential for the acceleration of electrons in wakefields is that they get trapped, i.e. they are at some point injected into the cavity and do not leave it afterwards. This could be seen from phase space plots, where trapped electrons should move on closed orbits, while untrapped electrons do not [11].

The simplest mechanism for electron trapping is the so-called *self-injection*. For this it is required that the electron has sufficient initial velocity; otherwise it slips backward in the plasma wave. For example, a simple condition for trapping was derived by Kostyukov *et al.* in [61] based on a phenomenological bubble model. Mathematically, they start by considering the Hamiltonian

$$\mathcal{H} = c\sqrt{m_e^2c^2 + (\mathbf{P} + e\mathbf{A}/c)^2 + m_e c^2 a^2} + e\phi \,, \tag{2.38}$$

where $\mathbf{P}$ is the electron's canonical momentum and $\mathbf{A}$ is the vector potential. In order for the particle to be trapped, there must be a point on its trajectory where the longitudinal velocity component becomes zero (i.e. the particle does not fall further back in the wave but gets accelerated to the front instead). Further calculation then yields that the bubble can trap electrons initially at rest if the bubble radius R is larger than the bubble's Lorentz factor γ_0. Depending on the models used, slightly or more significantly [62] deviating trapping conditions are obtained.

Besides self-injection, there are several other mechanisms that can be employed. Usually, those methods are designed to either trap more electrons than in self-injection or increase the quality of the witness beam. For example, density-down ramps can be utilized to change the velocity of the plasma wave which leads to a change in trapping condition

[19]. Ionization injection is another method for improved trapping: there, the presence of an additional, heavier element is used to induce localized potential changes [63]. These can change the momenta of the electrons such that they can be trapped more easily. Lastly, a scheme for high quality electron beams is the Trojan Horse Acceleration [20] that we already have mentioned in the introduction: a wakefield is driven by an electron beam and an additional weak laser beam ionizes atoms in the cavity. The electrons from ionization then are trapped in the blowout. Since they do not have a large transverse momentum, the emittance of the witness beam is much lower than usual.
We further investigate the concept of wakefield acceleration in chapter 4, where we also present further theory for a description of the blowout shape in the non-linear regime. Something we have omitted here, but will discuss in that chapter as well, is the acceleration of positrons: since positrons have opposite charge to electrons we cannot simply accelerate positrons with the same field regions of the wake. For now, we will go over to a basic introduction about ion acceleration.

2.5 Ion acceleration

The acceleration of ions via laser-matter interaction poses a different set of problems: ions are significantly heavier than electrons (ca. 1836× already in the case of the lightest ion, H^+). Already for other, heavier leptons like the muon, wakefield acceleration becomes more complicated as the plasma wave velocity should be matched for high-quality acceleration. Thus, while proton wakefield acceleration [64] might be theoretically feasible, it requires much higher laser intensities than the LWFA of electrons and needs further optimization.
There are, however, also several other schemes of ion acceleration. One prominent example is Target Normal Sheath Acceleration (TNSA), where a laser pulse irradiates a thin solid foil (for example made of Carbon). The laser field will push the electrons in the foil, creating an electric sheath field due to the shift between electrons and protons [30]. This field then leads to the acceleration of ions in a directed motion out of the target. Besides TNSA, there are many other schemes [21, 22, 65, 66] which further aim to improve upon beam collimation, energy spread, etc. and utilize different target setups. Depending on the use case, however, not all of these schemes are equally applicable: since we will solely investigate the acceleration of spin-polarized particles like H^+ and ^3He in the scope of ion acceleration in this thesis, solid-state targets are not an option [67]. As discussed later on, the target already needs to be pre-polarized in order to get a spin-polarized particle beam. With current methods it cannot be easily done for solid targets, but instead for gaseous targets.

Thus, we will investigate the use of Magnetic Vortex Acceleration (MVA) for this project [32, 33]. As for many of the ion acceleration schemes, there is no full analytical theory for its description due to the multitude of relevant effects and disparate time scales. The process of MVA has phenomenologically explained by Park *et al.* as follows [68]:
The laser pulse propagates through the near-critical density (NCD) target and pushes the electrons radially outwards. This creates a channel of low electron density with a radius of

$$R_{\mathrm{ch}} = \frac{\lambda_L}{\pi}\left(\frac{n_{\mathrm{cr}}}{n_e}\right)^{1/3}\left(\frac{2}{K}\frac{P}{P_{\mathrm{cr}}}\right)^{1/6} . \tag{2.39}$$

The parameter $K = 1/13.5$ is of geometrical nature [69]. In the wakefield of the laser pulse some electrons are accelerated, thereby inducing a strong current. A corresponding return current is formed in the wall of the channel. Together they give rise to a strong azimuthal magnetic field of strength $B_{\mathrm{ch}} \approx 2\pi e n_e R_{\mathrm{ch}} \gamma_e^2$, where γ_e is the bulk Lorentz factor of the accelerated electrons [70]. Once the end of the NCD target is reached, the magnetic field expands transversely. In turn, it displaces the electrons with respect to the ions inducing longitudinal and transverse electric fields. These fields are then able to collimate and accelerate ion beams.
The optimal ion energy is reached when the laser energy inside the channel is equal to the total electron energy after interaction with the laser [71]. The corresponding condition reads

$$\frac{n_e}{n_{\mathrm{cr}}} = \sqrt{2}K\left(\frac{P}{P_{\mathrm{cr}}}\right)^{1/2}\left(\frac{c\tau_0}{L_{\mathrm{ch}}}\right)^{3/2} , \tag{2.40}$$

where L_{ch} is the channel length. What was neglected here is whether the NCD target has a density-down ramp. It has been investigated by Nakamura *et al.* in [72], how the presence of such a ramp influences the transverse expansion of the magnetic field and accordingly the attainable ion energy. In section 5.3.1, we study the effects of down-ramps onto the spin polarization of proton beams.

With this, we have a basic understanding of electron and ion acceleration mechanisms. As we have especially noted in the section regarding ion acceleration, working with analytical theories for the regimes at hand is often not possible. We can "circumvent" this problem by employing numerical simulations. Thus, we introduce the concept of particle-in-cell simulations in the next chapter.

Chapter 3

The particle-in-cell method

In order to describe laser-matter interaction, often times analytic calculation does not suffice due to the complexity of the problem at hand. Therefore, numerical methods are needed to describe the abundance of – often relativistic – particles. One of the available options are particle-in-cell (PIC) simulations. Throughout most of the work performed in the scope of this thesis, PIC simulations have been employed in form of the codes VLPL and QV3D, both of which have been developed by A. Pukhov [73, 74]. The differences between the codes VLPL and the quasi-static QV3D will be explained later on. A more extensive introduction to PIC codes is given in [74], on which this chapter is based.

3.1 From the Vlasov equation to PIC

In order to perform simulations for laser-plasma based setups we i.a. need to solve Maxwell's equations

$$\frac{\partial \mathbf{E}}{\partial t} = c\nabla \times \mathbf{B} - 4\pi \mathbf{j} \,, \tag{3.1}$$

$$\frac{\partial \mathbf{B}}{\partial t} = -c\nabla \times \mathbf{E} \,, \tag{3.2}$$

$$\nabla \cdot \mathbf{E} = 4\pi\rho \,, \tag{3.3}$$

$$\nabla \cdot \mathbf{B} = 0 \,. \tag{3.4}$$

One can show that we may reduce the set of equations we need to solve to (3.1) and (3.2), and use (3.3), (3.4) as initial conditions only [74].

The current density $\mathbf{j}$, which acts as a source term for the electromagnetic fields, could be described by a single-particle distribution function $f(\mathbf{x}, \mathbf{p})$ for each species of particle.

The evolution of this function is given by the Boltzmann-Vlasov equation

$$\frac{\partial f}{\partial t} + \frac{\mathbf{p}}{\gamma m}\nabla f + \frac{\mathbf{F}}{m}\nabla_p f = \mathrm{St} \ , \tag{3.5}$$

where St incorporates particle collisions [34]. Solving this equation poses a great computational challenge as it is six-dimensional. We can, however, use the so-called *finite element method*. The distribution function can be sampled by a set of finite phase-fluid elements

$$f(\mathbf{x}, \mathbf{p}) \approx \sum_n w_n S(\mathbf{x} - \mathbf{x}_n, \mathbf{p} - \mathbf{p}_n) \ . \tag{3.6}$$

The term $S(\mathbf{x}, \mathbf{p})$ is the support function for the n-th element in the phase space (e.g. a 6D hypercube) and w_n is the corresponding weight. With this approximation we can describe the transport of the phase fluid along the Boltzmann-Vlasov characteristics by integrating for the centers of the fluid elements, i.e.

$$\frac{\mathrm{d}\mathbf{x}_n}{\mathrm{d}t} = \frac{\mathbf{p}_n}{\gamma m} \ , \qquad \frac{\mathrm{d}\mathbf{p}_n}{\mathrm{d}t} = q\left(\mathbf{E} + \frac{\mathbf{p}_n}{\gamma m c} \times \mathbf{B}\right) + \mathbf{F}_{\mathrm{St}} \ . \tag{3.7}$$

In the latter equation, $\mathbf{F}_{\mathrm{St}}$ corresponds to the collisional term of the Boltzmann-Vlasov equation. Therefore, we do not need a grid in the full phase space, but do utilize a grid in configuration space to solve Maxwell's equations.

3.2 Maxwell solver

In order to solve Maxwell's equations there are several numerical schemes. The most commonly used one is the Yee solver [75]. Depending on the solver different criteria must be fulfilled in order to ensure numerical stability. The criteria are related to the spatial grid size and the time step. The choice of these is also important for preventing unphysical simulations results from occuring. The Courant-Friedrichs-Lewy condition [76] states that

$$c\Delta t < \left(\frac{1}{h_x^2} + \frac{1}{h_y^2} + \frac{1}{h_z^2}\right)^{-1/2} \ . \tag{3.8}$$

Here, h_x, h_y, h_z denote the grid size in the respective dimensions and Δt is the time step. The condition ensures that information may only propagate at the speed of light but not faster.

For most of our simulations presented in the later chapters, we will use an alternative Maxwell solver: the RIP solver. The short-hand stands for "rhombi-in-plane"; the meaning

behind this is visible in its full description in [77]. RIP is a z-dispersionless Maxwell solver which means that several effects linked to numerical dispersion are suppressed by it. Hereinafter, we refer to it as z-dispersionless, as for most of our simulations z is the direction of propagation. It was compared by Filipovic *et al.* to the Yee solver for the case of relativistic electron bunches in the regime of quantum electrodynamics [78]. There, RIP was shown to suppress the numerical Cherenkov instability and did not exhibit any unphysical fields whereas the Yee solver did. Due to the different scheme used, the RIP solver links the grid size in z-direction to the time step via the condition $h_z = c\Delta t$. The stability condition for the RIP solver in vacuum reads

$$h_z^2 \left(\frac{1}{h_x^2} + \frac{1}{h_y^2} \right) < 1 \, . \tag{3.9}$$

In the presence of plasma it is modified to

$$\frac{1}{h_z^2} > \frac{1}{h_x^2} + \frac{1}{h_y^2} + \frac{\omega_p^2}{4c^2} \, . \tag{3.10}$$

The linkage of z- and time step means that the numerical simulation can only be set up in certain ways, as the time step needs to resolve the fastest oscillations for proper results.

3.3 Boris pusher

For advancing the particles often times the Boris (or "implicit midpoint") pusher [79] is used, although there are other available that have their own advantages and disadvantages [80, 81]. The Boris pusher uses the interpolated electric and magnetic field $\mathbf{E}, \mathbf{B}$ and calculates the momentum for the new time step $\mathbf{p}_1$ from the old $\mathbf{p}_0$ according to the equation

$$\frac{\mathbf{p}_1 - \mathbf{p}_0}{\tau} = e \left(\mathbf{E} + \frac{1}{c} \frac{\mathbf{p}_1 + \mathbf{p}_0}{2\gamma_{1/2} m} \times \mathbf{B} \right) \, . \tag{3.11}$$

Here $\gamma_{1/2}$ is the Lorentz factor taken at half the time step. The scheme is semi-implicit and can be solved for the final momentum; see e.g. [74] for this. Its main advantage to simpler particle pushers is that, due to the separated rotation step and $\mathbf{B}$ and the advance in $\mathbf{E}$, it describes relativistic particle motion more correctly.

To summarize the previous section that dealt with certain aspects of the simulation we will now list the steps performed within a time step of PIC simulations in order (cf. also Fig. 3.1): The electromagnetic fields are first interpolated from the grid-based values to the particle positions. The particles are then pushed using the calculated forces. As

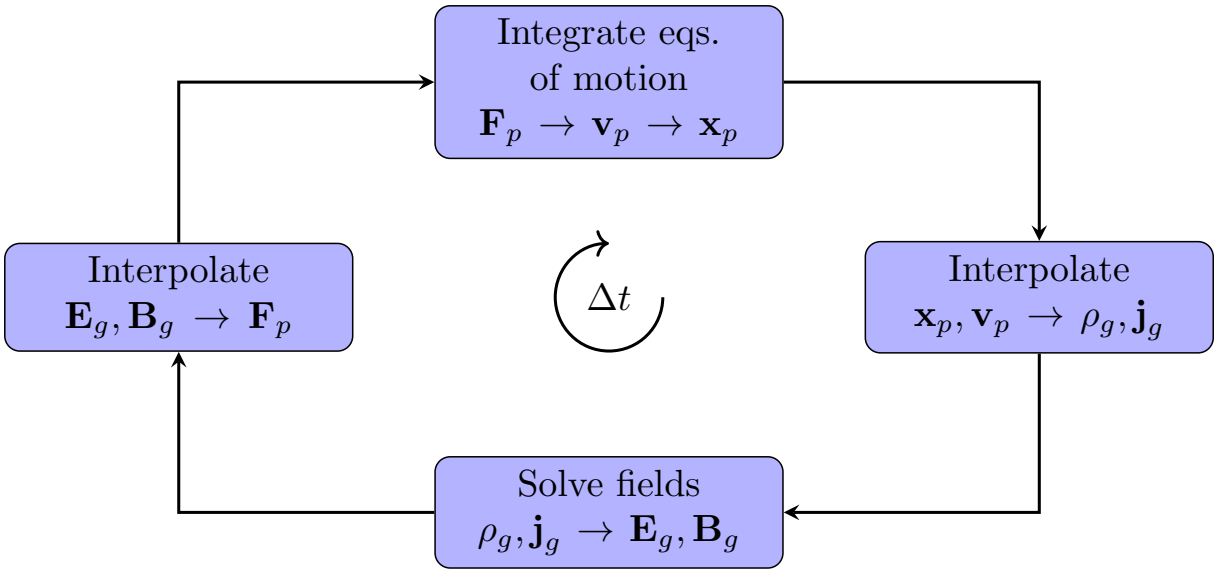

Figure 3.1: Schematic of the particle-in-cell cycle. The index "p" corresponds to variables given at the macro-particle position, while the index "g" denotes variables at the grid position.

the particle movement induces currents, these currents are interpolated to the grid, after which the fields can be advanced using the Maxwell solver. This process is then repeated for as many time steps as desired. Depending on the effects to be incorporated into the simulations, this cycle might be supplemented by other effects like Monte Carlo routines for effects of quantum electrodynamics or, as in the case of our considerations in chapter 5, a routine for the precession of particle spin.

3.4 Quasi-static codes

While it is only used for one of the publications in the following chapters [82], we should briefly introduce the concept of *quasi-static* PIC codes. Due to the very disparate scales in PIC simulations, numerical heating can become a problem which corresponds to diffusion in the phase space. A consequence of the heating is that energy is no longer conserved and unphysical simulation results may arise. This generally limits the time interval that can be simulated correctly with PIC codes. One possible way to improve upon this is the so-called *quasi-static approximation* [83]. There is a plethora of different PIC codes that utilize this approximation and have different dimensionality or coordinate systems. For our group, the quasi-static code based on VLPL is called QV3D. It is a 3D code using cartesian coordinates. In setups like wakefield acceleration, we have two evolution time scales: the faster scale of the driver, and the slower scale of acceleration. These time scales will be separated in the quasi-static approximation.

In his explanation of his code [74], Pukhov first introduces the new coordinates

$$\tau = t \,, \qquad\qquad \xi = z - ct \,. \tag{3.12}$$

Here, it should be noted for clarity, that different literature introduces the new spatial coordinate sometimes in different ways: other references might call this variable ζ, or they might use a different sign convention. Our assumption is that, while propagating a distance of approximately its own length, the driver changes slowly. Thus, for the plasma response to the driver, all derivatives with respect to the slow time τ will be neglected. Advancing from the head to tail of the driver, we can calculate the wakefield at time τ. With the calculated fields and particle distribution of the surrounding plasma, we can advance the driver with a large time step. While the quasi-static method allows for higher performance, it also gives some restrictions, as it cannot describe radiation and particle trapping.
Writing Maxwell's equations with respect to the new variable ξ and neglecting slow changes, we can find the quasi-static equations for the electric and magnetic field (again, see [74] for an extensive derivation of the equations). A layer of macro-particles is seeded at the front boundary of the simulation domain after gathering charge density and currents of the driving beam. The particles move in negative ξ-direction in accordance with the quasi-static equations of motion. The driver can be advanced in time using the fields induced by particles traversing the simulation box. Depending on the type of driver, this evolution needs to be considered differently: for particle beams, the equation of motion of the particles can be calculated. For a laser pulse, we instead need to solve an envelope model as the quasi-static code does not incorporate radiation.

With the analytical and numerical foundation for this thesis laid out, we can go over to the study of wakefields and Magnetic Vortex Acceleration. In the next chapter, we will first introduce an extensive analytical framework for the description of non-linear blowouts which will be compared to results from PIC simulations.

Chapter 4

Wakefield acceleration

With our knowledge from the previous chapter we can look into the first more involved setups. In the context of wakefield acceleration, it is of interest to describe the shape of the bubble/blowout and its fields rather well. While there have been simple, phenomenological models introduced in the past [61, 84], their applicability is quite limited. More recently, models i.a. by Lu *et al.* [85] and Golovanov and Thomas [86–88] have been proven to work for more general plasma profiles with a radial dependence.

In this chapter, we further improve upon the description of blowouts based on these models. One particular aspect lacking in current models is the description of the longitudinal electric field: while PIC simulations clearly show a divergence towards the end of the blowout, analytical models do not incorporate this feature very well. Thus, we start by "fixing" this divergence as we have presented in our publication [89]. For this, we introduce the general equations and notation used also in the subsequent section concerning further modeling of PWFAs.

Throughout this chapter we normalize time to the inverse plasma frequency ω_p^{-1}, lengths to $k_p^{-1} = c/\omega_p$, kinetic momenta to $m_e c$, energies to $m_e c^2$, fields to $m_e c\omega_p/e$, charges to the elementary charge e, masses to the electron rest mass m_e and potentials to $m_e c^2/e$.

The quasi-static wakefield potential is generally given as

$$\psi = A_z - \varphi \,, \tag{4.1}$$

where $\mathbf{A}$ and φ are the vector and scalar potential, respectively. The bubble is moving in z-direction with a velocity $V_0 \approx c$. Therefore, it makes sense to introduce a co-moving coordinate system with $\xi = z - t$. The problem exhibits cylindrical symmetry, thus

$$\mathbf{B} = \nabla \times \mathbf{A} = \left(\frac{\partial A_r}{\partial \xi} - \frac{\partial A_z}{\partial r} \right) \mathbf{e}_\varphi \,, \qquad \mathbf{E} = \nabla\psi - \mathbf{e}_z \times \mathbf{B} \,. \tag{4.2}$$

Specifically, the longitudinal and radial electric fields are of the form

$$E_z = \frac{\partial \psi}{\partial \xi} \,, \qquad\qquad E_r = \frac{\partial \psi}{\partial r} + B_\varphi \,. \tag{4.3}$$

The force components then become

$$F_z = -E_z - \frac{p_r}{\gamma} B_\varphi \,, \qquad\qquad F_r = -\frac{\partial \psi}{\partial r} - \left(1 - \frac{p_z}{\gamma}\right) B_\varphi \,. \tag{4.4}$$

The plasma profile $\rho(r)$ is assumed to have only radial dependence in the following. The wakefield potential can then be described as a function of ξ and r,

$$\psi(\xi, r) = \int_0^r \frac{S_I(r')}{r'} \, \mathrm{d}r' + \psi_0(\xi) \,. \tag{4.5}$$

The integral source

$$S_I(x) = \int_0^x \rho(r) r \, \mathrm{d}r > 0 \tag{4.6}$$

only depends on the radial coordinate. The term ψ_0 in the wakefield potential often is assumed to vanish in theory and depends on the bubble radius $r_b(\xi)$. The argument of the bubble radius will be left out for a shorter notation in the following. We find that

$$\psi_0(\xi) = -\int_0^{r_b} \frac{S_I(r_b)}{r} \, \mathrm{d}r - \frac{S_{I,b}\beta(r_b)}{2} \,. \tag{4.7}$$

Further, the parameter β is

$$\beta(r_b) = 2 \int_0^\infty \frac{\epsilon \, \mathrm{d}x}{1 + \epsilon x} \frac{F_0(x) + \epsilon F_1(x)}{1 + \epsilon F_1(0)} \tag{4.8}$$

with bubble radius $r_b(\xi)$, relative sheath width $\epsilon = \Delta / r_b$. Here, Δ is the thickness of the electron sheath. We use a function $g(y)$ to describe the shape of the electron sheath at the bubble boundary. The generalized momenta are

$$F_n(x) = \int_x^\infty y^n g(y) \, \mathrm{d}y \,. \tag{4.9}$$

We further assume that $F_0(0) = 1$. The field components can then be calculated as

$$E_z(\xi, r) = -\left(\frac{S_{I,b}}{r_b} + \frac{S_{I,b}\beta'(r_b)}{2} + \frac{\rho(r_b)\beta(r_b)r_b}{2}\right) r_b' \,, \tag{4.10}$$

$$B_\varphi(\xi, r) = -\frac{r}{2}\frac{\partial E_z}{\partial \xi} - \Lambda(r, \xi) \,, \tag{4.11}$$

$$E_r(\xi, r) = \frac{\partial \psi}{\partial r} + B_\varphi = \frac{S_I(r)}{r} + B_\varphi \,. \tag{4.12}$$

Here,

$$\Lambda(r, \xi) = -\frac{1}{r}\int_0^r j_z(\xi, r')r' \, \mathrm{d}r' \tag{4.13}$$

is the integral current density. In total, this gives the following force components:

$$F_z = -E_z - \frac{p_r}{\gamma}B_\varphi \,, \tag{4.14}$$

$$F_r = -\frac{S_I(r)}{r} - \left(1 - \frac{p_z}{r}\right) B_\varphi \,. \tag{4.15}$$

4.1 Homogeneous plasma

In the special case of a homogeneous plasma with $\rho(r) = 1$ and $S_I(r) = r^2/2$, the electric field components are

$$E_r = \frac{r}{2} + B_\varphi \,, \tag{4.16}$$

$$E_z = -\frac{r_b r_b'}{2}\left(1 + \beta(r_b) + \frac{r_b\beta'(r_b)}{2}\right) \,. \tag{4.17}$$

Accordingly, the force components become

$$F_z = \frac{r_b r_b'}{2}\left(1 + \beta(r_b) + \frac{r_b\beta'(r_b)}{2}\right) - \frac{p_r}{\gamma}B_\varphi \,, \tag{4.18}$$

$$F_r = -\frac{r}{2} - \left(1 - \frac{p_z}{\gamma}\right) B_\varphi \,. \tag{4.19}$$

If we assume the bubble to be spherically shaped, then we can set $r_b = \sqrt{R^2 - \xi^2}$ with $r_b' = -\xi/r_b$. Moreover, we assume that the bubble sheath is thin, thus $\beta = \beta' = 0$. With this the electromagnetic fields can be simplified to

$$E_z = \frac{\xi}{2} \,, \qquad B_\varphi = -\frac{r}{4} - \Lambda(r, \xi) \,, \qquad E_r = \frac{r}{4} - \Lambda(r, \xi) \,. \tag{4.20}$$

This form is well known from other simplified bubble models. The accelerating and focusing force components then are

$$F_z = -\frac{\xi}{2} + \frac{r p_r}{4\gamma} + \frac{p_r}{\gamma}\Lambda(r,\xi) \,, \tag{4.21}$$

$$F_r = -\frac{r}{4}\left(1 + \frac{p_z}{\varphi}\right) - \frac{1}{2\gamma^2}\Lambda(r,\xi) \,. \tag{4.22}$$

The particles undergo fast betatron oscillations. Therefore we can assume that $\langle r p_r \rangle \approx 0$. After sufficient acceleration, we further have $p_z \approx \gamma$, giving us the simplified force terms

$$F_z \approx -\frac{\xi}{2} \,, \qquad F_r \approx -\frac{r}{2} \,, \tag{4.23}$$

which are – again – well known from simplified bubble models like [61].

4.2 Stretched bubble

A slightly more complicated form of the bubble would be to assume that it is not spherical, but stretched. We further assume that this bubble has a small amplitude, $R \ll \lambda_p$, similar to [90]. To describe a stretched bubble, we set

$$r_b = \sqrt{1 - \left(\frac{\xi}{b}\right)^2} \,, \tag{4.24}$$

where $b > R$. In turn, the longitudinal electric field becomes $E_z = a\xi$ with $a \in (0, 1/2)$. In the thin-sheath approximation $\beta = \beta' = 0$, we further obtain

$$B_\varphi = -\frac{r}{2}a - \Lambda(r,\xi) \,, \qquad E_r = \frac{r}{2}(1-a) - \Lambda(r,\xi) \,. \tag{4.25}$$

From this we can again calculate the force to be

$$F_z = -a\xi + \frac{r p_r}{2\gamma}a + \frac{p_r}{\gamma}\Lambda(r,\xi) \,, \tag{4.26}$$

$$F_r = -\frac{r}{2}\left(1 - a + a\frac{p_z}{\gamma}\right) - \frac{1}{2\gamma^2}\Lambda(r,\xi) \,. \tag{4.27}$$

As in the case considered before, we are able to assume $\langle r p_r \rangle$ as well as $p_z \approx \gamma$. Therefore, the force components approximately correspond to

$$F_z \approx -a\xi \,, \qquad F_r \approx -\frac{r}{2} \,. \tag{4.28}$$

From the equations (4.28) it becomes clear that the bubble's elongation leaves the focusing force unchanged. This holds as long as the electrons are already trapped, perform betatron oscillations and have high energy. The accelerating force F_z, by contrast, is dependent on the factor a.

4.3 Bubble ODE

In general, the ordinary differential equation

$$A(r_b)r_b'' + B(r_b)(r_b')^2 + C(r_b) = \frac{\Lambda(r_b(\xi),\xi)}{r_b} \tag{4.29}$$

is solved to obtain an approximation of the electron sheath with radius $r_b(\xi)$ surrounding the bubble. The coefficient functions are

$$A(r_b) = 1 + \frac{S_{I,b}}{2} + \left(\frac{\rho(r_b)r_b^2}{4} + \frac{S_{I,b}}{2}\right)\beta + \frac{S_{I,b}r_b}{4}\beta' \,, \tag{4.30}$$

$$B(r_b) = \frac{\rho(r_b)r_b}{2} + \left[3\rho(r_b)r_b + \rho'(r_b)r_b^2\right]\frac{\beta}{4} + \left[S_{I,b} + \rho(r_b)r_b^2\right]\frac{\beta'}{2} + S_{I,b}r_b\frac{\beta''}{4} \,, \tag{4.31}$$

$$C(r_b) = \frac{S_{I,b}}{2r_b}\left[1 + \left(1 + \frac{S_{I,b}\beta}{2}\right)^{-2}\right] \,. \tag{4.32}$$

An extensive derivation is given by Thomas *et al.* in [91]. If the sheath thickness Δ fulfills $\Delta \ll r_b$ and $\Delta \gg 2r_b/S_{I,b}$, we can simplify the coefficient functions to a great extent, namely

$$A(r_b) \approx \frac{S_{I,b}}{2} \,, \qquad B(r_b) \approx \frac{\rho r_b}{2} \,, \tag{4.33}$$

$$C(r_b) \approx \frac{S_{I,b}}{2r_b} \,, \qquad \Lambda(\xi) = \Lambda(r_b(\xi),\xi) \,. \tag{4.34}$$

The approximations would be valid for bubbles with large radii in the range of one plasma wavelength. For the Trojan Horse regime, however, it is not, as the radius is in the order of $\lambda_p/4$. Then, $S_{I,b}/2$ would be in the order of unity. We can compensate this by modifying the coefficient functions phenomenologically to

$$A(r_b) \approx 1 + \frac{S_{I,b}}{2} \,, \qquad B(r_b) \approx \frac{\rho r_b}{2} \,, \tag{4.35}$$

$$C(r_b) \approx \frac{S_{I,b}}{2r_b} \,, \qquad \Lambda(\xi) = \Lambda(r_b(\xi),\xi) \,. \tag{4.36}$$

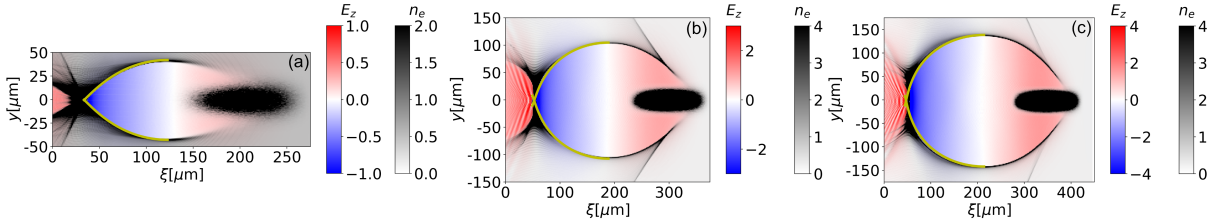

Figure 4.1: Simulations results for a bubble in homogeneous plasma that is being driven by a 1 GeV bi-Gaussian electron driver. The driving beam has peak density (a) $|\rho_e| = 3$, (b) $|\rho_e| = 24$, (c) $|\rho_e| = 48$. The yellow line corresponds to the solution of the differential equation that describes the bubble border very well. For all simulations $\lambda_p = 200$ μm. *Source: [89], licensed under CC BY 4.0.*

If we assume a non-loaded bubble, i.e. $\Lambda = 0$, we can find an analytical approximation to the ODE solutions, if we consider small $|\xi|$ near the bubble center. Then

$$r_b \approx R\,, \qquad r_b' \approx 0\,, \qquad r_b'' \approx -\frac{C}{A} \approx -\frac{S_{I,b}}{(2+S_{I,b})R}\,. \tag{4.37}$$

For the source integral we obtain

$$S_{I,b} = \frac{R^2}{2} \tag{4.38}$$

in the case of homogeneous plasma and finally for the bubble radius

$$r_b \approx R - \frac{1}{1+4R^{-2}}\frac{\xi^2}{2R}\,. \tag{4.39}$$

Looking at the solution of the ODE (yellow line), we can see that a proper choice of the parameters Δ and R leads to an adequate fit of the analytical approximation in the bubble middle, but the bubble back is not resolved very well (cf. Fig. 4.1). The main problem, however, is that the longitudinal field bears a divergence at the bubble stern that is not described by this model since E_z is proportional to r_b', but r_b' is very flat (Fig. 4.2).

4.4 Field modulation near bubble back

If we want to consider the longitudinal electric field E_z for a bubble in homogeneous plasma, a simplified expression can be obtained when a thin electron sheath is assumed, namely

$$E_z = -S_{I,b}\frac{r_b'}{r_b}\,. \tag{4.40}$$

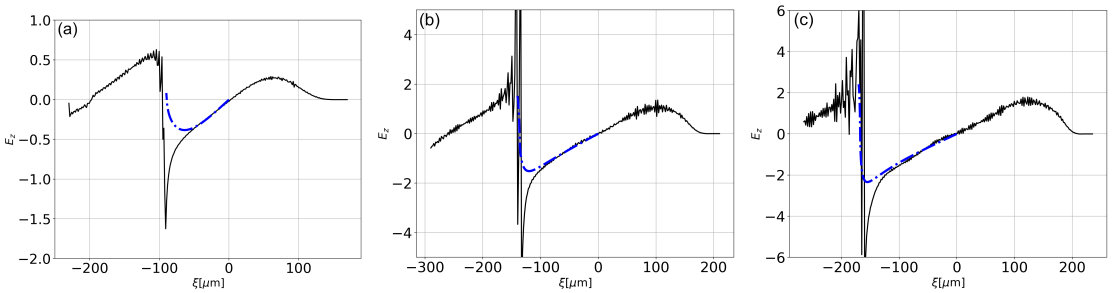

Figure 4.2: The longitudinal electric field E_z in dependence of the coordinate ξ (black line). The data in (a)-(c) is taken from the corresponding PIC simulations at the line $y = 0$ μm. The blue line shows the results of the model without the fix applied. It is clearly visible that the bubble middle is described well but not the back at $\xi \leqslant -100$ μm. *Source: [89], licensed under CC BY 4.0.*

Approximating the field by its lowest order for small values of ξ we find

$$E_z \approx E_0 \xi \tag{4.41}$$

with

$$E_0 = \frac{1}{2 + 8R^{-2}} \, . \tag{4.42}$$

Here, $|\mathrm{d}E_z/\mathrm{d}\xi| \leqslant 1/2$, which is the upper limit of large bubbles with $R \gg 1$. Similarly, the derivative is limited by zero (the lower limit for small amplitude bubbles with $R \ll 1$). We find in PIC simulations that this description – while being in good agreement with the fields in the bubble mid – does not describe the divergence of the electric field at the bubble back. This can be due to electron currents at the stern which we have neglected thus far. These would change the decrease of the bubble radius in that region more significantly.

In order to augment this behaviour, we assume that the field diverges at $L = \xi(r_b = 0)$. We introduce a function

$$f(\xi) = \left(\frac{L}{L - \xi} \right)^{1/m} = \frac{1}{\sqrt[m]{1 - \frac{\xi}{L}}} \tag{4.43}$$

with $m \in \mathbb{R}$ which shall modify the field such that the divergence is incorporated in the bubble back while leaving the field in the middle intact. Looking at the limits

$$\lim_{\xi \to L} f(\xi) = \infty \, , \qquad\qquad f(\xi \approx 0) \approx 1 \, , \tag{4.44}$$

we find that this function is able to do this. If the parameter m is chosen heuristically from

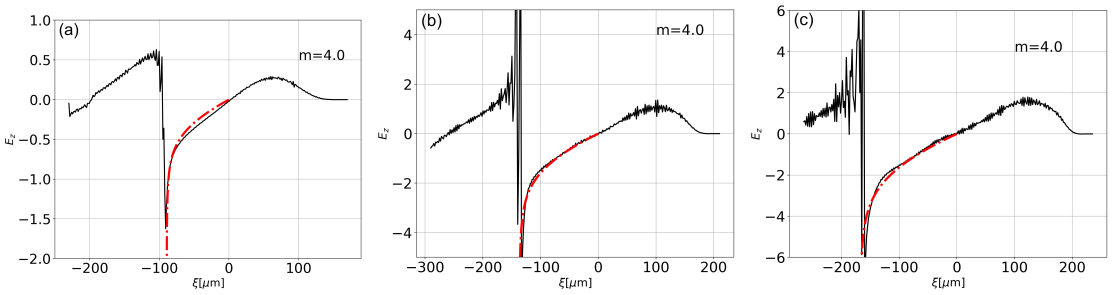

Figure 4.3: Longitudinal electric field for the three previously shown cases (a)-(c). The red line corresponds to the field obtained using the ansatz including the fix with $m = 4$. In all of the cases, the model incorporates the divergence towards $\xi \leqslant -100$ μm very well. *Source: [89], licensed under CC BY 4.0.*

the interval $m \in [3, 4]$, we find that the function's influence on the bubble mid is reduced to a satisfactory extent, while still bearing the divergence seen in PIC simulations.

Thus, the "fixed" fields are

$$E_z = \frac{E_0 \xi}{\sqrt[4]{1 - \frac{\xi}{L}}} , \qquad B_\varphi = -\frac{r}{2} \frac{E_0(4L - 3\xi)}{4L \sqrt[4]{1 - \frac{\xi}{L}}^5} , \tag{4.45}$$

and the corresponding forces (calculated via the general theory) are

$$F_z \approx -\frac{E_0 \xi}{\sqrt[4]{1 - \frac{\xi}{L}}} , \qquad F_r = -\frac{r}{2} + \left(1 - \frac{p_z}{\gamma}\right) \frac{E_0(4L - 3\xi)}{4L \sqrt[4]{1 - \frac{\xi}{L}}^5} . \tag{4.46}$$

As we quite clearly see in Fig. 4.3, this fix to our model is able to much better incorporate the divergence in the longitudinal electric field.

4.5 Self-consistent bubble border calculation

While the ODE (4.29) works very well for describing the bubble boundary in many cases, solving it has the additional "challenge" that the initial conditions for r_b, r_b' have to be obtained from PIC simulations. A much nicer way of solving this equation would be to do it in a self-consistent manner, i.e. simply by specifying a driver analytically. We have investigated this in [92].

Again, we start from the ODE for the bubble boundary (4.29) introduced in the previous sections. In the approximation that the sheath electrons are ultra-relativistic, we have $\Delta \ll r_b$ and $\Delta \gg r_b^{-1}$. In this case, we have $\beta \ll 1$ and $\beta r_b^2 \gg 1$. The ODE can then be

brought into the much simpler form

$$r_b \frac{\mathrm{d}^2 r_b}{\mathrm{d}\xi^2} + 2\left(\frac{\mathrm{d}r_b}{\mathrm{d}\xi}\right)^2 + 1 = 2\kappa(\xi, r_b) \ , \tag{4.47}$$

where $\kappa(\xi, r) = 2\Lambda(\xi, r)/r^2$. For a vanishing value of r, it follows from the definition of $\Lambda(\xi, r)$ that

$$\lim_{r\to 0} \kappa(\xi, r) = -\rho_B(\xi, 0) \ . \tag{4.48}$$

The function ρ_B describes the charge density of the beams prevalent in the setup. From our relativistic approximation we can infer that $r_b \gg 1$. Because of this, the equation should be invalid where r_b is close to zero. In the following, we describe why it is still usable here.

For the region along the ξ-axis where no bunches are present, we are able to define a first integral of the simplified ODE, namely

$$I_0(\xi) = \pi \frac{r_b^4}{16}\left[1 + 2\left(\frac{\mathrm{d}r_b}{\mathrm{d}\xi}\right)^2\right] = \pi \frac{R_b^4}{16} = \text{const.} \ , \tag{4.49}$$

where in the last step we have used that the bubble has a maximum radius of $r_b = R_b$ and at that position r_b' vanishes. In the case that $\kappa \neq 0$, the integral becomes

$$\frac{\mathrm{d}I_0}{\mathrm{d}\xi} = \frac{\pi}{2} r_b^3 \frac{\mathrm{d}r_b}{\mathrm{d}\xi} \kappa(\xi, r_b) \ . \tag{4.50}$$

Integrating the equation above and taking into account that

$$E_z(\xi) = \frac{r_b}{2}\frac{\mathrm{d}r_b}{\mathrm{d}\xi} \ , \tag{4.51}$$

we obtain

$$I_0(\xi) - I_0(\xi_0) = -2\pi \int_{\xi_0}^{\xi} \int_0^{r_b} E_z(\xi')\rho_B(\xi', r') r' \, \mathrm{d}r' \mathrm{d}\xi' \ . \tag{4.52}$$

The expression on the right-hand side approximately corresponds to $-\int \mathbf{j}_B \cdot \mathbf{E} \, \mathrm{d}V$, i.e. the power of the energy exchange between the bubble's electric field and the bunch between ξ_0 and ξ. This means, that I_0 can be understood as a measure of energy density in the bubble. For example: for the witness beam and an accelerating field $E_z < 0$, I_0 decreases with ξ. The interpretation of this is that the energy of the bubble is expended on acceleration. By comparison, for $E_z > 0$, ξ increases, i.e. the driver pumps the bubble.

If we introduce the local effective size of the bubble,

$$R_{\text{eff}}(\xi) = 2\,(I_0/\pi)^{1/4} \ , \tag{4.53}$$

and use dimensional values, we obtain

$$I_0 = \frac{m^2c^5}{4\pi e^2}\frac{(k_p R_{\text{eff}})^4}{16} \ . \tag{4.54}$$

We can further see that

$$I_0(\xi) - I_0(\xi_0) = P = -\int \mathbf{j}\cdot\mathbf{E}\,\mathrm{d}V \ , \tag{4.55}$$

i.e. I_0 is a power (of the energy loss by the driver or the maximum possible acceleration power achievable, respectively).

Going back to the ODE, we had remarked that a numerical solution from $r_b = 0$ is difficult since then the second derivative diverges. In order to circumvent this, we substitute

$$\psi_\xi(\xi) = \frac{r_b^2(\xi)}{4} \ . \tag{4.56}$$

This removes the divergence while not introducing a zero-solution into the equation. Substituting in the ODE yields

$$\frac{\mathrm{d}^2\psi_\xi}{\mathrm{d}\xi^2} + \frac{1}{2\psi_\xi}\left(\frac{\mathrm{d}\psi_\xi}{\mathrm{d}\xi}\right)^2 = \kappa(\xi, 2\sqrt{\psi_\xi}) - \frac{1}{2} \ . \tag{4.57}$$

We now have to define initial conditions to fix the problem of excitation. Since $r_b(\xi_0) = 0$, we set $\psi_\xi(\xi_0) = 0$. Further, we assume that $\mathrm{d}r_b/\mathrm{d}\xi$, which means that the solution emerges at an angle of zero from the axis (this assumption is valid for driver with a longitudinal density growing continuously from zero). Together with the substituted ODE, we get the initial conditions

$$\psi_\xi(\xi_0) = 0 \ , \qquad\qquad \frac{1}{\psi_\xi}\left(\frac{\mathrm{d}\psi_\xi}{\mathrm{d}\xi}\right)^2\Big|_{\xi_0=0} = 0 \ . \tag{4.58}$$

Our substituted variable ψ_ξ is defined as positive. Thus, the right-hand side of the ODE needs to be positive as well. In turn, it follows that bubble excitation may only occur for

$$\kappa(\xi, 0) = |\rho_B(\xi, 0)| > \frac{1}{2} \ . \tag{4.59}$$

Generally, the solution of this ODE still needs to be obtained numerically. Having calcu-

lated $\psi_\xi(\xi)$, the other quantities are related via

$$r_b = 2\sqrt{\psi_\xi}\,, \qquad \frac{\mathrm{d}r_b}{\mathrm{d}\xi} = \frac{1}{\sqrt{\psi_\xi}}\frac{\mathrm{d}\psi_\xi}{\mathrm{d}\xi}\,, \qquad E_z = \frac{\mathrm{d}\psi_\xi}{\mathrm{d}\xi}\,, \tag{4.60}$$

$$I_0(\xi) = \pi\psi_\xi^2\left[1 + \frac{2}{\psi_\xi}\left(\frac{\mathrm{d}\psi_\xi}{\mathrm{d}\xi}\right)^2\right]\,. \tag{4.61}$$

Comparing to PIC simulations, we find that the bubble size is somewhat larger than expected but that the electric field is better described by the self-consistent model than solving from the bubble center. Further, the effect of driver density is the following: Since for weak drivers the assumption $r_b \gg 1$ does not hold, the agreement to PIC simulations is inadequate and our model predicts a spherical bubble instead of the physical, elongated form (not shown here). Increasing the driver density yields much better correspondence between the model and simulations, as the assumption now holds for a significant part of the bubble. Thus, we are able to describe bubble shape and accelerating field only using the driver's properties. In the publication [92], we further show an analytical solution to a specific, cylindrical driver which will be left out for reasons of brevity. As stressed before, for general drivers, we still need to solve the ODE in a numerical manner. From the obtained solutions we can also derive scaling laws for I_0, as well as the optimal plasma density and deceleration length for a driver of a certain charge and length. Additional, future work could consider the creation of models for positron or proton drivers which are not described correctly by our model due to the different excitation physics. A model describing LWFA in a self-consistent manner would be of interest as well.

4.6 Positron acceleration in a two-fold plasma column

While for electrons a beneficial region for acceleration in the wakefield structure is obvious, the same is more problematic for positrons. Due to their opposite charge, the positrons cannot be accelerated by the same field region in the bubble as the electrons were. The accelerating region for positrons is at the front of the bubble. However, a strong focusing field is missing there, thus preventing any proper acceleration from happening. In recent years, several setups for improved positron acceleration have been proposed. Some use donut-shaped electron drivers in order to create a proper region [93], others use drive bunches comprised of positrons or hollow plasma targets [94–96]. By Diederichs *et al.* a setup consisting of a finite-width plasma column has been proposed [97–100]. The electron driver creates a wake as usual, but the radius (and accordingly the fields) change due to

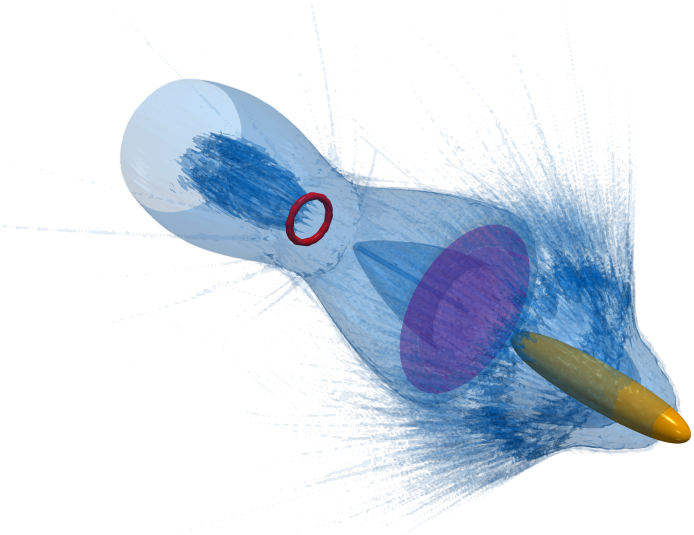

Figure 4.4: Three-dimensional schematic of the setup for positron acceleration. The particle driver (orange) expels electrons (blue). The second column is ionized by the ultra-short laser pulse (magenta). The positron ring (red) is placed in the back where the equilibrium line is found. *Source: [101].*

the fact, that for bubble radii exceeding the column width a different restoring force is acting. In turn, the bubble shape is changing. This acceleration mechanism was proven to be rather beneficial for positron acceleration, but some effects like driver evolution were disregarded in the first PIC simulations.

We have proposed further modification of this setup for a stronger focusing [101]. In our setup, we use two drivers that ionize a two-fold column structure: First, an electron driver ionizes a first column of radius r_1. With some delay, an ultra-short, weak laser pulse ionizes a second, wider ($r_2 > r_1$) column. Together, they form a structure like it is shown in Figure 4.4; the corresponding electromagnetic fields can be seen in Figure 4.5. Instead of a Gaussian positron witness beam, we will place a ring beam in the region where the focusing force vanishes (from now on referred to as the "equilibrium line"). We will see in our analytical model that this position coincides with the strongest accelerating field for that specific radial position.

In order to study our proposed scheme numerically, we use the quasi-static PIC code QV3D of our group. The advantages of quasi-static codes have been discussed in section 3.4. The simulation domain is of the size $16 \times 20 \times 20 k_p^{-3}$, where $k_p = 2\pi/\lambda_p$ is the plasma wave number. In the following, we use $\lambda_p = 75 \times 10^{-4}$ cm. The grid size is $h_x = h_y = h_z = 0.05 k_p^{-1}$ (note that for these simulations with QV3D a Maxwell solver based on the Fourier transform, not RIP, was used).

Initially, the box is filled with unionized Hydrogen gas with density $n_0 = 2 \times 10^{17}$ cm^{-3}. The Gaussian-shaped electron driver propagates in z-direction and has dimensions $\sigma_z =$

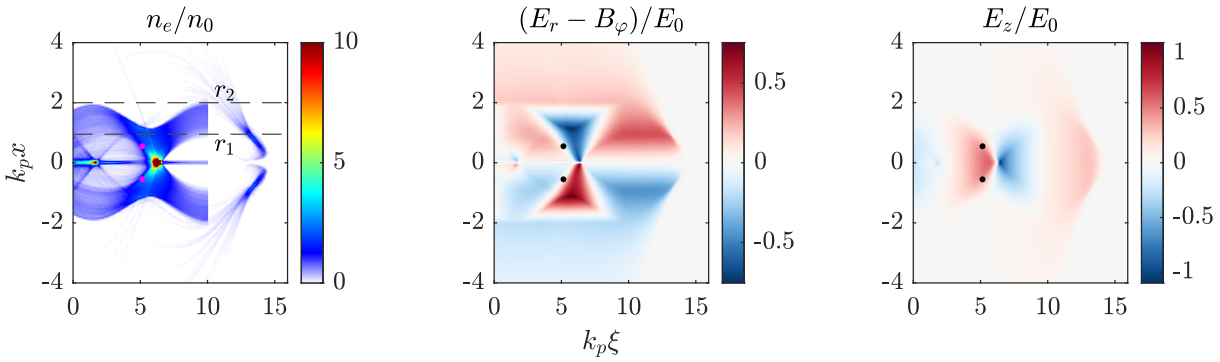

Figure 4.5: Results of PIC simulations for the laser-augmented blowout scheme. For better visibility, a laser pulse with only $w_0 = 17$ μm is used (the later setup uses $w_0 = 125$ μm). Left: The electron density, clipped at $10n_0$ exhibits a fork-like structure. The parameters r_1, r_2 are referred to in the analytical derivation. Middle/Right: the position of the positron ring coincides with the equilibrium line of the focusing force as well as with the maximum accelerating gradient. The positron ring position is denoted by the magenta/black dots. *Source: [101].*

12 μm, $\sigma_x = \sigma_y = 2.4$ μm. It has a peak density of $20n_0$ and the electrons have an initial momentum of $p_z = 10^4 m_e c$ with 5% longitudinal spread. The electron driver ionizes the first, smaller plasma column and excites a wakefield. The structure of this wakefield deviates from the wakefield in homogeneous density; the exact structure will be described more extensively in the analytical part.

The laser pulse for ionizing the second, wider column is circularly polarized, has a duration of $\tau_0 = 4.5$ fs and a wavelength of $\lambda_L = 400$ nm. In order to obtain a Rayleigh length in the cm range, we choose a focal spot size of $w_0 = 125$ μm. As the pulse is needed for the ionization of the second column, a normalized laser vector potential of $a_0 = 0.025$ suffices. A pulse like this could be created at the LWS-20 laser which has 16 TW peak power and 70-75 mJ pulse energy [102]. The usage of other radii is also possible: in Fig. 4.5, we show the simulation results for a $w_0 = 17$ μm pulse, although here only for better visibility of the fork-like structure. Smaller focal spots, however, come at the cost of a smaller Rayleigh length. Similarly, increasing the pulse length to avoid the ultra-short regime is possible, but will introduce an unwanted curvature of the ionization front. Ultra-short pulses further come with the indirect advantage that, due to the typically used optical parametric chirped-pulse amplification frontends, ionization from pre-pulses is reduced. We will therefore stay with the duration of 4.5 fs and waist of 125 μm.

For the description of the pulse, the envelope model is used. Tunnel ionization is incorporated according to the references [103, 104]. We further consider the refraction of the laser pulse over the course of the simulations which will be of interest for the stability discussion later on.

Right behind the electron driver, the field structure is similar to blowouts in homogeneous plasma. But, because only a narrow part of the gas is ionized, the fields extend over a comparatively greater distance. Looking at the focusing force $E_r - B_\varphi$ in the region $\xi = (5-7)k_p^{-1}$, we see a white line corresponding to a vanishing force (Fig. 4.5). This region is beneficial for positron acceleration as positrons on this line will be held there by the surrounding field, while experiencing a new maximum accelerating field E_z. Therefore, we will place the positron ring at this position. The density of the positron ring is varied in the range $(1-80)n_0$ for the various simulation runs. In all simulations, the initial radius is 6 μm with a thickness of 1 μm. The momentum of the positrons is $p_z = 10^4 m_e c$. Similarly structured positron beams could be created like the hollow electron beams from Laguerre-Gaussian modes in [105, 106].
In the following we will derive the analytical model in order to describe this laser augmented blowout (LAB) scheme.

4.6.1 Analytical model

We consider a plasma in the quasi-static approximation (with $\xi = t - z$) with the configuration

$$\rho_e(0,r) = \begin{cases} -1\ , r_1 < r < r_2 \\ 0\ , \text{else} \end{cases} \quad , \qquad \rho_i(\xi,r) = \begin{cases} 1\ , r < r_2 \\ 0\ , \text{else} \end{cases} \quad . \tag{4.62}$$

Ions in the area $[0, r_1]$ begin to attract outer electrons, and a wakefield is created for $\xi > 0$. Ions are considered immobile. The general derivation procedure is similar to [87]. The position $\xi = 0$ denotes the point where the laser pulse ionizes the plasma ring $r_1 < r < r_2$. As the problem has axial symmetry, such a wakefield can be described by the wakefield potential ψ and the azimuthal magnetic field B_φ:

$$\psi = \psi_0(\xi) - \int_r^{r_2} \frac{\mathrm{d}r'}{r'} \int_0^{r'} r''(j_z - \rho)\, \mathrm{d}r'' \ , \tag{4.63}$$

$$B_\varphi = \frac{1}{r} \int_0^r \left[j_z + \frac{\partial \psi}{\partial \xi^2} \right] r'\, \mathrm{d}r' \ . \tag{4.64}$$

The electric field components can be derived via

$$E_z = \frac{\partial \psi}{\partial \xi} \ , \qquad E_r = -\frac{\partial \psi}{\partial r} + B_\varphi \ . \tag{4.65}$$

The value of $\psi_0(\xi)$ represents some electrons which have been ejected to $r \gg r_2$ and which

generate a wakefield. The electrons in the wakefield have a conserved Hamiltonian which leads to the equation

$$\gamma - \psi - p_z = 1 - \psi(0, r_0) \,, \qquad \gamma = \sqrt{1 + p_r^2 + p_z^2} \,. \tag{4.66}$$

The initial distribution of the wakefield potential is

$$\psi(0,r) = \begin{cases} \psi_0(0) + \frac{r_1^2}{2} \ln\left(\frac{r_2}{r}\right) \,, r_1 < r < r_2 \\ \psi_0(0) + \frac{r_1^2}{2} \ln\left(\frac{r_2}{r_1}\right) + \frac{r_1^2 - r^2}{4} \,, r < r_1 \end{cases} \,. \tag{4.67}$$

Electrons satisfy the equations of motion

$$\frac{\mathrm{d}p_r}{\mathrm{d}t} = \frac{\partial \psi}{\partial r} + (p_z - 1) B_\varphi \,, \qquad \frac{\mathrm{d}r}{\mathrm{d}t} = \frac{p_r}{\gamma} \,, \tag{4.68}$$

$$\frac{\mathrm{d}p_z}{\mathrm{d}t} = -\frac{\partial \psi}{\partial \xi} - p_r B_\varphi \,, \qquad \frac{\mathrm{d}\xi}{\mathrm{d}t} = 1 - \frac{p_z}{\gamma} \,. \tag{4.69}$$

In the following, we will present two approximations for the transverse motion; once in the relativistic case and once for the non-relativistic, small-amplitude case. From the latter we will obtain the electromagnetic fields of the structure and the corresponding equilibrium lines.

Transverse motion approximation (relativistic case)

We assume that both the longitudinal derivative $\partial\psi/\partial\xi$ of the wakefield potential and the azimuthal magnetic field B_φ can be neglected. In this case, we have $p_z = 0$, $\xi = t$ and the electron motion is described by

$$\frac{\mathrm{d}p_r}{\mathrm{d}\xi} = \frac{\partial \psi}{\partial r} \,, \qquad \frac{\mathrm{d}r}{\mathrm{d}\xi} = \frac{p_r}{\gamma} \,. \tag{4.70}$$

Since the current density $j_z = 0$ vanishes, we are able to write

$$\frac{\partial \psi}{\partial r} = -\frac{1}{r} \int_0^r r' \rho(\xi, r') \, \mathrm{d}r' = -\frac{r}{2} - \frac{1}{r} \int_0^r r' \rho_e(\xi, r') \, \mathrm{d}r' \,. \tag{4.71}$$

For an electron with initial coordinate r_0, if inner and outer electrons never cross its trajectory, the value

$$\int_0^r r' \rho_e(\xi, r') \, \mathrm{d}r' = -\frac{r_0^2 - r_1^2}{2} = \text{const.} \tag{4.72}$$

Thus, its equation for p_r becomes

$$\frac{\mathrm{d}p_r}{\mathrm{d}\xi} = -\frac{r}{2} + \frac{r_0^2 - r_1^2}{2r} \, . \tag{4.73}$$

This motion corresponds to the potential

$$V(r) = \frac{r^2}{4} - \frac{r_0^2 - r_1^2}{2} \ln \frac{r}{r_0} \, . \tag{4.74}$$

We introduce the short-hand $\delta r := r - r_0$ and thus rewrite the equation to

$$\frac{\mathrm{d}p_r}{\mathrm{d}\xi} = -\frac{r_1^2}{2r_0} - \frac{\delta r}{2} \left(1 + \frac{r_0^2 - r_1^2}{r_0(r_0 + \delta r)} \right) \, . \tag{4.75}$$

Transverse motion approximation (non-relativistic small-amplitude case)

Let us assume that $|\delta r| \ll r_0$ and that the electron motion is non-relativistic. Then we can neglect the non-linear term in δr and get

$$\frac{\mathrm{d}^2 \delta r}{\mathrm{d}\xi^2} = -\frac{r_1^2}{2r_0} - \delta r \frac{2r_0^2 - r_1^2}{2r_0^2} \, . \tag{4.76}$$

The solution with initial conditions $\delta r(0) = 0, \mathrm{d}\delta r/\mathrm{d}\xi(0) = 0$ is

$$\delta r = -\frac{r_1^2 r_0}{2r_0^2 - r_1^2} \left[1 - \cos\left(\sqrt{1 - \frac{r_1^2}{2r_0^2}} \xi \right) \right] \, . \tag{4.77}$$

The condition of applicability of this model is

$$\frac{2r_1^2 r_0}{2r_0^2 - r_1^2} \gg r_0 \, , \qquad\qquad r_0 \gg \sqrt{\frac{3}{2}} r_1 \, . \tag{4.78}$$

Under these conditions we can also neglect r_1 in the equations of motion and obtain the simpler equation

$$\delta r = -\frac{r_1^2}{2r_0} (1 - \cos \xi) \, . \tag{4.79}$$

The amplitude of oscillations decreases with r_0, thus trajectory crossing never happens.

Let us now assume that this solution is valid for all electrons in the range $[r_1, r_2]$. In this case, for a particular value of ξ, all electrons are located between

$$r_{\min} = r_1(1 + \cos\xi) \ , \qquad r_{\max} = r_2 - \frac{r_1^2}{2r_2}(1 - \cos\xi) \ . \tag{4.80}$$

In this range, the electron density can be found as

$$\rho_e(\xi, r) = -\frac{r_0(\xi, r)}{r}\frac{\partial r_0}{\partial r}(\xi, r) \ , \tag{4.81}$$

where $r_0(\xi, r)$ is the initial coordinate of the electron which ended at the point (ξ, r). This function can easily be calculated as

$$r_0(\xi, r) = \frac{r + G(\xi, r)}{2} \ , \qquad \frac{\partial r_0}{\partial r} = \frac{r + G(\xi, r)}{2G(\xi, r)} \ , \tag{4.82}$$

where we have introduced the function

$$G(\xi, r) = \sqrt{r^2 + 2r_1^2(1 - \cos\xi)} \ . \tag{4.83}$$

Thus, the density becomes

$$\rho_e(\xi, r) = \begin{cases} -\frac{[r+G(\xi,r)]^2}{4rG(\xi,r)} \ , r_{\min} < r < r_{\max} \\ 0 \ , \text{else} \end{cases} \ . \tag{4.84}$$

Using $\rho_e(\xi, r)$, we can calculate the distribution of the potentials. First,

$$E_r = -\frac{\partial\psi}{\partial r} = \frac{r}{2} + \frac{1}{r}\int_0^r r'\rho_e(\xi, r')\,\mathrm{d}r' = \frac{r}{2} + \frac{1}{r}\int_0^{r_0(\xi,r)} \rho_e(0, r_0)r_0\,\mathrm{d}r_0 \ . \tag{4.85}$$

There are four areas for E_r, namely

$$E_r(\xi, r) = \begin{cases} \frac{r}{2} \ , r < r_{\min}(\xi, r) \\ \frac{r}{2} - \frac{r_0^2(\xi,r) - r_1^2}{2r} \ , r_{\min}(\xi, r) < r < r_{\max}(\xi, r) \\ \frac{r}{2} - \frac{r_2^2 - r_1^2}{2r} \ , r_{\max}(\xi, r) < r < r_2 \\ \frac{r_1^2}{2r} \ , r > r_2 \end{cases} \ . \tag{4.86}$$

Using the calculated E_r, we can also calculate the potential ψ,

$$\psi(\xi, r) = \int_r^{r_2} E_r(\xi, r')\, \mathrm{d}r' \,. \tag{4.87}$$

Here, we assume that the potential is equal to zero at r_2. The resulting wakefield in the different regions then becomes

$$\psi = \begin{cases} \frac{r_2^2 - r^2}{4} - \frac{r_2^2 - r_1^2}{2} \ln\left(\frac{r_2}{r_{\max}}\right) - \frac{r_{\max}^2 - r_{\min}^2}{8} \\ + \frac{2r_1^2(1+\cos\xi)}{8} \ln\left(\frac{r_{\max}}{r_{\min}}\right) - \frac{G_I(\xi, r_{\max}) - G_I(\xi, r_{\min})}{4} \,, r < r_{\min} \\ \frac{r_2^2 - r^2}{4} - \frac{r_2^2 - r_1^2}{2} \ln\left(\frac{r_2}{r_{\max}}\right) - \frac{r_{\max}^2 - r^2}{8} \\ + \frac{2r_1^2(1+\cos\xi)}{8} \ln\left(\frac{r_{\max}}{r}\right) - \frac{G_I(\xi, r_{\max}) - G_I(\xi, r}{4} \,, r < r_{\min} < r < r_{\max} \\ \frac{r_2^2 - r^2}{4} - \frac{r_2^2 - r_1^2}{2} \ln\left(\frac{r_2}{r}\right) \,, r_{\max} < r < r_2 \\ \frac{r_1^2}{2} \ln\left(\frac{r_2}{r}\right) \,, r > r_2 \end{cases} . \tag{4.88}$$

Here, we define

$$G_I(\xi, r) = \int G(\xi, r)\, \mathrm{d}r = \frac{rG(\xi, r)}{2} + r_1^2(1 - \cos\xi) \ln[r + G(\xi, r)] \,. \tag{4.89}$$

The accelerating field E_z can be calculated easily via the Panofsky-Wenzel theorem [107], which states that

$$\frac{\partial E_z}{\partial_r} = \frac{\partial E_r}{\partial \xi} \,. \tag{4.90}$$

Therefore, we first obtain

$$\frac{\partial E_r}{\partial \xi} = \begin{cases} 0 \,, r < r_{\min}(\xi) \\ -\frac{[r + G(\xi, r)] r_1^2 \sin\xi}{4 r G(\xi, r)} \,, r_{\min}(\xi) < r < r_{\max}(\xi) \\ 0 \,, r > r_{\max}(\xi) \end{cases} \tag{4.91}$$

and then integrate $E_z = \int_r^{r_2} \partial E_r / \partial \xi \, \mathrm{d}r$, yielding

$$E_z = \begin{cases} -\frac{r_1^2 \sin\xi}{4} \ln\left[\sqrt{\frac{r_2(r_1 - r_{\min})}{r_1(r_2 - r_{\max})}} \frac{r_{\max}}{r_{\min}}\right] \,, r < r_{\min}(\xi) \\ -\frac{r_1^2 \sin\xi}{4} \ln\left[\sqrt{\frac{r_2(G - r)}{(G + r)(r_2 - r_{\max})}} \frac{r_{\max}}{r}\right] \,, r_{\min}(\xi) < r < r_{\max}(\xi) \\ 0 \,, r > r_{\max}(\xi) \end{cases} . \tag{4.92}$$

We will compare the analytically obtained fields with PIC simulations, but will first calculate the equilibrium lines.

4.6.2 Equilibrium lines

Let us find the line $r_{\mathrm{eq}}(\xi)$ at which E_r turns to zero. There are two such places, the first one is between $r_{\min}(\xi)$ and $r_{\max}(\xi)$ and is determined by

$$r^2 - r_0^2(\xi, r) + r_1^2 = 0 \,. \tag{4.93}$$

To solve this equation, we solve it against r_0 by introducing

$$r = r_0 - \frac{r_1^2}{2r_0}(1 - \cos\xi) \,, \tag{4.94}$$

where we have used the definitions (4.82) and (4.83). Then, we get

$$r_0^2 - r_1^2(1 - \cos\xi) + \frac{r_1^4}{4r_0^2}(1 - \cos\xi)^2 - r_0^2 + r_1^2 = 0 \,, \tag{4.95}$$

$$r_0 = \frac{r_1}{2\sqrt{-\cos\xi}}(1 - \cos\xi) \,. \tag{4.96}$$

First, we see that the solution can only exist if $\cos\xi < 0$. Secondly, r_0 is limited by the values of r_1 and r_2. The condition that $r_0 \geqslant r_1$ is always true, but r_2 imposes another limitation on ξ,

$$-\cos\xi > \left(\frac{r_2}{r_1} - \sqrt{\frac{r_2^2}{r_1^2} - 1}\right)^2 \,, \tag{4.97}$$

or, if we solve for ξ,

$$\arccos\left[-\left(\frac{r_2}{r_1} - \sqrt{\frac{r_2^2}{r_1^2} - 1}\right)^2\right] < \xi < 2\pi - \arccos\left[-\left(\frac{r_2}{r_1} - \sqrt{\frac{r_2^2}{r_1^2} - 1}\right)^2\right] \,. \tag{4.98}$$

If r_2 is sufficiently large, this region will be close to the interval $[\pi/2, 3\pi/2]$. The equilibrium line is

$$r_{\mathrm{eq}} = r_1 \frac{1 + \cos\xi}{2\sqrt{-\cos\xi}} \,. \tag{4.99}$$

It is convenient to linearize E_r around this line. To do so, we write

$$\frac{\partial E_r}{\partial r}(\xi, r_{\mathrm{eq}}) = -\frac{4\cos^2\xi}{(1+\cos\xi)(1-3\cos\xi)} \,. \tag{4.100}$$

The focusing gradient can be arbitrarily large for small r. We can also calculate E_z along the equilibrium line. First of all, we calculate

$$G(\xi, r_{\mathrm{eq}}) = r_1 \frac{1-3\cos\xi}{2\sqrt{-\cos\xi}} \,. \tag{4.101}$$

In this case,

$$G(\xi, r_{\mathrm{eq}}) - r_{\mathrm{eq}} = r_1 \frac{-2\cos\xi}{\sqrt{-\cos\xi}} \,, \qquad G(\xi, r_{\mathrm{eq}}) + r_{\mathrm{eq}} = r_1 \frac{1-\cos\xi}{\sqrt{-\cos\xi}} \,. \tag{4.102}$$

Then, the longitudinal electric field E_z becomes

$$E_{z,\mathrm{eq}}(\xi) = -\frac{r_1^2 \sin\xi}{4} \ln\left[\frac{-4\cos\xi}{1-\cos^2\xi}\frac{r_2 r_{\max}}{r_1^2}\right] \tag{4.103}$$

$$= -\frac{r_1^2 \sin\xi}{4} \ln\left[\frac{-4\cos\xi}{1-\cos^2\xi}\frac{r_2^2}{r_1^2} - \frac{2\cos\xi}{1+\cos\xi}\right] \,. \tag{4.104}$$

The distribution is symmetrical with respect to $\xi = \pi$. The equilibrium line itself does not depend on the value of r_2, but the accelerating field does. Thus, if the highest possible accelerating gradient is wanted, r_2 should be increased. The field scales as $E_{z,\mathrm{eq}} \propto \ln(r_2/r_1)$, so the scaling is comparatively weak. Further, the scaling is only valid until r_2 reaches the radius at which the electrons expelled by the driver are.

4.6.3 Simulation results

If we compare the fields obtained analytically with the ones from PIC simulations, we can see that they are in good agreement (cf. Fig. 4.6). Along the dashed-dotted line showing the equilibrium line $r_{\mathrm{eq}}(\xi)$ the positron ring can be accelerated. Since r_{eq} stays close to $r_{\min}$, the acceleration occurs in almost the maximum field possible.

We also observe that the simulation field structure is not symmetric. The structure from our model, however, is since we neglect that the real oscillation period of electrons depends on their initial radial position. Taking this into account, the fit between analysis and simulations can be improved even further.

In order to understand the effect our scheme has on beam quality, we consider the nor-

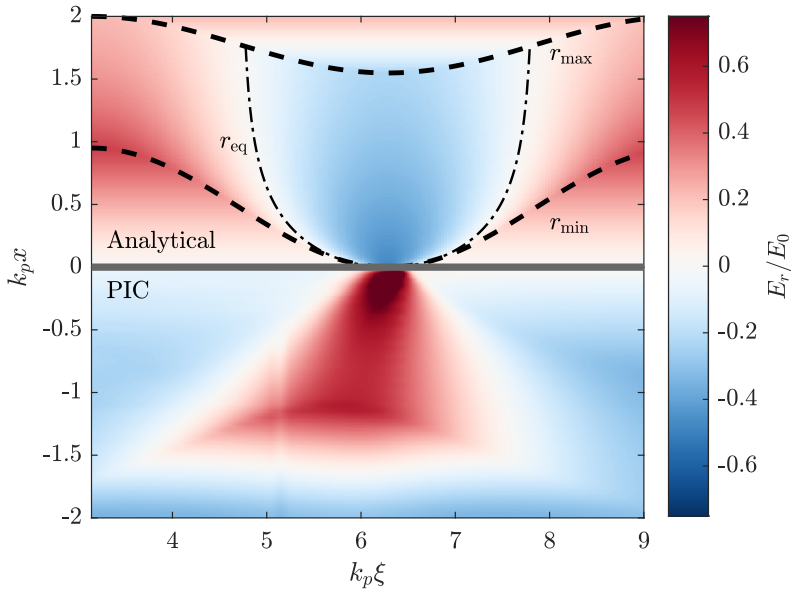

Figure 4.6: Comparison of the PIC simulation results with the analytically obtained radial field E_r. The dashed-dotted line corresponds to the equilibrium along which the positrons are accelerated. The color inversion between the two half planes is due to the (anti-)symmetry of the fields around $x = 0$. The vertical line at $\xi \approx 5k_p^{-1}$ in the PIC results stems from the fields of the witness beam. *Source: [101].*

malized root-mean-square (rms) emittance, which is defined as

$$\epsilon_x = \frac{1}{m_e c}\sqrt{\langle x^2\rangle\langle p_x^2\rangle - \langle x p_x\rangle^2} \tag{4.105}$$

or with y, p_y for ϵ_y. The operator $\langle\cdot\rangle$ denotes the second central moment of the positron distribution. The emittance of the witness beam increases over the course of the simulation (cf. Fig. 4.7). In the beginning ϵ_x and ϵ_y grow almost the same, but after approx. $10^4 T_0$ a significant difference can be seen. Towards the end of the simulation the slope of both curve flattens around a "saturation point" $\epsilon_x \approx 36\ \mu$m, $\epsilon_y \approx 27\ \mu$m. The difference between the two curves seems to indicate the presence of some plasma instabilities.

Additionally, we perform two separate simulations where we displace the positron ring either by one transverse or one longitudinal cell initially. The transverse shift only has minor effects on the final emittance, while a longitudinal displacement shows a more pronounced increase. Even stronger mismatching of the positron ring size with the plasma setup can even lead to the defocusing and loss of positrons besides the increase in emittance. The presented emittance values cannot directly be compared to typical Gaussian-shaped witness beams due to the inherently different geometry.

The accelerating gradient and the focusing force is shown in Fig. 4.8. The E_z commonly known from wakefield acceleration can bee seen; the gradient is $E_z \approx 38$ GV/m. Changing

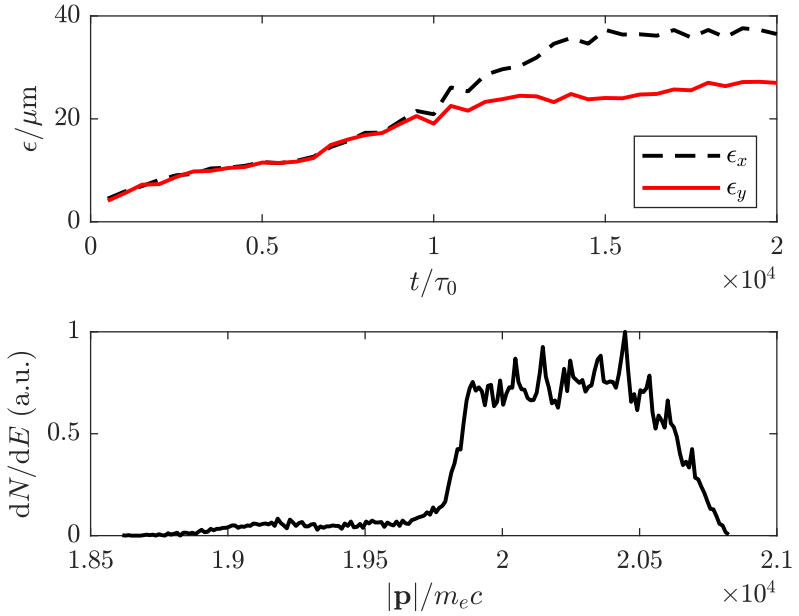

Figure 4.7: Emittance evolution for a $1n_0$ positron ring (top). The bottom plot shows the final momentum spectrum after $2 \times 10^4 T_0$. *Source: [101].* © *American Physical Society. Reproduced with permission. All rights reserved.*

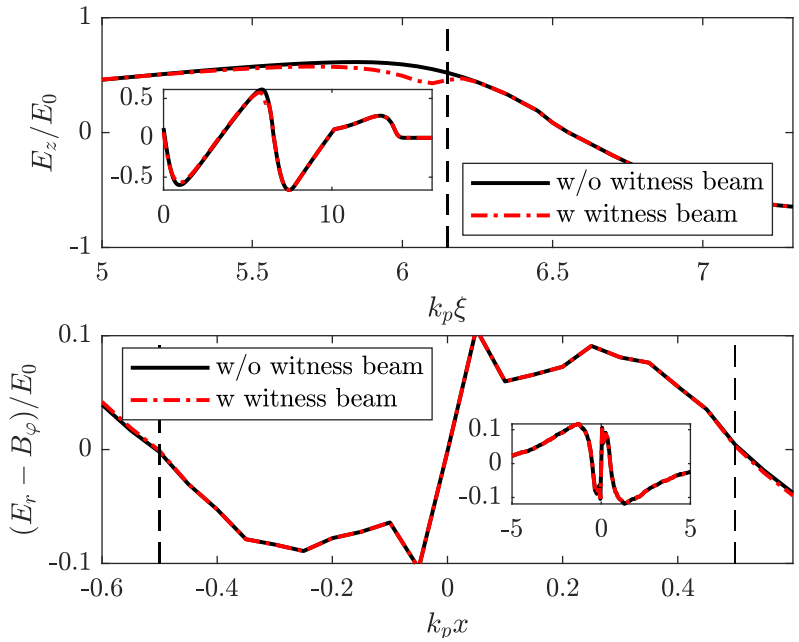

Figure 4.8: Accelerating (top) and focusing (bottom) field for simulations without a witness beam and with a $10n_0$ witness beam. The lineouts are taken at the positron ring's initial location (dashed lines). The larger-scale behaviour of the fields is shown in the insets. *Source: [101].* © *American Physical Society. Reproduced with permission. All rights reserved.*

the density and/or the dimensions of the witness beam can lead to flattening of the accelerating field in the surrounding area (see the difference between the lines with and without witness beam).

For a positron ring with $10n_0$, we are able to accelerate approx. 15 pC of positrons, while the driver has a charge of $n_{\text{driver}} \approx 670$ pC. After an acceleration over a distance of 24 cm, the mean energy of the witness beam is in the range of 10 GeV. The final energy spread is 1.7% (cf. Fig. 4.7). Up to 60 pC of witness beam can be accelerated with this structure; even higher densities lead to beam loading and loss of charge over time. Further, emittance and energy spectrum will be worsened.

For the stability and feasibility of the scheme, several other factors need to be discussed. Firstly, dephasing between the laser pulse and the witness bunch could potentially limit the achievable acceleration length. Our consideration of laser refraction throughout the simulations is in good accordance with analytical estimates. The laser group velocity can be approximate as $v_{\text{gr}} \approx 1 - n_0/(2n_{\text{cr}})$. For typical lasers with a wavelength of 800 nm this would correspond to a slip back of the laser by $1.8k_p^{-1}$ over the acceleration distance of 24 cm (assuming that the positron bunch moves with $v_z \approx c$). Accordingly, the entire field structure would move backwards with the laser, changing the equilibrium position for transverse focusing to be closer to the central axis. Moreover, the ionization front exhibits increases curvature over time. Both of the mentioned effects will increase emittance and could potentially destroy the ring structure altogether after some time. Going to the shorter wavelength of 400 nm used in simulations, we can improve on the slippage and thus on the scheme's stability.

Another effect to be considered is ionization defocusing due to the transverse plasma profile. Gibbon has derived that this effect becomes important if the condition

$$\frac{n_0}{n_{\text{cr}}} > \frac{\lambda_L}{\pi z_R} \tag{4.106}$$

is fulfilled [46]. Here, z_R denotes the Rayleigh length. In the case of our simulations, ionization defocusing would generally need to be considered. However, the LAB scheme does not rely on very strong fields or small spot sizes (recall that $w_0 = 125$ μm), so the effect would not be too detrimental in our use case. The laser only needs to be strong enough to ionize the second column with the larger radius $r_2 \gg r_1$. If, in the case of ionization defocusing occurring, the width of the second column would increase, this would even be beneficial for acceleration (cmp. Eq. (4.104)).

Beam head erosion is another effect that could be detrimental to the scheme: over the course of propagation, the driving beam ionizes the gas, leading to an eroded head. As shown by Li *et al.*, the rate with which the ionization front moves back over time depends

on several factors, including the gas species and the Lorentz factor of the bunch [108]. Some options for the mitigation are given by An *et al.*, e.g. decreasing the driver's emittance or using a gas with lower ionization threshold [109].

One last effect we might need to consider is the delay of electron driver and laser pulse. However, simulations where the delay is changed, show that it does not affect the scheme too much since the initial bubble fields are not too important for the positron dynamics.

In total, the LAB scheme is able to accelerate positrons over distances of tens of centimeters even when considering potentially detrimental effects like driving beam evolution and laser refraction.

4.7 Structured witness beams

Up to now we have mainly been interested in the shape of the blowout boundary and the corresponding fields. Only in the case of our positron setup, we have investigated the evolution of the witness beam. We have, however, not looked at the microscopic structure of the witness beam more closely. We know from the theoretical results that the bubble/blowout fields act focusing, i.e. ideally all of the particles would be confined to a singular point. This is obviously not the case. One of the counter-acting effects is the repelling Coulomb interaction between the electrons of the witness beam. In thermal equilibrium, both of these effects together should lead to a periodic structure of the electrons which is called a *Wigner crystal* in solid-state physics [110]. Structures like this have been proposed for conventional rf-based ring accelerators [111] and more recently also for wakefield accelerators. In the original publication by Thomas *et al.* [112], the equilibrium structure in the witness beam has been determined taking into account the retarded Liénard-Wiechert potentials of the electron interaction. There, however, a Taylor expansion in v/c was used which assumes that the electron velocity is small compared to the speed of light. This is generally not the case for *accelerated* electrons and was fixed in subsequent publications whose results we shall briefly summarize in the following.

4.7.1 Equilibrium slice model

In the first follow-up publication [113] to the results by Thomas *et al.*, the Lagrangian of a particle in electromagnetic fields known from standard literature like [114] together with simple wakefield of [61] was used as a basis for the description. If we assume that the term describing the interaction of the electrons is only a perturbation, we can calculate the Hamiltonian from the Lagrangian by simply changing the signs of the contributions.

The Hamiltonian is found to be

$$\mathcal{H} = \sum_{i=1}^{n} \left[\gamma_i + q_i \psi(\mathbf{r}_i) - p_{i,z} + \sum_{i>j} \left(1 - \frac{p_{i,z} p_{j,z}}{\gamma_i \gamma_j} \right) q_i \varphi_{ij} \right] , \tag{4.107}$$

where ψ is the wakefield potential and φ_{ij} is the scalar Liénard-Wiechert potential between particles i and j. Variables with index j are given at the retarded time $t_j = t - |\mathbf{r}_i(t) - \mathbf{r}_j(t_j)|$. If we want to find the energetic minimum of the system, we can use the gradient of the Hamiltonian

$$\begin{aligned} \nabla_{i\perp} \mathcal{H} =& \frac{1}{2} \begin{pmatrix} x_{i,0} \\ y_{i,0} \end{pmatrix} + \sum_{j \neq i} \left(1 - \frac{p_{i,z} p_{j,z}}{\gamma_i \gamma_j} \right) \nabla_{i\perp} \varphi_{ij} \\ & - \sum_{j \neq i} \varphi_{ij} \left[\frac{p_{i,z}}{\gamma_i} \left(\frac{\partial}{\partial p_{j,z}} \frac{p_{j,z}}{\gamma_j} \right) \frac{\partial p_{j,z}}{\partial t_j} \nabla_{i\perp} t_j + \frac{p_{j,z}}{\gamma_j} \nabla_{i\perp} \frac{p_{iz}}{\gamma_i} \right] , \end{aligned} \tag{4.108}$$

where $\nabla_{i\perp} = \mathbf{e}_x \partial_{x_i} + \mathbf{e}_y \partial_{y_i}$. The derivatives of the retarded time are found numerically. The equilibrium structure was found by using the method of steepest descent which we will further explain in the scope of our research in the following. It was found that the electrons in the 2D model will form a hexagonal lattice which is the closest sphere packing in two dimensions [115]. This is to be expected from the 2D setup, as the electrons all are placed on the same ξ-position, i.e. most of the relativistic effects can be neglected. Since the crystalline structure is hexagonal, but the bubble is spherical, some transition between the different geometries must be found. This is done by introducing so-called *topological defects* into the structure, where the number of nearest neighbours is changed from the usual six. A more extensive discussion of these defects in general can be found in [116].

4.7.2 Force equilibrium model

Instead of the Hamiltonian-based equilibrium slice model, we can also choose to look at the equilibrium between the focusing bubble force and the repelling Coulomb interaction. The fact that this alternative description is possible was already discussed by us in [117, 118]. The force can be written in terms of the Lagrangian as

$$\frac{\mathrm{d}\mathbf{p}_i}{\mathrm{d}t} = \frac{\mathrm{d}}{\mathrm{d}t} \nabla_{\mathbf{v}_i} L = \nabla_{\mathbf{r}_i} \mathcal{L} \, . \tag{4.109}$$

Now, we may split the expression into two parts, one describing the external force, the other the Coulomb interaction:

$$\frac{\mathrm{d}}{\mathrm{d}t}\mathbf{p}_{\mathrm{ext},i} = \nabla_{\mathbf{r}_i}\mathcal{L}_{\mathrm{ext},i} + \nabla_{\mathbf{r}_i}\mathcal{L}_{C,i} - \frac{\mathrm{d}}{\mathrm{d}t}\mathbf{p}_{C,i} \ , \tag{4.110}$$

$$\frac{\mathrm{d}}{\mathrm{d}t}\mathbf{p}_{C,i} = \nabla_{\mathbf{r}_i}\mathcal{L}_{\mathrm{ext},i} \ . \tag{4.111}$$

Finally, the force can be written as

$$\mathbf{F}_i = \frac{\mathrm{d}}{\mathrm{d}t}\mathbf{p}_{\mathrm{ext},i} - \frac{q_i}{c}\frac{\mathrm{d}}{\mathrm{d}t}\mathbf{A}(\mathbf{r}_i) + \left(\nabla_{\mathbf{r}_i} - \frac{\mathrm{d}}{\mathrm{d}t}\nabla_{\mathbf{v}_i}\right)\mathcal{L}_C \ . \tag{4.112}$$

The first two terms in Eq. (4.112) correspond to the Lorentz force of the external fields acting on the particle, whereas the last term describes the force from interaction with other particles. As a basis for the retarded Coulomb interaction we will again have to use the Liénard-Wiechert potentials

$$\Phi(\mathbf{x},t) = \left[\frac{e}{1-\boldsymbol{\beta}\cdot\mathbf{n}}\right]_{\mathrm{ret}} \ , \qquad \mathbf{A}(\mathbf{x},t) = \left[\frac{e\boldsymbol{\beta}}{1-\boldsymbol{\beta}\cdot\mathbf{n}}\right]_{\mathrm{ret}} \tag{4.113}$$

as the base of our calculations. Following the standard derivation by Jackson [119], we are able to find that the electromagnetic fields due to Liénard-Wiechert potentials equate to

$$\mathbf{E}(\mathbf{x},t) = e\left[\frac{\mathbf{n}-\boldsymbol{\beta}}{\gamma^2(1-\boldsymbol{\beta}\cdot\mathbf{n})^3R^2}\right]_{\mathrm{ret}} + \frac{e}{c}\left[\frac{\mathbf{n}\times((\mathbf{n}-\boldsymbol{\beta})\times\dot{\boldsymbol{\beta}})}{(1-\boldsymbol{\beta}\cdot\mathbf{n})^3R}\right]_{\mathrm{ret}} \ , \tag{4.114}$$

$$\mathbf{B}(\mathbf{x},t) = [\mathbf{n}\times\mathbf{E}]_{\mathrm{ret}} \ . \tag{4.115}$$

Here, the index "ret" denotes that the variables are given at the retarded time. The vector $\mathbf{n}$ is the unit vector pointing from the source charge to the observer and R is their distance. Similarly to the Hamiltonian approach, we will iteratively minimize the force on all the particles to obtain the equilibrium solution. It is found that in two spatial dimensions the hexagonal Wigner crystals persist, while in three dimensions the structure differs from classical (i.e. non-relativistic) close-packing of spheres: due to the relativistic effects in ξ the electron bunch is elongated in that direction. For a small number of particles, a single filament in ξ-direction can be observed. Increasing the particle number, not all particles fit into a single line for energy minimization, thus evading to other directions; the filament becomes somewhat helical. Further increasing the number of electrons leads to an "explosion" of the filament and the creation of an ellipsoidal shell. This process repeats for even more electrons and higher shells are being created. A full description of

this behaviour and the main influencing parameters is given in the works [117, 118].
The equilibrium configuration is found using the *resilient backpropagation* (abbrv. Rprop) algorithm. This algorithm works in a similar fashion to the method of gradient descent. In gradient descent, the gradient of the function to be minimized tells us the direction of steepest ascent; going in opposite direction thus leads us closer to the minimum value of the function. This process is done iteratively, i.e.

$$\mathbf{X}^{(k+1)} = \mathbf{X}^{(k)} - \alpha^{(k)} \nabla f^{(k)} \,, \tag{4.116}$$

where $\mathbf{X}^{(k)}$ denotes the position vector at the k-th step and $\alpha^{(k)}$ is the step size for that given iteration. The step size needs to be chosen carefully, as smaller steps take a long time to lead to convergence, while larger steps could "jump" over a minimum. In Rprop, the step size is chosen via

$$\alpha^{(k+1)} = \begin{cases} \min(\alpha^{(k)}\eta^+, \alpha_{\max}) \text{ if } \nabla f^{(k)} \cdot \nabla f^{(k-1)} > 0 \\ \max(\alpha^{(k)}\eta^-, \alpha_{\min}) \text{ if } \nabla f^{(k)} \cdot \nabla f^{(k-1)} < 0 \\ \alpha^{(k)} \text{ else} \end{cases} \,. \tag{4.117}$$

Here, $\eta^+ = 1.2$, $\eta^- = 0.5$, $\alpha_{\max} = 50$ and $\alpha_{\min} = 10^{-6}$ are the standard values which have been proven to deliver good results for a variety of problems [120]. It is further not guaranteed that the algorithm actually finds the global minimum of the problem, but rather one of several local minima.
This can further be investigated by adding small, random steps to the position vectors. Common methods are i.a. the Metropolis algorithm and simulated annealing [121, 122], where random steps (following some probability distribution function) are added at any iteration. This allows the function value to briefly worsen, get out of local minima, and reach the global minimum in the long run. For the case of structured witness beams, it was found in [117], that the structures found here actually correspond to the global minimum.

4.7.3 Effects of finite emittance

In the previously mentioned publications the electrons only carried momentum in ξ-direction, meaning that the beam's emittance would vanish completely. This does not give a physical picture: beams in experiment always exhibit some emittance which should generally be small for the best results in different applications. For the subject of the

structured electron bunches the question arises, whether finite emittance will destroy the periodic structure or whether it is able to persist.
Thus in a separate publication, the same model of [118] was used but for electrons that carry small, random momenta $\delta p_x, \delta p_y$ in the transverse direction. The mean value and standard deviation were varied in order to see at which range significant perturbations become apparent.
In the following, we define the normalized emittance as

$$\epsilon = \frac{p_\perp}{p_\parallel} \beta\gamma\delta \ . \tag{4.118}$$

Here, $p_\perp$, $p_\parallel$ denote the maximum transverse and longitudinal momentum of the electron distribution, δ is the witness beam's transverse diameter. As before, $\beta = v/c$ refers to the normalized particle velocity and γ to the corresponding Lorentz factor.
We implement finite emittance by considering an N-electron ensemble of which all the particles have the same longitudinal momentum $p_\parallel$ (i.e. in the propagation direction). In the transverse direction, we give a Gaussian distribution of the momenta. This distribution will be centered around $\mu_{p_\perp} = 0$ MeV$/c$ and has a standard deviation of $\sigma_{p_\perp}$.
Throughout the simulations, we vary $p_\perp/p_\parallel$ in the range of zero (no emittance, cold beam) to 10^{-2}. Momentum in the longitudinal direction is fixed to $p_\parallel = 10$ MeV$/c$.
The plasma wavelength is kept at $\lambda_p = 10^{-4}$ m. For a 1 nC electron bunch, the emittance would be in a range of up to $\epsilon = 2 \times 10^{-5}$ mm rad.

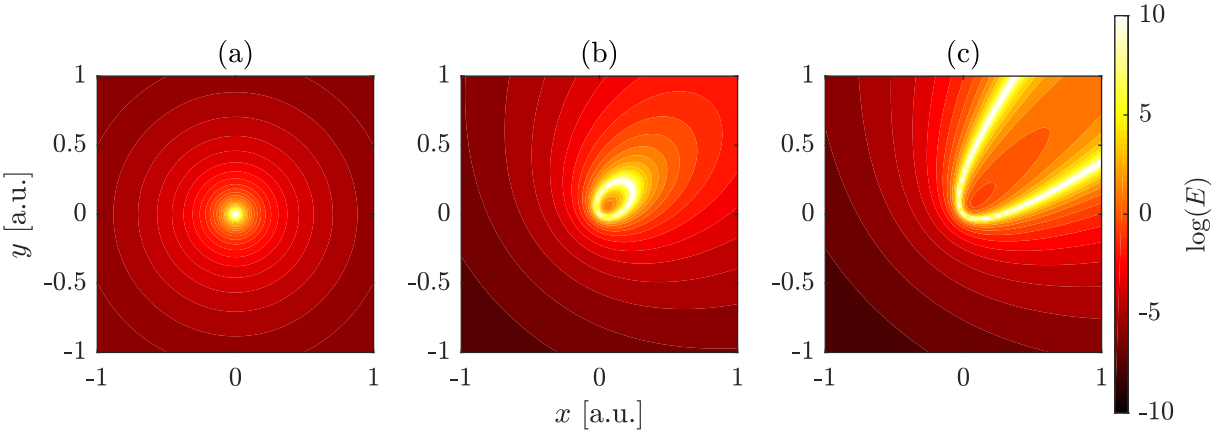

Figure 4.9: Electric field for a single electron moving in ξ-direction as seen by a test charge in dependence of the transverse emittance. (a) shows the case of zero/ultra-low emittance. (b) Increasing the emittance yields a change in the field structure, that becomes even more pronounced at higher emittance (c). *Source: [123].*

Let us first look into a simple setup consisting of only a single electron in the beam load with vanishing transverse emittance interacting with a test charge. The particle is

accelerated in ξ-direction and has a velocity close to the speed of light. As in previous investigations, we need to consider the Liénard-Wiechert potentials: the information about an electric field due to the presence of another electron needs to be transmitted. This transmission is limited to the vacuum speed of light c. Therefore, the electric field shows a cone-like structure. In Fig. 4.9, the logarithmic electric field in the x-y-plane is shown, i.e. the particle is moving in or out of the plane. This is why we only see one bright central dot in the case of zero/ultra-low transverse emittance: we are looking directly at the top of the cone (a). Introducing some tranverse momentum component in, the cone is tilted to the side due to the radial components in (b), (c). We are now able to see the cone shape in the cross section. Further, the cone widens, which also leads to a widening of the whole beam structure once multiple electrons are being considered.

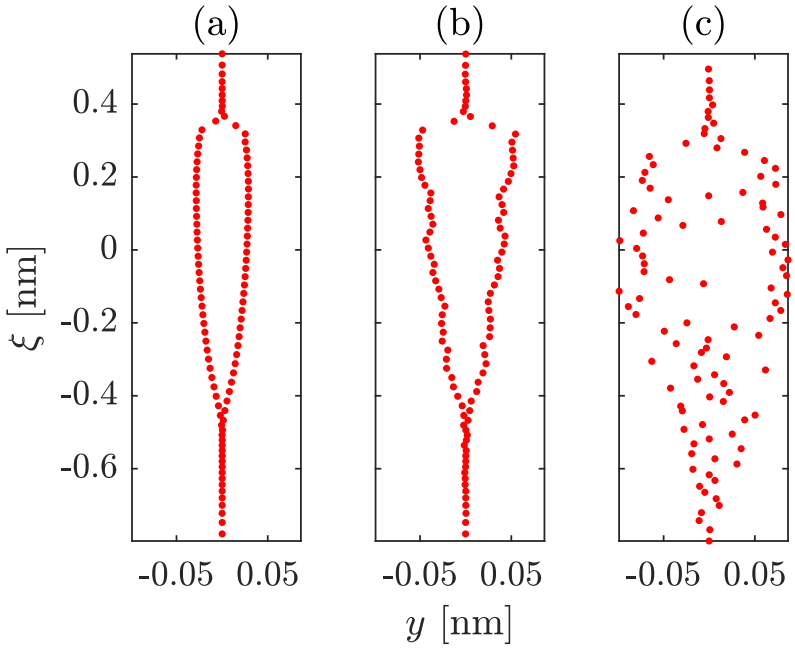

Figure 4.10: Equilibrium distribution for $N = 100$ electrons using different emittance ((a)-(c): low to high). For higher emittance values the distribution slowly starts to break up. *Source: [123].*

Now, we will investigate the effect of emittance on a structure of $N = 100$ electrons more deeply (cf. Fig. 4.10). For the lowest emittance of $p_\perp \approx 10^{-5} p_\parallel$ (frame (a)), the structure is basically indistinguishable from the case of zero emittance: We observe that the central filament is split up into two parts. This is not a consequence of the finite emittance, but rather of the amount of electrons that the prevalent forces try to fit into one structure. As it cannot go into a single filament, it splits up (this is also the reason for the formation of the electron shells for much larger N). Going to an increased $p_\perp \approx 10^{-4}$, we can see some changes starting to occur (frame (b)). While we still see a similar structure to the

previous case, the lines start to corrugate. This corrugation of the structure is to be expected from the changes in the electromagnetic fields. Increasing the emittance even further (e.g. to $p_\perp \approx 10^{-2} p_\parallel$ in frame (c)), the structure starts to break apart. The one feature of the original structure visibly persisting is the elongation in ξ-direction due to it being the direction of acceleration.

In our parameter scan we observe that the broadening of the crystal structure is linear in the emittance. This is clearly visible in Fig. 4.11 where we show the change in the mean distance (note that the axis corresponding to the emittance is given in logarithmic form there).

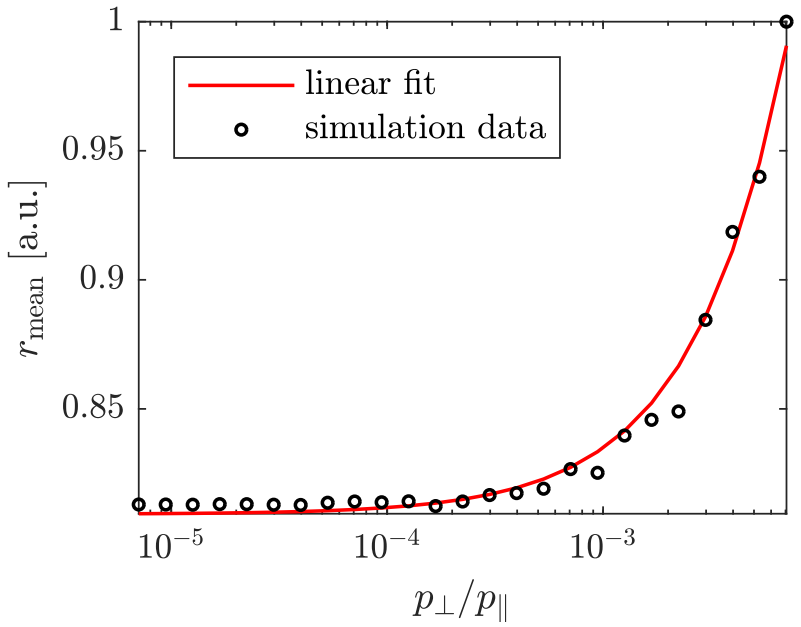

Figure 4.11: Mean distance in the equilbrium distribution in dependence of the emittance. *Source: [123].*

The corrugation of the structure would prevent the application of it for high-brightness gamma sources. However, the much higher number of particles in a physical system will even out some of the effects: for one, the random radial momenta of many particles can average out for the structure. Moreover, the different shells that arise for a larger amount of particles will press together the ones inside it, further improving the structure. The widening of the structure we have observed is similar to changing parameters like the longitudinal momentum $p_\parallel$, plasma wavelength λ_p or the particle number N like it was done in our previous studies [113, 118]. A next step in the study of the witness beam's crystalline structure would be the investigation of its dynamics.

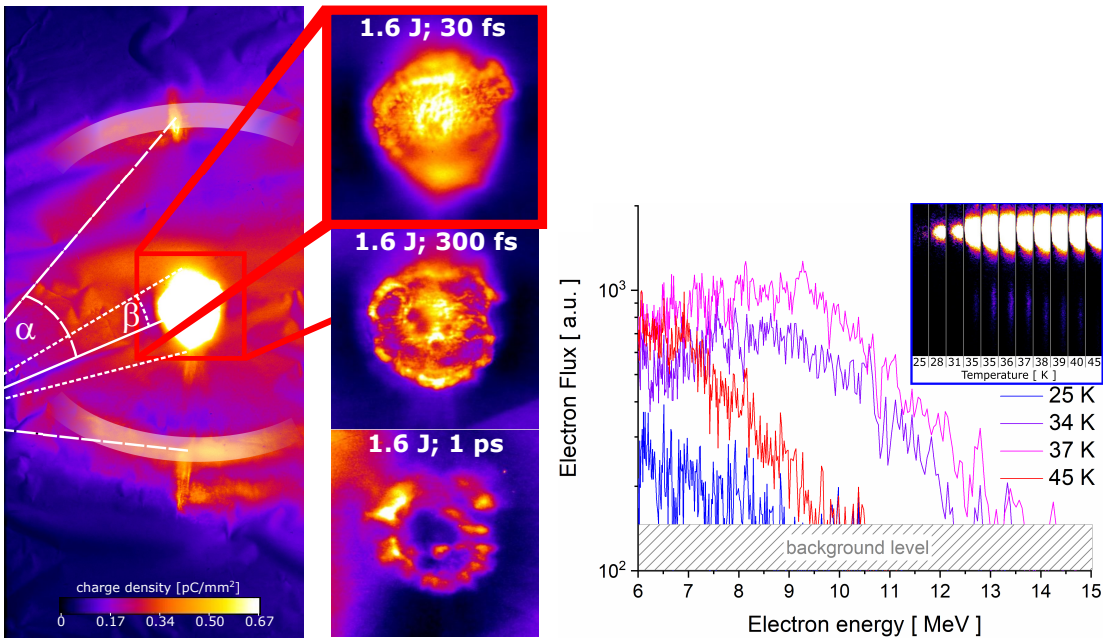

Figure 4.12: Left: Structure on the image plate with opening angles α, β displayed. The zoomed-in part shows the finer structure of the central spot for various pulse durations. Right: Experimentally obtained energy spectrum for different temperatures. *Source: [124], licensed under CC BY 4.0.*

4.8 Electron acceleration in clusters

Up to now, the setups we have looked at have consisted of a rather simple plasma target like a homogeneous plasma. Even in the case of the positron setup, the target is simply comprised of two plasma columns.

In a separate collaboration with the group of O. Willi, a more complicated target was used [124]. The target consists of cryogenic Hydrogen which is pumped through a de Laval nozzle. Depending on backing pressure, Hydrogen temperature and flow, Hydrogen clusters of different sizes can be created. For a certain parameter set, the distribution of cluster sizes can be approximated by a log-normal distribution (see [125–127] for more details on the target).

This target now has several strong differences to the aforementioned ones: one big factor is the highly localized density of the target. This means that figuring out whether a wake can be driven (and particles trapped) is harder to figure out than in the homogeneous case. Further, we will see some effects that we would not observe for simpler targets: a strong laser pulse is able to rip out many (or all) of the cluster's electrons, leaving behind an ionic cluster. Due to Coulomb interaction, these clusters will explode (thus, this process is aptly named *Coulomb explosion*). In the experiment, the ARCTURUS laser [128] was used for the interaction with the Hydrogen clusters. Different parameter scans, varying the pulse energy or the duration were performed. Further, different temperature and

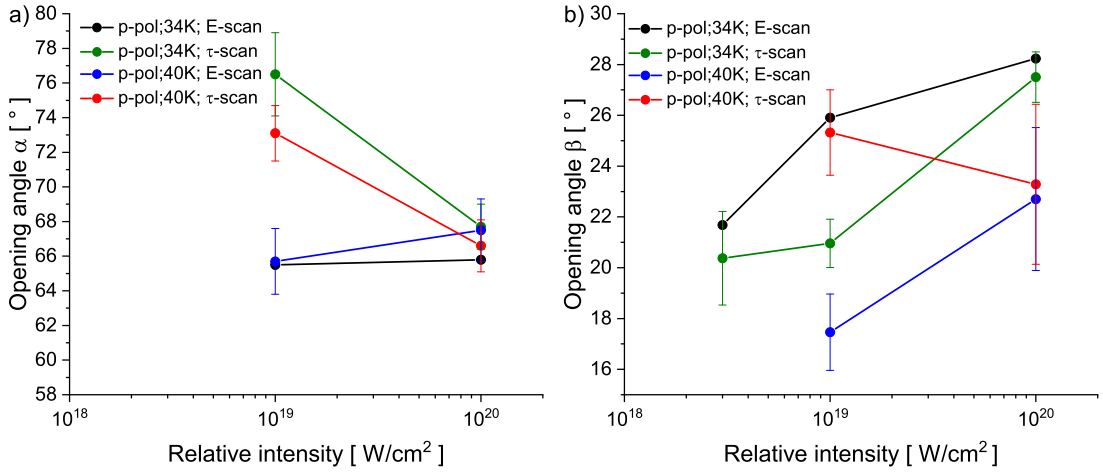

Figure 4.13: Opening angle α for the outer ring (a) and β for the central spot (b) for different temperatures in the energy and pulse duration scan. *Source: [124], licensed under CC BY 4.0.*

backing pressure of the cluster source were investigated. The spatial profile of accelerated electrons was recorded using Imaging Plates (IPs). In all of the cases, a ring-shaped structure was observed (cf. Fig. 4.12), while the additional central spot was only observed for some choices of laser-plasma parameters. The electron energies obtained were < 15 MeV. Both the outer ring-structure as well as the opening angle of the central spot are rather consistent throughout the E- and τ-scans (see Fig. 4.13) and no strong scaling can be observed. This behaviour was to be explained using simulations.

For our fully electromagnetic PIC simulations, we choose a simulation domain of size $(100 \times 46 \times 46)\lambda_L^3$ that is moving with the laser pulse ($\lambda_L = 800$ nm). The resolution is $h_x = 0.05\lambda_L$, $h_y = h_z = 0.1\lambda_L$ and $\Delta t = h_x/c$. The laser pulse parameters are based on the experimental values, i.e. $a_0 = 6.84$, $w_0 = 5$ μm, $\tau = 30$ fs. While longer (up to 100 fs) and/or weaker pulses were considered in experiment, many of those parameter regimes are computationally unwieldy for 3D-PIC.

In a first simulation, it is assumed that the clusters are placed periodically without any homogeneous background. The distance between clusters is $3\lambda_L$ in any direction. This value is approximated from the experimental electron density for 60 nm clusters. The clusters are simulated as being one cell large and consisting of 10^4 electrons and 500 protons (macro-particles). The smaller number of particles per cell for protons is chosen for reasons of computational effort. We inherently assume that the clusters have already expanded to some extent here, and set the density to be accordingly lower at approx. $5n_{\mathrm{cr}}$. We consider the clusters as being already fully ionized. This further reduces computational load while the electrons still can feel the potentials of the proton clusters. This target extends over a length of $375\lambda_L$. Focusing of the pulse is considered; the focal spot is in

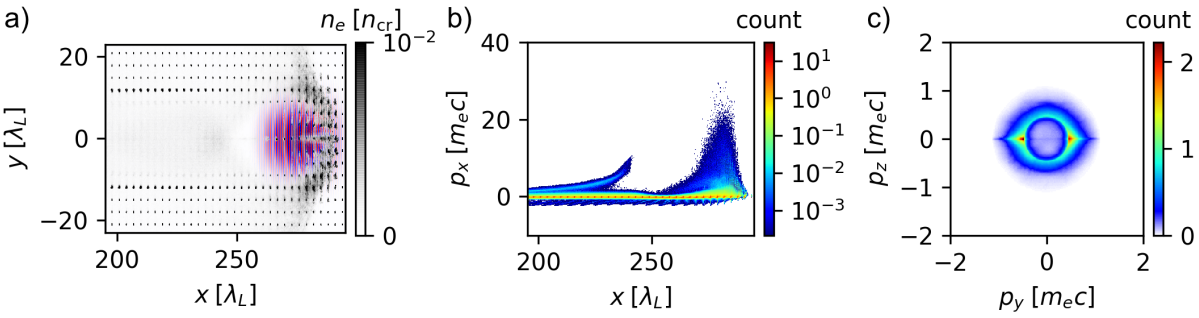

Figure 4.14: Simulations results for the laser pulse propagating through the cluster ensemble after $300T_0$. (a) The laser pulse expels electrons from the clusters via ponderomotive scattering, leaving behind a wakefield-like cavity. (b) Longitudinal momentum and (c) p_y-p_z phase space of the electrons (clipped for better visibility). *Source: [124], licensed under CC BY 4.0.*

the middle of the interaction volume.

The laser pulse rips electrons from the clusters and expels them in the direction transverse to its propagation. This leaves behind a cavity at the back of the laser pulse which is reminiscent of a bubble in wakefield. However, only a very minor amount of electrons is actually wakefield accelerated (see the region $x < 250\lambda_L$ in Fig. 4.14b)). As the accelerating gradient here is rather weak, no high-energy electrons are to be expected from this acceleration mechanism here.

We can, however, see that most of the electrons are actually accelerated directly by the laser pulse (see the phase space in Figs. 4.14b) and c)). Here, two mechanisms could potentially be important: direct laser acceleration (DLA) and ponderomotive scattering. For high-energy electrons from DLA, it is necessary that they stay in phase with the laser fields for as long as possible; a discussion about relevant parameters is given by Jirka *et al.* in [38]. In this simplified model it is, however, assumed that the plasma is homogeneous and that it does not change over time. In our case, the inhomogeneities due to plasma render this approximation useless. Further, the expected energies from DLA would by orders of magnitude larger than what we observe in both the PIC simulations as well as the experiment. For the simulations, we also see that the particles quickly lose their energy again, i.e. they are not effectively accelerated over a longer period of time. This brings us to the second possible process, ponderomotive scattering. This mechanism is due to the ponderomotive force of the laser pulse directly pushing electrons outwards. The process has been analytically considered in publications like [51] and [129]. Experimentally it was first observed for energies up to a few keV by Monot *et al.* [130] and to about 100 keV by Moore *et al.* [131]. Malka *et al.* have also used the process of ponderomotive scattering for an explanation of electrons observed in the MeV range [132].

From the analytical studies of this mechanism [51, 129], the following approximation for the scattering angle is given: given an electron initially at rest, i.e. with $\gamma \approx 1$, the angle is

$$\tan(\theta) = \frac{\sqrt{2(\gamma - \gamma_0 - 1)/(1 + \beta_0)}}{\gamma - \gamma_0(1 - \beta_0)} \,. \tag{4.119}$$

Here, $\beta_0 = v_0/c$ is the normalized velocity as usual. If the electrons have not been pre-accelerated, as it is the case in our simulations (the motion of the clusters should be negligible by relativistic standards), the approximation $\beta_0 \approx 0$ can be made (and accordingly $\gamma_0 \to 1$). This leads us to the simplified equation

$$\tan(\theta) = \sqrt{\frac{2}{\gamma - 1}} \,. \tag{4.120}$$

An approximation not visible from this equation itself we have to make for simplicity's sake is, that the electron is initially positioned on the central axis $y = 0$ and that it experiences the maximum laser electric field in its focus. In the experiment, the outer ring-structure was located at about 60°-80°. From equation (4.120), we get an energy range of 30 keV up to 300 keV. We calculate the same for the central spot: there, the measured angles were 16° to 30°, which yields energies of 3 MeV to 12 MeV. This fits the experimentally found energy spectra quite well. Differences from experiment are likely to be explained i.a. the positioning of the electrons with respect to the laser. As mentioned above, Eq. (4.120) assumes the electrons to be on the central axis and in the laser focus. Both of these assumptions are unlikely to be met by most of the electrons being scattered. Further, in the experiment there will be some amount of plasma background and clusters present whereas the formula is generally derived for acceleration in vacuum. The experimental laser parameters will also be subject to shot-to-shot fluctuations.

For the maximum obtainable electron energy from ponderomotive scattering, another equation from the publication [129] can be used:

$$\gamma_{\max} = \gamma_0 \left[1 + \frac{a_0^2(1 + \beta_0)}{2} \right] \,. \tag{4.121}$$

In case of our used parameters this would give $\gamma_{\max} \approx 24.4$ which is in good agreement with experimental and simulation data (cf. Figs. 4.12 and 4.15). We also look into the emission angles for certain energy ranges in our PIC simulations. Ponderomotive scattering in the simulations is almost completely radially symmetric which is to be expected from the form of the ponderomotive force. In Figure 4.14c) the p_y-p_z-plane for electrons with $1.1 \leqslant \gamma \leqslant 1.5$ is shown. There, an additional feature along the line $p_z = 0$ can be

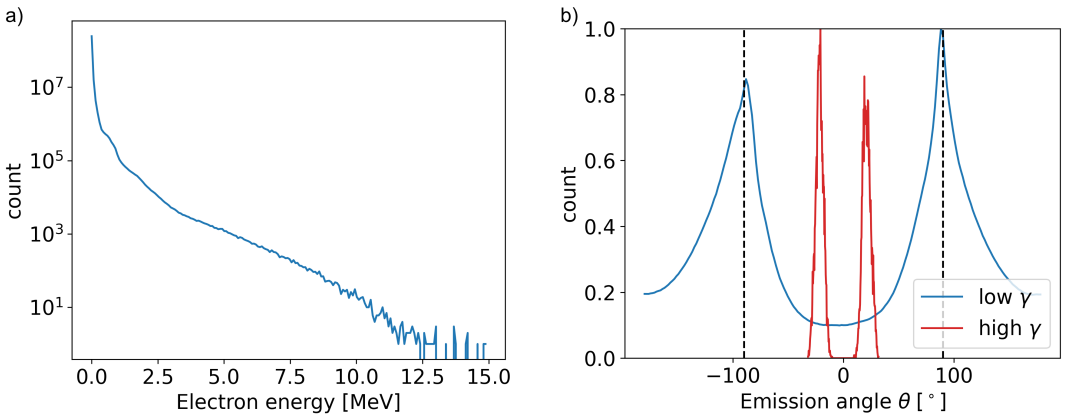

Figure 4.15: (a) Logarithmic energy spectrum of the electrons in the simulation box after $300T_0$. (b) Energy spectrum for the same time step. The blue line shows the distribution of electrons with $(20 - 160)$ keV, while the red line shows the distribution of the $(6 - 12)$ MeV electrons. The dashed lines correspond to angles of $\pm 90°$. *Source: [124], licensed under CC BY 4.0.*

observed. This stems for the laser's linear polarization; if we consider circular polarization, this feature disappears completely, leaving behind a fully symmetric picture. We show the emission angles for ranges 20 keV $\leqslant \mathcal{E} \leqslant$ 160 keV as well as 6 MeV $\leqslant \mathcal{E} \leqslant$ 12 MeV at $300T_0$ in Fig. 4.15. For this plot, the angle is defined as $\theta = \arctan(p_y/p_x)$ which leaves out the slight asymmetry due to the plane of laser polarization.

In the lower energy range, the electrons form a ring with an ejection angle of slightly below 90° which, again, is in good agreement with the experimental results. For higher energies, angles in the range 20°-30° are obtained. Note that in the plot both curves are normalized to 1 for better visbility. In a direct comparison, the forward signal would be much weaker here.

The angles and energy ranges obtained from this rather basic cluster model already fit the experimental data quite well. However, the actual physical picture is more complicated: before the main laser pulse interacts with the plasma target, the pre-pulse will already rip off some of the clusters' electrons and lead to partial Coulomb explosion in the target. The main pulse, arriving some picoseconds after the pre-pulse, will therefore see not a pure cluster target, but actually a target consisting of some approximately homogeneous background plus remnants of larger clusters. How important the consideration of pre-pulses for laser-plasma interaction in clustered targets was already described by Auguste *et al.* [133]. If we were to assume that we only have a homogeneous plasma target interacting with the peak pulse, ponderomotive scattering would still be responsible for most of the outer-ring electrons. The corresponding density (expanding all the clusters to fill the whole box) would be in the range 10^{16}-10^{17} cm^{-3}. In this regime, wakefield acceleration still is largely negligible (although, a lower number of particles per cell compared to the

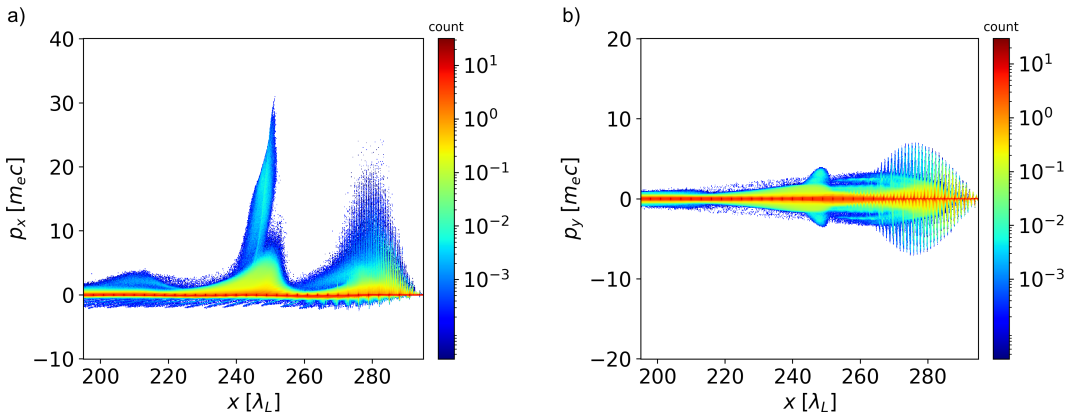

Figure 4.16: Phase space plots for simulations with a finite background density of $n_e = 5 \times 10^{17}$ cm^{-3}. (a) shows the x-p_x-plane, (b) the x-p_y-plane. Two electron populations, one from DLA and ponderomotive scattering, the other from wakefield acceleration, are present. *Source: [124], licensed under CC BY 4.0.*

simple cluster target have to be used here due to the huge box size). Again, only a few electrons would be accelerated at the wake's stern. The absence of any clusters also will lead to a decrease in the maximum energy.

The process of ponderomotive scattering is present even for longer pulse durations in the experiment which is why the outer ring-structure is always visible. There, the pre-pulse still homogenizes the target such that the peak pulse can interact with it and scatter the electrons outwards. When considering the longer pulses in experiment, the effective a_0 is lowered as the pulse energy is fixed throughout. Thus, the opening angle of the ring only changes slightly, but the shape of the cavity created by the peak pulse can change quite drastically. In turn, the trapping condition changes.

This means, that the laser pulse in the experiment neither sees a completely clustered target nor a completely homogeneous target: as alluded to earlier, it is likely to be an intermediate state. The pre-pulse will rip out some of the electrons in the clusters and induce Coulomb explosion. In turn, the clusters will expand, and the density profile will appear more homogeneous in the picoseconds afterwards. Still, not all clusters will be ionized completely or be completely ripped apart: some remnants will stay around in the interaction volume.

We study this with an additional simulation, where we take the clustered target from before and, on top, add a homogeneous background of $n_e = 5 \times 10^{17}$ cm^{-3}. While this strongly overestimates the experimentally available density, it shows the relevant processes quite clearly even for our statistical possibilities: as it is visible in Fig. 4.16, more electrons are now being accelerated at the back of the wake. For even higher densities, the E_x-gradient driving these electrons would be even stronger. Looking into the x-p_y-plane, we

see that these electrons also do not have a very large transverse spread, i.e. they will mainly contribute to the central spot.
This means that the apparent discontinuity visible on the IPs (strong outer ring, strong central spot, almost nothing in between) will occur for such an intermediate target. Only then do we have both the ponderomotive scattering responsible for the outer ring and also significant LWFA (and partly DLA) contribution to the central spot. A more detailed discussion about the effects of clusters on LWFA is given by Mayr *et al.* in [134, 135]. The clusters introduce highly localized potential difference that can give a kick to the electron momentum. This kick can be sufficient for the electron to be injected into the wake; how easily the particles can be injected depends on the clusters' charge density and diameter. The process behind this injection is similar to ionization injection [136]. There, however, different (or more specifically, heavier) particle species are used for injection also utilizing the local potential changes. Already, the obtained results fit the experimental data quite well. In theory, the data could be fitted even better if we were to consider a randomized position of the clusters. It was shown in [135] that this changes the results marginally and leaves the main features of the scheme intact.
We have seen in this section, that for clusterized targets only the consideration of several acceleration mechanisms at once gives a complete physical picture and that here the pre-pulse of the laser plays an important role that is often neglected in other simulations.

This concludes our investigations concerning the wakefield acceleration of leptons, more specifically electrons and positrons. As we have seen, it is possible to improve upon the models describing the bubble border in PWFA, even in a self-consistent fashion. The same theoretical foundation could be transferred to the positron setup which utilized both a particle and a laser driver for the acceleration of positron rings. Again, the analytical theory and simulations are in good agreement. Further, it was shown that structured witness beams in the form of Wigner crystals may persist even for finite emittance, although further work needs to be done with respect to the dynamics of those. Lastly, we have seen that structured targets like Hydrogen clusters lead to a plethora of other effects that need to be considered if the acceleration process is to be fully understood. In the next chapter, we will investigate the acceleration of spin-polarized proton beams.

Contributions of the author

In the publication [89] concerning the E-field divergence of the blowout, L.R. and J.T. worked together on the analytical framework in discussion with A.G. The manuscript was mainly written by L.R. The self-consistent model of [92] was developed by A.G. Here, L.R. checked the calculations and consulted A.G. in the writing process. For the positron setup [101], L.R. conducted the PIC simulations and wrote the manuscript; A.G. contributed the analytical calculations. In the publication about the Wigner crystals with finite emittance [123], L.R. wrote the code needed for finding the equilibrium structures and conducted the simulations. He was the main author of the manuscript in consultation with J.T. Lastly, for the experimental collaboration [124] concerning Hydrogen clusters, L.R. was responsible for the theoretical investigation: He conducted the PIC simulations and found the explanation for the process. L.R. wrote the introduction and the theoretical part of the paper, whereas B.A. was responsible for the experimental sections.

Chapter 5

Spin-polarized proton beams

So far, when talking about accelerated particles, we have only considered parameters like the final particle energy, the beam emittance and the beam charge. For some experiments, however, the particle spin can become essential, e.g. when looking at future QCD experiments [137], examining the nuclear structure of the proton [25] or even polarized fusion [26].
For conventional accelerators, some spin-related experiments have been looked at i.a. in [138]. Contrary to that, the research for spin-polarized particles in laser-plasma based setups has only just begun in the last couple of years [67]. In the following, we give a brief overview of the relevant effects that need to be considered and what kind of setups are feasible. Later on, we will specifically discuss the results presented in [139, 140], that examine further aspects of one specific proton acceleration scheme, Magnetic Vortex Acceleration. Throughout this chapter, spin is normalized to $\hbar/2$.

5.1 Spin-related effects

When considering spin in acceleration, there are three main effects that could become important. Here, we will give a brief explanation of what these effects are and why they have to be or do not have to be considered. In the end we are going to focus on only one effect, the spin precession in the presence of electromagnetic fields. An extensive review on the general topic of spin-polarized particle beams for accelerators was given by Mane *et al.* [141]; a discussion with several scaling laws specifically geared towards our studies has been written by Thomas *et al.* [142].
In general, the spins in a many-particle system precess uniformly in the presence of completely homogeneous fields or in the absence of any. Once we add certain electromagnetic fields and therefore introduce inhomogeneities, the particle spins start to precess differently over time. As we see in the following section, this behaviour is formalized in the

Thomas-Bargmann-Michel-Telegdi (short: T-BMT) equation.
To quantify this effect, we introduce the notion of the polarization vector

$$\mathbf{P} = \frac{1}{N}\sum_{i=1}^{N}\mathbf{s}_i \ , \tag{5.1}$$

which averages over all the spin vectors of an N-particle ensemble. If the angle

$$\alpha = \max_i \left[\arccos\left(\frac{\mathbf{P}_0 \cdot \mathbf{s}_{i,\mathrm{f}}}{|\mathbf{P}_0| \cdot |\mathbf{s}_{i,\mathrm{f}}|}\right)\right] \tag{5.2}$$

between the final spin vector $\mathbf{s}_{i,\mathrm{f}}$ and the initial polarization $\mathbf{P}_0$ stays small, we can argue that the particle ensemble stays polarized. We will describe in the following sections respectively which notion of polarization we will use for our calculations (i.e. which particles count towards the beam). The next sections will introduce three effects/equations that either describe the change of spin over time or the effect of spin onto the particle trajectory. For each of the effects we will discuss how relevant they are to our parameter regime as they occur on disparate time scales.

5.1.1 T-BMT equation

The first equation we need to consider is the aforementioned T-BMT equation. We will follow the derivation by Jackson [119]. The basis for his derivation of the T-BMT equation is the idea by Uhlenbeck and Goudsmit about spin: a particle (originally an electron) has an intrinsic angular momentum named spin $\mathbf{s}$ which is linked to the magnetic moment via

$$\boldsymbol{\mu} = \frac{ge}{2mc}\mathbf{s} \ , \tag{5.3}$$

where g is the *Landé factor*. When the particle is moving through some configuration of electric and magnetic fields $\mathbf{E}, \mathbf{B}$ with a velocity $\mathbf{v}$, the spin should precess like

$$\frac{\mathrm{d}\mathbf{s}}{\mathrm{d}t'} = \frac{ge}{2mc}\mathbf{s} \times \mathbf{B}' \ , \tag{5.4}$$

where variables with an apostrophe are to be understood as being measured in the particle's rest frame. We now want a more general description of spin precession in the relativistic case using four-notation. First, we need to find a spin four-vector $S = (S_0, \mathbf{S})$ that reduces to the common spin-vector $\mathbf{s}$ in the particle's rest frame.
For the zeroth component of the four-vector we have

$$S'^0 = \gamma(S^0 - \boldsymbol{\beta} \cdot \mathbf{S}) \ . \tag{5.5}$$

In the rest frame, this component should vanish, i.e. $U_\alpha S^\alpha = 0$. Thus, $S_0 = \boldsymbol{\beta} \cdot \mathbf{S}$. The Lorentz boost between the two systems gives us

$$\mathbf{S} = \mathbf{s} + \frac{\gamma^2}{\gamma + 1}(\boldsymbol{\beta} \cdot \mathbf{s})\boldsymbol{\beta} \,, \qquad\qquad S_0 = \gamma \boldsymbol{\beta} \cdot \mathbf{s} \,. \tag{5.6}$$

For the spin evolution, Jackson finds that the covariant notation must be of the form

$$\frac{\mathrm{d}S^\alpha}{\mathrm{d}\tau} = K_1 F^{\alpha\beta} + \frac{K_2}{c^2}(S_\lambda F^{\lambda\mu} U_\mu) U^\alpha + \frac{K_3}{c^2}\left(S_\beta \frac{\mathrm{d}U^\beta}{\mathrm{d}\tau}\right) U^\alpha \,, \tag{5.7}$$

where τ denotes proper time, $F^{\alpha\beta}$ is the field tensor and the K_i, $i \in \{1, 2, 3\}$, are constants. To arrive at this equation, he assumed that the equation is linear in spin and in the external fields. For the four-velocity, the velocity itself and the first derivative with respect to proper time may be incorporated; higher orders are excluded. In the resting frame, the equation has to simplify to the known equation. Utilizing the condition $\mathrm{d}_\tau(U_\alpha S^\alpha) = 0$ and allowing for non-electromagnetic forces and field gradients, he finds that $K_1 = K_2$ as well as $K_3 = -1$. The comparison to the original equation yields $K_1 = ge/2mc$. The equation now is of the form

$$\frac{\mathrm{d}S^\alpha}{\mathrm{d}\tau} = \frac{ge}{2mc}\left[F^{\alpha\beta} S_\beta + \frac{1}{c^2} U^\alpha (S_\lambda F^{\lambda\mu} U_\mu)\right] - \frac{1}{c^2} U^\alpha \left(S_\lambda \frac{\mathrm{d}U^\lambda}{\mathrm{d}\tau}\right) \,. \tag{5.8}$$

In the absence of gradient forces akin to the Stern-Gerlach force $\nabla(\boldsymbol{\mu} \cdot \mathbf{B})$ or when the fields are homogeneous, the translatory motion of the particle is described by

$$\frac{\mathrm{d}U^\alpha}{\mathrm{d}\tau} = \frac{e}{mc} F^{\alpha\beta} U_\beta \,. \tag{5.9}$$

This finally yields the *BMT equation* [143]

$$\frac{\mathrm{d}S^\alpha}{\mathrm{d}\tau} = \frac{e}{mc}\left[\frac{g}{2} F^{\alpha\beta} S_\beta + \frac{1}{c^2}\left(\frac{g}{2} - 1\right) U^\alpha (S_\lambda F^{\lambda\mu} U_\mu)\right] \,. \tag{5.10}$$

The name of this equation notably has the "T-" missing, although Thomas' contribution [144] is already implicitly contained. Using more algebra, the equation can be rewritten to the form

$$\frac{\mathrm{d}\mathbf{s}}{\mathrm{d}t} = -\boldsymbol{\Omega} \times \mathbf{s} \tag{5.11}$$

with the precession frequency

$$\boldsymbol{\Omega} = \frac{e}{mc}\left[\Omega_B \mathbf{B} - \Omega_v \left(\frac{\mathbf{v}}{c} \cdot \mathbf{B}\right)\frac{\mathbf{v}}{c} - \Omega_E \frac{\mathbf{v}}{c} \times \mathbf{E}\right] \,. \tag{5.12}$$

The prefactors contain the Lorentz factor γ and the *anomalous magnetic moment* $a = (g-2)/2$ of the particle:

$$\Omega_B = a + \frac{1}{\gamma}\,, \qquad \Omega_v = \frac{a\gamma}{\gamma+1}\,, \qquad \Omega_E = a + \frac{1}{\gamma+1}\,. \tag{5.13}$$

This notation of the T-BMT equation is found in most of the publications concerning spin-polarized particle beams from laser-plasma interaction. The anomalous magnetic moment of the particles is the difference between the Landé factor g expected from the Dirac equation and the results from higher-loop corrections [145]. For example, for the electron, the Dirac equation yields $g = 2$, but more detailed calculation shows that $a_e = (g-2)/2 \approx 10^{-3}$ and not $a_e = 0$ which would otherwise be expected. The value of the proton is significantly larger, $a_p \approx 1.79$.

5.1.2 Stern-Gerlach force

Another effect that could become important for spin-polarized particle beams is the Stern-Gerlach force. It is most prominently known from the famous experiment [146] that showed that different particle spins lead to different particle trajectories if said particles are subject to a magnetic field. This is described by the formula

$$\mathbf{F}_{\mathrm{SG}} = \nabla(\boldsymbol{\mu}\cdot\mathbf{B})\,. \tag{5.14}$$

More generally, a relativistic description of the Stern-Gerlach force is

$$\mathbf{F}_{\mathrm{SG}} = \left(\nabla - \frac{\mathrm{d}}{\mathrm{d}t}\nabla_{\mathbf{v}}\right)(\boldsymbol{\Omega}\cdot\mathbf{s})\,. \tag{5.15}$$

Here, $\boldsymbol{\Omega}$ is the precession frequency that we already have seen in the case of the T-BMT equation. In order to observe a "split" of the particle ensemble with respect to the prevalent fields, a high field strength is necessary. Thomas *et al.* find the following approximations for the separation distances for electrons (Δ_e) and protons (Δ_p) due to the Stern-Gerlach force in their publication [142]:

$$\Delta_e \propto 0.3(2+3a\gamma)\,\lambda_L[\mu\mathrm{m}]^{-1}\,\gamma^{-1}\,, \qquad \Delta_p \propto 0.3\left(\frac{m_e}{m_p}\right)^2\lambda_L[\mu\mathrm{m}]^{-1}\,\gamma^{-1}\,. \tag{5.16}$$

Here, it was assumed that the electromagnetic fields exhibit at least some form of homogeneity, i.e. the field gradients $\partial F = 0$ vanish. In the case of electrons, this distance would be in the μm range, while for protons it would only be in the sub-pm range. Therefore

they conclude that electron beams could by spin-polarized by the Stern-Gerlach force if the acceleration distance would be great enough. For protons, Stern-Gerlach does not seem to deliver any option for beam polarization. Thus, we can generally neglect the Stern-Gerlach force in our case of laser-plasma based acceleration.

5.1.3 Sokolov-Ternov effect

Lastly, radiative effects may also induce changes in spin polarization. This is described by the so-called Sokolov-Ternov effect [27]: when synchrotron radiation is emitted due to electromagnetic fields in a plasma, there are different probabilities for a spin-flip from down to up ($P_\uparrow$) than from up to down ($P_\downarrow$). In turn, over time, polarization of an initially unpolarized beam can be built up. The polarization in dependence of time is described by the equation

$$P(t) = \frac{P_\uparrow - P_\downarrow}{P_\uparrow + P_\downarrow}\left[1 - \exp\left(-\frac{t}{T_{\mathrm{pol}}}\right)\right] , \tag{5.17}$$

where $P_\uparrow, P_\downarrow$ are the aforementioned probabilities and T_{pol} is the characteristic time needed to build up a certain degree of polarization. Again, scaling laws for this effect were derived by Thomas *et al.* in [142]. They found that the characteristic time scales for electrons and protons scale like

$$T_{\mathrm{pol},e} = \frac{10^{-7}\,\mathrm{s}}{T_e\,[\mathrm{GeV}]^2 F\,[\mathrm{TV/m}]^3} , \qquad T_{\mathrm{pol},p} = \frac{10^{14}\,\mathrm{s}}{T_p\,[\mathrm{GeV}]^2 F\,[\mathrm{TV/m}]^3} . \tag{5.18}$$

Here T_e and T_p correspond to the electron and proton kinetic energy, respectively, while F denotes the maximum field strength during acceleration.

In the case of plasma-based accelerators, the polarization time for electrons in the GeV range would be on the order of microseconds, while the duration of laser-particle interaction is typically in the nanosecond range. We can therefore safely disregard contributions by the Sokolov-Ternov effect in our simulations.

Thus, in the subsequent sections, we will only consider spin precession according to the T-BMT equation in our simulations. The spin is incorporated as three (s_x, s_y, s_z) further parameters for the macro-particles and updated during the PIC cycle. Having discussed the relevant effects, we now go over to a brief summary of what means of acceleration and types of targets we could use for spin-polarized particle acceleration.

5.2 Overview of acceleration methods

Depending on what kinds of particles we want to accelerate, we get certain restrictions what means of acceleration are feasible (or even possible) for highly spin-polarized particle beams. In the case of electrons, which we will not discuss more deeply, wakefield acceleration remains a promising method in both the laser-driven and particle beam-driven cases. As shown by Wu *et al.* [29, 147], a pre-polarized HCl target can be used to obtain electron bunches with ca. 80% polarization.

The main problem for wakefield acceleration is the initial phase: during the time of injection, the electrons exhibit only low γ, meaning that the spin precession is comparatively large. In combination with the strong azimuthal magnetic fields B_φ of the bubble this can lead to a strong decrease in average polarization. Afterwards, in the acceleration phase with higher γ, the polarization remains largely unchanged as the prefactors of the precession frequency become smaller. One proposed solution to this is the use of laser pulses consisting of Laguerre-Gaussian modes instead of Gaussian ones, leading to regions with lower B_φ. It has to be noted, however, that the final electron beam becomes ring-shaped, meaning that lower current densities will be achieved.

As already mentioned, the target considered is pre-polarized (a full description of this process for the HCl can be found in [29], for ^{3}He in [28]). This currently allows for the highest degree of beam polarization and is feasible for certain types of mixtures. Recently Nie *et al.* [148] proposed a setup quite similar to the Trojan Horse regime which leads to beams with up to 30% polarization from an initially unpolarized target. Once this approach is further optimized and is applicable for different gas mixtures, it could be the experimentally more feasible method. The requirement of pre-polarization currently also rules out solid-state targets in which the spin cannot be as easily aligned as in gaseous targets [67].

For the acceleration of spin-polarized proton beams different setups could be used. Given very high laser intensities in the future, proton wakefield acceleration like in [64] could become possible. Proof-of-concept numerical studies for that were performed by Hützen *et al.* [149].

Besides this approach, there are several means of proton acceleration that might be usable, i.a. Magnetic Vortex Acceleration (MVA), Radiation Pressure Acceleration (RPA) and others. In the following we will concentrate on the former.

5.3 Magnetic Vortex Acceleration

The effect of laser intensity on spin polarization was already investigated by Jin *et al.* in [150]. There, the normalized laser vector potential was varied in the range $a_0 = 25$-100,

while all other parameters were kept the same. In agreement with the analytical estimates of [142] it was shown in PIC simulations that increasing the laser intensity is accompanied by a decrease in beam polarization: for $a_0 = 25$ the beam polarization was approx. 82%, while for $a_0 = 100$ it dropped to only 56%.

5.3.1 Effects of density down-ramp

In the first studies concerning MVA for spin-polarized particle beams only short gas targets with a steep density-down ramp at the end were used. In the case of electron wakefield acceleration it is well known that the shape of the down-ramp can influence witness beam quality as well as the amount of charge being accelerated. For MVA, down-ramps were investigated by Nakamura *et al.* [72].

We have investigated its effect on spin in a separate publication [139]. Here, a simulation box of size $(100 \times 60 \times 60)\lambda_L$ that is co-moving with the laser pulse is used. The laser pulse of wavelength $\lambda_L = 800$ nm is circularly polarized. Throughout the different simulations, the pulse length of $\tau_0 = 10\lambda_L/c$, the focal spot size of $w_0 = 10\lambda_L$ and the normalized vector potential $a_0 = 25$ are kept the same. The grid size is chosen as $h_x = 0.05\lambda_L$ in propagation direction, and $h_y = h_z = 0.4\lambda_L$ in the transverse direction. The step size is chosen in accordance with the RIP solver, i.e. $\Delta t = h_x/c$.

The target is a pre-polarized ($s_y = 1$) HCl gas with $n_{\mathrm{H}} = n_{\mathrm{Cl}} = 0.0122 n_{\mathrm{cr}}$. This Hydrogen/Chlorine density corresponds to a near-critical electron density. It starts with an up-ramp from vacuum of length $5\lambda_L$, followed by a density plateau with $200\lambda_L$ length. Finally, the down-ramp length at the target's end is varied in the range $(0 - 100)\lambda_L$.

As described in the general theory, the interaction of the laser pulse with this NCD plasma leads to Magnetic Vortex Acceleration. For the case of an absent down-ramp, a well collimated proton beam is created at the target's end (cf. Fig. 5.1). The proton energies are comparable to the original setup by Jin *et al.*, where the influence of the laser intensity was studied. For $a_0 = 25$ and a comparable HCl target (but with $5\lambda_L$ down-ramp) they obtained $\mathcal{E}_p \approx 53$ MeV.

For longer ramps, the electromagnetic fields are able to expand transversely due to the lower density. This behaviour was first described by Nakamura *et al.* [72]. It leads to a difference in beam collimation: now the focusing fields are not able to push all the protons into one well-defined beam. Instead, we observe a "cloud" of protons with lower peak density (see also Fig. 5.2 for the transverse density). The longer the ramp, the more pronounced this behaviour gets: in the case of $75\lambda_L$ and $100\lambda_L$ it is difficult to properly define what protons belong to the final beam.

The reasons for the change in beam structure are two-fold: increasing the ramp lengths in the simulations leads to an effectively longer interaction volume, leading to increased

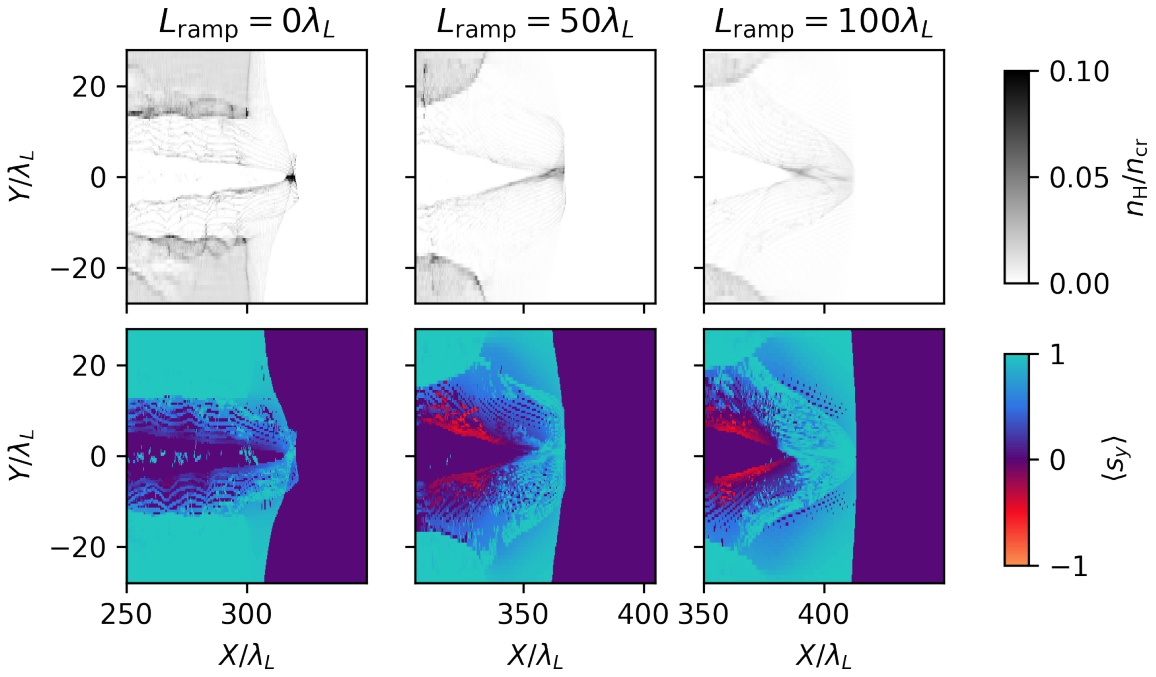

Figure 5.1: Comparison of the beam collimation (top row) and polarization (bottom row) for various ramp lengths. While the collimation quality quickly decreases, polarization in the beam remains high even for longer ramps. *Source: [139].*

dissipation of laser energy. It is difficult to account for this difference in interaction volume as varying the density leads to the laser pulse experiencing different regimes of laser-plasma interaction. Secondly, the transverse expansion of the fields creates a wider channel in the down-ramp region allowing the width of the proton bunch to increase. In publications like [68, 72] the ramp length was always chosen such that beam collimation is as good as possible.

For us, however, the main interest lies within the effect of the down-ramp on spin polarization. From the T-BMT equation we are able to see that the precession frequency should be smaller than for electrons since $|\boldsymbol{\Omega}| \propto m^{-1}$. We have to note, however, that the values for a and γ have changed and therefore the three pre-factors $\Omega_B, \Omega_E, \Omega_v$ have increased in size. For the calculation of the beam's polarization we consider particles close to the central axis. We subdivide the x-direction into several bins and calculate the average $\langle s_y \rangle$ for every bin. As seen from Fig. 5.3, the polarization differs not only over the whole simulation box but also visibly along the beam itself. The reason for this is that particles in the front of the beam experience different electromagnetic fields than the particles in the beam's back. Let us subdivide the beam into a front, middle and back part. Protons in the front have been focused into the bunch for the shortest amount of time, since there the laser pulse has just created the channel and, accordingly, the filament. These protons

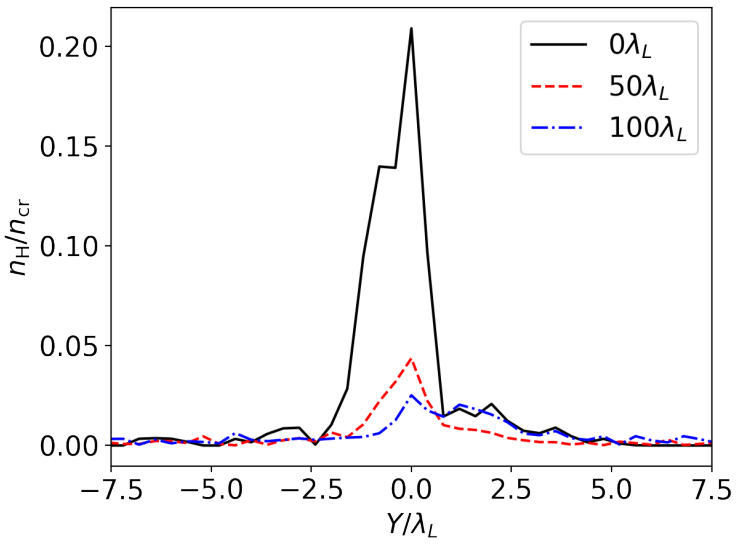

Figure 5.2: Transverse beam profiles for selected ramp lengths in the plane with peak density. Longer ramps allow a widening of the beam structure, there reducing peak density. *Source: [139].* © *IOP Publishing. Reproduced with permission. All rights reserved.*

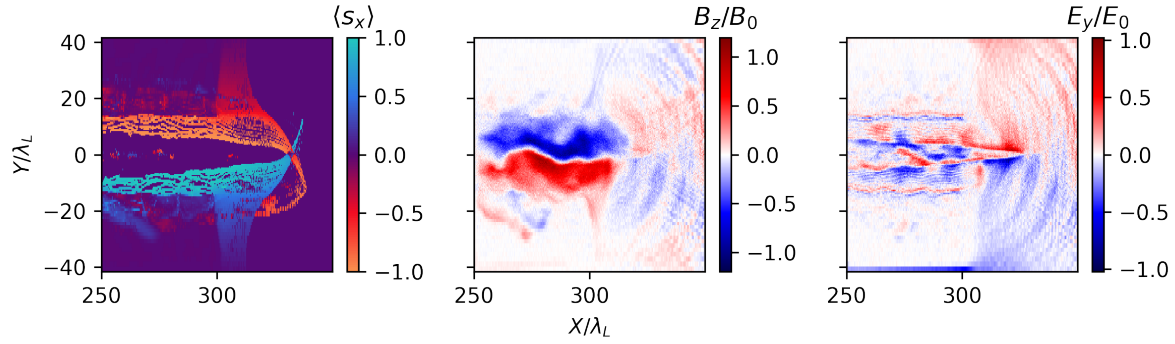

Figure 5.3: Particle spin (a) and field configuration (b), (c) after $300T_0$ in the simulation with $0\lambda_L$ down-ramp. Initially, all protons have $s_x = 0$ and $s_y = 1$. Fields are normalized with $E_0 = B_0 = mc\omega_0/e$. Protons in the accelerated beam maintain high polarization (notice here that $s_x \to 0$), while the surrounding protons differ from the initial polarization direction quite severely. *Source: [139].* © *IOP Publishing. Reproduced with permission. All rights reserved.*

L_{ramp}	0	25	50	75	100
Avg. polarization $\langle s_y \rangle$	0.81	0.83	0.83	*0.83*	*0.63*
n_{peak} $[n_{\text{cr}}]$	0.209	0.126	0.044	*0.027*	*0.025*

Table 5.1: Simulation results for the different ramp lengths. For the longest ramps, $75\lambda_L$ and $100\lambda_L$, the accelerated protons are not well-collimated therefore making the calculation of an average beam polarization complicated (italicized values). *Source: [139].*

experience a comparatively strong field leading to depolarization. Particles in the beam's stern have been propagating through the plasma for a longer time and therefore have been affected more severely by depolarizing fields. This can be seen quite well in Fig. 5.4: there, the slope at the beam back towards $377\lambda_L$ is steeper than at the beam front towards $380\lambda_L$. Protons in the middle part of the beam experience comparatively lower fields and have been part of the beam for a moderate amount of time, thus leading to a peak value in polarization there. This is in agreement with the results from [142], where it was stated that the precession frequency is proportional to the maximum field strength, i.e.

$$|\mathbf{\Omega}| \propto F := \max(|\mathbf{E}|, |\mathbf{B}|) \, . \tag{5.19}$$

The described depolarization in parts of the proton beam already occurs in the absence of any down-ramp. There, however, beam polarization is generally still pretty high. Looking at the various simulations with finite down-ramp lengths, we observe an amplification of the effects described previously, in the case of $100\lambda_L$ leading to the most pronounced drop in polarization (cf. Table 5.1).

Again, the reasons for depolarization are manifold: firstly, the increase in ramp lengths leads to a longer interaction volume. Secondly, longer ramps (i.e. flatter slopes) amplify the differences in fields that the various parts of the proton beam experience. The down-ramp changes the process of compressing the beam when leaving the plasma. This can be viewed like in the case of shock waves, where different components having different velocities being compressed together: depending on the down-ramp more or less protons can easily be compressed longitudinally. The amplitude of the magnetic field also decreased in lower densities. It was shown by Nakamura *et al.* in [72] that

$$B_2 = B_1 \frac{n_1 + n_2}{2n_1} \, , \tag{5.20}$$

where 1 and 2 denote the high- and low-density region of the plasma, respectively. This further shows why the slope in the beam front of the polarization spectrum decreases

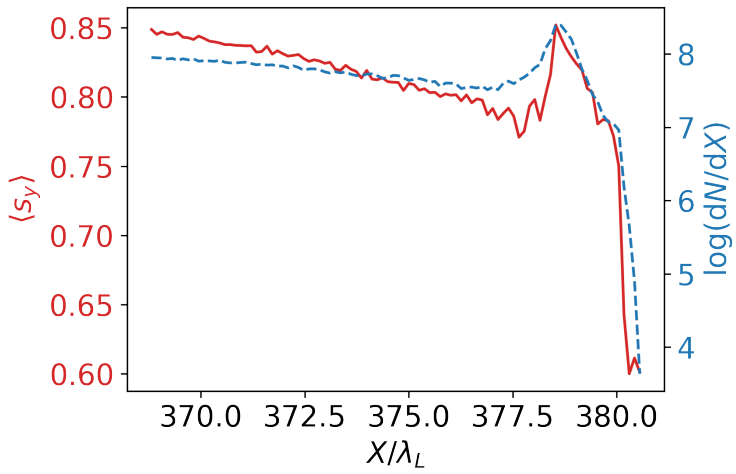

Figure 5.4: Beam polarization (red) and particle number (blue, dashed) in dependence of the longitudinal position in the case of no down-ramp after $300T_0$. *Source: [139].*

slower than in the back.

For most of the considered ramp lengths, the high polarization of around 80% in the absence of any ramp is maintained. Only when using a ramp of $100\lambda_L$ length is the polarization decreasing to approx. 60%. The most visible effect from the simulations, however, still is the decrease in focusing quality. Thus, as mentioned previously, it is difficult to even define the beam for very long ramps.

In order to mitigate these effects it might be possible to change the laser-plasma parameters accordingly. However, for large values of a_0 depolarization becomes very strong even for short down-ramps [150]. Both the polarization decrease due to stronger fields as well as the decrease in long ramps can be explained by the scaling laws derived in [142]. There, a particle beam is described as depolarized once the angle between initial and final polarization direction is in the range of $\pi/2$. This can be expected to occur after the minimum depolarization time

$$T_{D,p} = \frac{\pi}{6.6aF} \,. \tag{5.21}$$

It has to be noted, however, that the equation above assumes that F is constant which is not the case for down-ramps. Since the various parts of the proton beam are "born" at different times. Thus, especially in cases of down-ramps, the experienced fields can be much weaker. In total, it has become clear from the simulations that as-short-as-possible plasma targets are desirable for the acceleration of spin-polarized proton beams, although this will not always be realizable in experiments. For MVA, it has been shown by Sharma

that the ideal length of a plasma plateau is

$$L_{\mathrm{ch}} = a_0 c\tau_0 \frac{n_{\mathrm{cr}}}{n_e} K \ , \tag{5.22}$$

where $K = 13.5$ is a geometric factor for 3D [151]. Thus, depending on the target density, the laser parameters can be chosen to allow for a short plasma slab. For lower a_0, we are also not limited to the here simulated pulse duration τ_0. This also leads to a different time scale over which the MVA structures are built up. In this way, it could be possible to achieve both a well-collimated and highly polarized proton beam.
A further option would be to partly shield the protons from the laser fields by mounting a foil in front of the gas target thereby increasing spin polarization. This setup would be more akin to radiation pressure acceleration [152].
For electrons, it was shown that one could build a mechanical setup in order to filter out unwanted spin contributions [153]. In theory, something similar for protons may be realized.
Finally, for longer gas targets, it could be sensible to employ other elements than proposed here. For example, ^{129}Xe can be nuclear-polarized to a high degree as well [154]. Depending on the used elements, the achievable target density might, however, differ. Therefore, a different regime/process of ion acceleration could occur.

5.3.2 Dual-pulse setup

As we have seen in the last section, it is possible to use MVA in order to accelerate highly spin-polarized proton beams. While the down-ramp was shown to be of rather minor consequence for the final beam polarization at least for shorter targets, it is already clear from studies like [142, 150] that increasing the laser intensity will lead to severe depolarization. Thus for high energy ions, it is of interest to find a more feasible setup.
Already for the wakefield acceleration of electrons certain laser modes have been proven to be beneficial for spin polarization: Wu *et al.* were able to show that using a donut-like Laguerre-Gaussian mode, it is possible to maintain a higher degree of polarization [29]. There, the main advantage is that the weaker azimuthal magnetic field of the mode leads to less spin precession than a conventional Gaussian pulse during the electrons' injection into the bubble. In the acceleration phase after injection the fields are of lesser concern, as the pre-factors of the T-BMT equation tend to zero for high γ.
For ions, the situation is somewhat different: firstly, the values of γ reached during acceleration are quite different from what is possible to achieve with electrons. This will keep the precession frequency $\boldsymbol{\Omega}$ high for a longer period of time. Secondly, the processes and their timescales are very different: for ions (in MVA) the channel needs to be created in

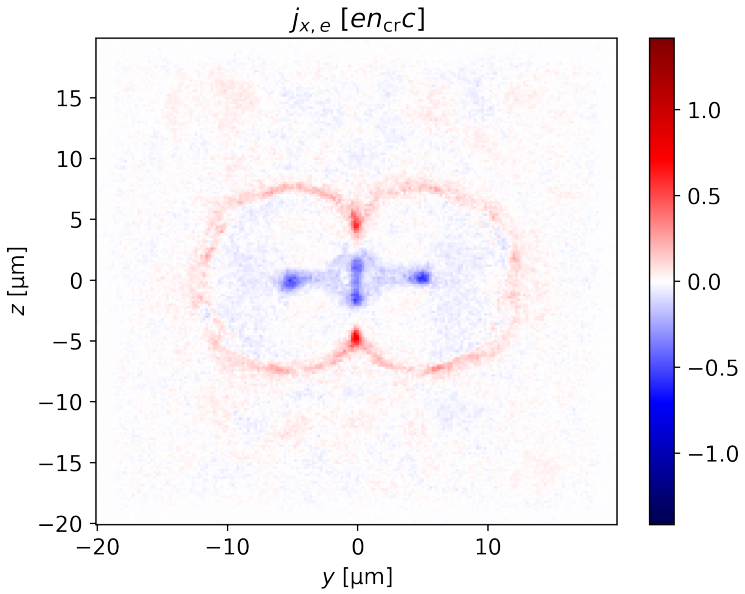

Figure 5.5: Current density in the y-z-plane after $t = 427$ fs. The two plasma channels are shown here by the forward moving currents (blue dots in each center) and corresponding return currents (red circles). Additionally, the central filament (blue region around $(0, 0)^T$) is formed to to the opposing polarization of the two laser pulses. *Source: [140].*

order for the filament to form. Then, the strong azimuthal magnetic field is formed which is detrimental for spin polarization.

Still, it makes sense to look at different laser modes in the context of polarized ions acceleration for a different reason. In a separate publication [140], we have utilized two linearly polarized laser pulses propagating side-by-side. Both laser pulses have anti-parallel phase, meaning that there is a jump of π between the electric fields of the two. This setup can be understood as a simplification of the donut modes of Laguerre-Gaussian pulses to a two-dimensional plane. The two lasers will each create their own plasma channel, i.e. the MVA process occurs twice at the same time. Therefore, two filaments are created and two proton bunches are pushed out of the plasma target at the end. However, more interestingly due to the phase jump, we also will induce a strong longitudinal electric field in the space between the two pulses. This will introduce a third filament in the center, out of which the protons will also be pushed at the end (cf. Fig. 5.5). The advantage of the protons in the third filament is that they are better shielded since they only see part of the laser fields. As we will see, this will increase the polarization of the final proton beam.

The study looked at PIC simulations with different laser intensities. The simulation domain has a size of $120 \times 80 \times 80\lambda_L^3$ and follows the laser pulses (again, $\lambda_L = 0.8$ μm). For the grid, we choose $h_x = 0.05\lambda_L$ (propgation direction), $h_y = h_z = 0.25\lambda_L$. As before,

a_0		$\mathcal{E}_{\text{peak}}$ [MeV]	$\mathcal{E}_{\text{max}}$ [MeV]	Q_{FWHM} [nC]	P_{FWHM}[%]
50	(d)	68.5	107.8	1.07	93
75	(d)	98.3	156.1	0.61	84
100	(d)	124.3	181.8	0.76	77
$\sqrt{2} \cdot 100$	(s)	124.8	186.3	0.61	64

Table 5.2: Results for the dual-pulse setup for various laser intensities. The case of $a_0 = 25$ is excluded here, since no proper peak of the distribution can be defined. The letters (d), (s) denote whether the dual- or single-pulse setup was used. *Source: [140].*

the RIP solver necessitates that $\Delta t = h_x/c$. Further, we increase the transverse grid size by 5% per cell for $|y|, |z| > 20\lambda_L$.

The two laser pulses are linearly polarized and exhibit the mentioned jump of π in the carrier envelope phase. Both of them have the same duration of $\tau = 26.7$ fs and focal spot size $w_0 = 4$ μm. The normalized laser vector potential is varied in range $a_0 = 25 - 100$ for the different simulation runs. Both pulses are separated by $\Delta y = 8$ μm. At the start ($t = 0$ fs), the center of both pulses is placed at $x = -16$ μm.

As before, we utilize the HCl target with density $n_{\text{H}} = n_{\text{Cl}} = 0.0122 n_{\text{cr}}$ and $n_{\text{cr}} = 1.7 \times 10^{21} \text{cm}^{-3}$. The atoms are pre-ionized to H^+ and Cl^{2+}. The target starts with an up-ramp of 4 μm, followed by a plateau at peak density of 200 μm length. The transition to vacuum is marked by a down-ramp of 4 μm. All protons have been pre-polarized, i.e. $s_y = 1$. The process visible in the simulations is as described before: each laser pulse performs its own MVA. Thus, in total, two channels are created. Due to the longitudinal electric field in the region between the pulses stemming from their phase difference, the third filament is formed. From now on, we will refer to it as the "central filament". This central filament is compressed/focused at the end of the target in the same fashion as the filaments in conventional MVA.

We have summarized the results for the different simulation runs after 1.3 ps in Table 5.2. The maximum proton energy obtained of course increases with higher a_0. For $a_0 = 25$ per laser, a maximum energy of $\mathcal{E}_{\text{max}} \approx 45$ MeV is reached. At $a_0 = 100$, the most energetic particles have approx. $\mathcal{E}_{\text{max}} = 182$ MeV. In the following, we will only take into account the protons that have a momentum spread of $\pm 2°$, where $\theta = \arctan(p_y/p_x)$. In all cases but $a_0 = 25$, we see a well-defined peak in the energy spectrum for those protons (cf. Fig. 5.6). We therefore exclude the results for $a_0 = 25$ from further discussion. For $a_0 = 50$, the peak around 68.5 MeV is rather narrow. For larger a_0, the distributions widen to some extent. We further have to note, that for $a_0 = 100$ two peaks around 100 MeV and 150 MeV besides the main peak at 124 MeV show up; this might indicate that the acceleration mechanism actually consists of several processes working together.

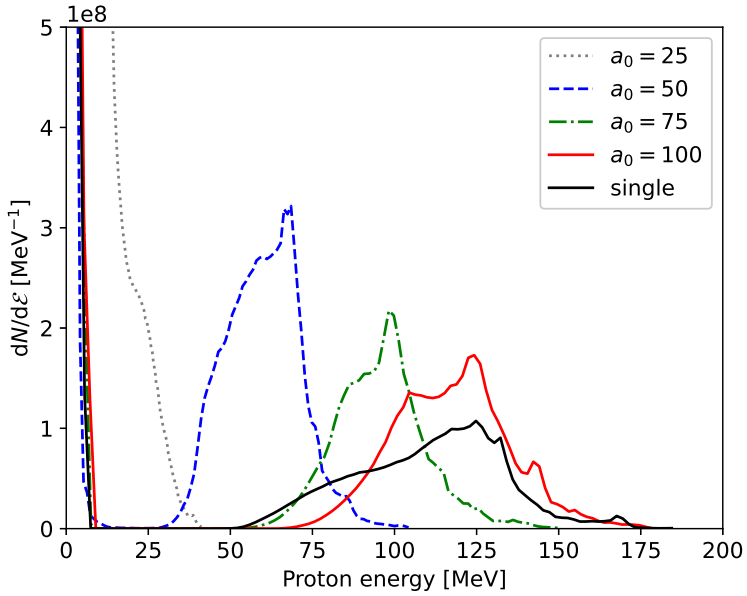

Figure 5.6: Energy spectra for the various simulation runs with the dual-pulse scheme. The line "single" corresponds to the single-pulse comparison with $a_0 = \sqrt{2} \cdot 100$. Note that the plot display the spectra for protons with $|\theta| \leqslant 2°$. *Source: [140].*

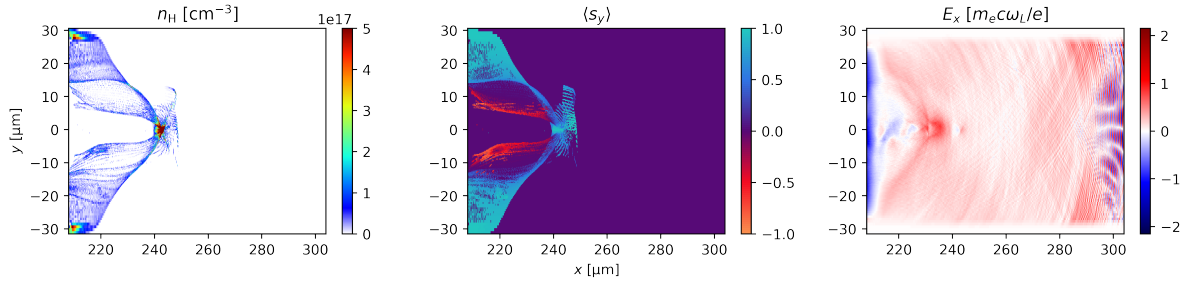

Figure 5.7: Left: Proton density distribution for the dual-pulse setup with $a_0 = 100$ after 1.1 ps. The colorbar is clipped for better visbility; the highest density is seen towards the central axis. Center: Average spin in y-direction. The protons in the accelerated central beam stay better polarized than in the (red) region around it. Right: The accelerating field acting on the protons at the end of the HCl target. *Source: [140].*

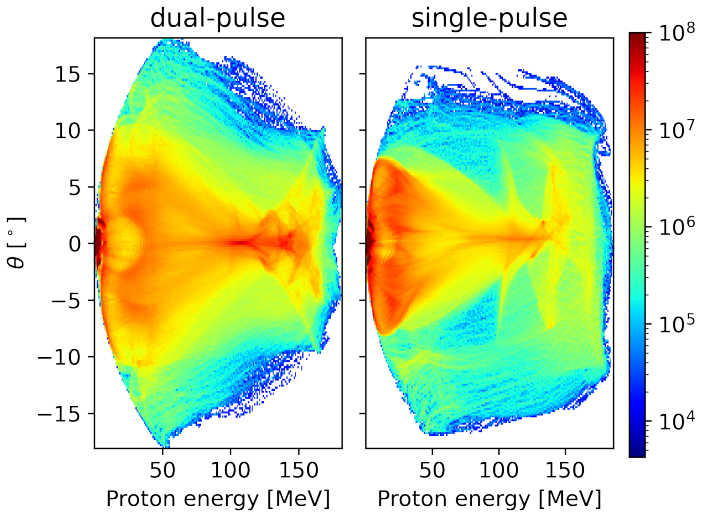

Figure 5.8: Angular distribution plotted against the proton energy. The color corresponds to the number of particles (clipped at 10^8). The angle is defined at $\theta = \arctan(p_y/p_x)$. *Source: [140].*

Even for the large values of a_0, the beams are well collimated. As visible in Fig. 5.7, a well-defined bunch can be seen. Looking closer, we can see that besides the main density peak, there are actually two smaller high-density region stemming from the separate channels. Depending on the choice of laser intensity and plasma density, the accelerated structure can appear more shock-like. The angular distribution can also be seen in Fig. 5.8.

The charge of the final proton beam is in the range of $(0.61 - 1.07)$ nC for all simulations. These numbers refer to the FWHM around the energy peak. No clear trend of the beam charge in dependence of the laser intensity is recognizable which might be attributed to the fact that the density is kept the same throughout all the simulations. Better matching laser and plasma to one another should improve the yield. As known from other publications on ion acceleration, the amount of accelerated protons should generally increase with a_0 for a matched target.

Looking at the beam polarization, we calculate it the following way here: for an N-particle ensemble, the polarization is $P = \sqrt{P_x^2 + P_y^2 + P_z^2}$ where P_j is the average over the spin components, i.e.

$$P_j = \sum_{i=1}^{N} \frac{s_{i,j}}{N} , \quad j \in \{x, y, z\} . \tag{5.23}$$

As visible in Fig. 5.7, the spin precession in the region of the proton bunch is smaller than in the region around it. The polarization spectra for the various intensities is displayed in Fig. 5.9. The general trend, that polarization decreases for rising a_0, also holds here.

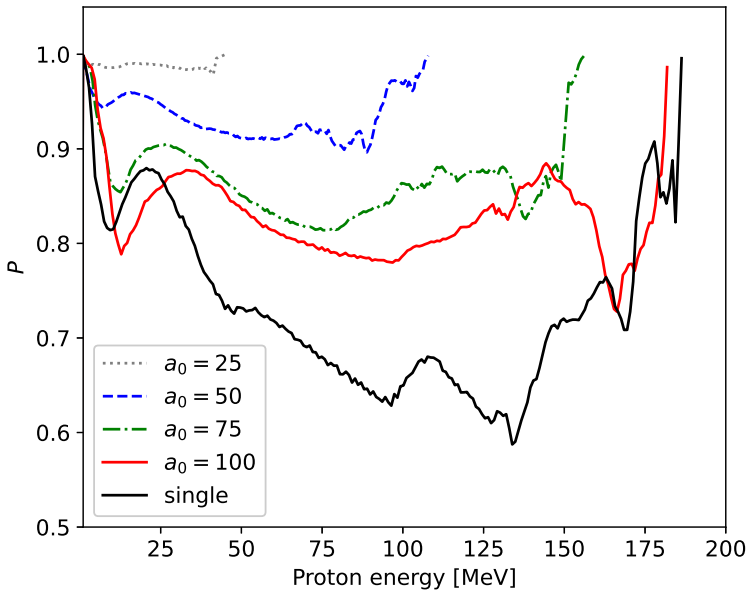

Figure 5.9: Polarization spectra for various laser intensities in the dual-pulse setup; the single-pulse line corresponds to $a_0 = \sqrt{2} \cdot 100$. Note that the apparent polarization increase towards very high proton energies is just of statistical nature and not physical. *Source: [140].*

For $a_0 = 25$, polarization is almost completely negligible. Going to higher intensities the polarization still is around 93% for particles in the FWHM of the $a_0 = 50$ run. For $a_0 = 100$, it decreases to 77%. This is in general agreement with the scaling laws of [142], were it was stated that depolarization time scales with $1/\max(|\mathbf{E}|, |\mathbf{B}|)$. Note that the seeming increase in energy towards very high energies in the polarization spectrum (e.g. for $\mathcal{E} \geqslant 170$ MeV for $a_0 = 100$) must not be interpreted as a physical feature. This actually stems from the statistics: since only a small amount of particles reaches these energies, they all have similar spin direction (in the most extreme case: if only one particle was to be found in that energy bin, it would have perfect polarization, i.e. $P = 100\%$). If we were to consider a dual-pulse setup using two lasers that are in phase (not shown here), we would see lower polarization throughout the whole energy spectrum as the proton beam would consist of particles that would have experienced stronger fields.

The interaction of two laser pulses in a plasma has already been studied in a plethora of publications [44, 155–157] without the consideration of spin polarization. Dong *et al.* solved the equations of two pulses co-propagating in plasma using the slowly varying envelope model [155]. However, they neglected proton motion which becomes important for our laser intensities and our scheme. Additionally, the plasma density was assumed to be low. Nevertheless, it showed that the two channels can attract each other, which can also be seen for higher densities [156, 157]. Other effects visible in our dual-pulse setup

have partly been observed already in other MVA-related studies [68, 72].
In order to have a direct overview over the advantages of the dual-pulse scheme over conventional single-pulse MVA, we have performed further simulations with the same target interacting with only a single laser pulse. This laser pulse still is linearly polarized and has the same duration and focal spot size as the pulses in the simulations before. To accomodate for the difference in energy between the two setups, we use a slightly higher intensity of $\sqrt{2}a_0$.
The simulations show the typical formation process of MVA. Energy-wise the peak value of 124.8 MeV for $a_0 = \sqrt{2}\cdot 100$ is very close to the 124.3 MeV for the dual-pulse setup with $a_0 = 100$ (the maximum proton energy is higher for the single pulse). We do see, however, that the energy spectrum for the single pulse is broader. Further, the angular spread of the dual-pulse scheme is better. This can be attributed to the two laser fields acting from both sides on the central beam, leading to better collimation. This is shown quite clearly in Fig. 5.8. One other interesting aspect visible there is that the single-pulse spectrum is asymmetric around $\theta = \arctan(p_y/p_x) = 0°$ for $\mathcal{E} > 100$ MeV. This kink towards positive θ-values is absent from the dual-pulse scheme indicating that the two laser pulses are able to suppress some instabilities.
For the single-pulse scheme, the beam charge is lower at 0.61 nC as well as the beam polarization at around 64% (for the dual-pulse case it was 0.76 nC and 77%). The lower polarization likely stems from the better shielding from the fields: protons of the central filament only see parts of the strong electromagnetic fields therefore leading to less depolarization. This is not the case for protons in conventional MVA.
The efficiency of the dual-pulse scheme will of course also be influenced by the length of the density down-ramp. As we have seen in the previous section, shorter targets are generally preferable for the final beam quality. In particular, for the two pulses, the transverse expansion of the fields from both channels could lead to them crossing each other, further reducing quality. In total, however, the dual-pulse schemes seems to be generally advantageous due to its better spin polarization and its angular spread.

In the future, more analytical work concerning spin-polarized ion acceleration would be beneficial for further understanding of the processes at hand. Moreover, while the setups presented promise well-polarized beams with high energy, it would be of great interest to simplify the polarization process similar to setups like those of Nie *et al.* [148].

Contributions of the author

For [139] regarding the effects of down-ramps, L.R. conducted the simulations on the basis of discussions with A.H. The examination of the results as well as the writing of the paper were performed by him. In the case of [140] regarding the dual-pulse setup, L.R. performed all the simulations and wrote the manuscript. The same work distribution applies for the proceedings that are based on these results.

Chapter 6

Conclusion

In the present thesis we have investigated several particle acceleration mechanisms that are based on laser-plasma interaction and/or the interaction of energetic particle beams with plasma.

In the first two chapters we have laid the foundation in plasma theory and particle-in-cell simulations that we have used in the later chapters. In particular, we introduced the notion of laser-driven and particle beam-driven plasma wakefield accelerators as well as Magnetic Vortex Acceleration.

In chapter 4 we improved upon analytical models for the description of beam-driven setups. In a first step, we introduced a phenomenological function into the analytical accelerating field that allowed for a better incorporation of its divergence than previous models. This model still exhibited the crux that the initial conditions for the differential equation describing the border of the blowout must be obtained from PIC simulations. A separate model then gave the possibility to describe the structure self-consistently, i.e. only from the parameters of the driving beam.

Further, we proposed a laser-augmented blowout (LAB) scheme for the acceleration of positron rings. The mechanism utilized an electron driver for the ionization of a small plasma column and the excitation of a wake. It was directly followed by a short and weak, but wide laser pulse that ionized a wider column behind the driver. The resulting field structure exhibited equilibrium lines along which the transverse force vanishes, while the accelerating field reaches its maximum for positrons. Placing the positron ring on this line proved to deliver rather stable acceleration over tens of centimeters. The analytical derivation of the equilibrium line was found to be in good agreement with the PIC simulations and the stability of the scheme was discussed extensively.

A further project concerning wakefield acceleration dealt with the inner structure of the witness beam. Following the assumption that the equilibrium of the focusing wakefield and the repelling Liénard-Wiechert potentials should give rise to a periodic structure as

an energetic minimum, we examined the effect of finite emittance onto said structure. It was found that for smaller momentum spread the structure was only marginally changed, but that it could be destroyed for higher emittance.
Lastly for the first part of the thesis, electron acceleration from cryogenic, clustered Hydrogen was investigated in an experimental collaboration. The experimentally observed structure on the image plates could be explained as a consequence of several acceleration mechanisms working together. Moreover, the role of the laser pre-pulse became apparent for such targets: the pre-pulse already ionized part of the clusters, inducing their Coulomb explosion. When the main pulse arrives, it interacts with a more homogeneous plasma in which wakefield acceleration can occur. Further, ponderomotive scattering and direct laser acceleration of electrons are partly responsible for the electron profile observed in experiment. In the context of our presented wakefield research, future work could look into setups feasible for positron acceleration that prove to be even more stable and easier to experimentally realize. Beyond that, the self-consistent theory for the description of beam-driven wakefields [92] should be further developed for the laser-driven case where currently no such theory is available.
In the second part of this thesis, in chapter 5, we investigated the acceleration of proton beams form the interaction of laser pulses with near-critical density plasma in the form of Magnetic Vortex Acceleration. While certain aspects of MVA are already well understood, we focused our research on the spin-polarized proton beams, for which only limited research exists in the context of laser-plasma interaction. In particular, we first simulated targets with different lengths of density down-ramps to understand their influence of beam quality. While in most of the cases the spin polarization was not changed significantly, beam collimation was shown to worsen quite severely due to the transverse expansion of the electromagnetic fields in the ramp. A further publication made use of two laser pulses propagating side-by-side through the same target as in the previous study. The two pulses had a carrier envelope phase difference of π with respect to one another, thus introducing a strong longitudinal electric field in the space between them. This lead to the creation of a central filament of accelerated ions which were better shielded from the laser fields and thereby of higher spin polarization. Further, the presence of the surrounding laser fields also improved beam collimation compared to the conventional single-pulse MVA.
Of great interest in the research of spin-polarized particle beams besides the comparison of theory to the first experimental results would be novel setups where polarization can be more easily obtained. Something similar to the setups by Nie *et al.*, where without a complicated setup polarization can be obtained [148], would be desirable for protons as well. Further, analytical theory on the subject of ion acceleration (especially with spin considered) is currently lacking and should be worked upon in the near future.

Acknowledgments

First and foremost, I would like to thank Prof. Alexander Pukhov for giving me the possibility to perform my PhD studies in his group. Without his advice and support throughout the years this would not have been possible. On a similar note, I would like to thank Johannes Thomas for his support in the onset of my PhD as well as his support throughout my Bachelor's and Master's degree. Prof. Carsten Müller I would like to thank for agreeing to being the second reviewer of this thesis and his general help over the years.
I would further like to thank the DFG and BMBF for funding parts of my projects over the years, as well as the Jülich Supercomputing Center (JSC) which allowed many of the large-scale simulations in the scope of our project (qed20). A big thanks also has to go to our system administrator Eugen Braun who was always able to get everything technical up and running again, even if that would mean staying up until late in the night.
Further, this time of research would not have been nearly as interesting without the many collaborations I have had luck to work on with many wonderful people: Thank you to Prof. Igor Kostyukov and Anton Golovanov from RAS in Nizhny Novgorod for all the analytical insights. Another thanks to Prof. Markus Büscher and Anna Hützen from Forschungszentrum Jülich for introducing me to the field of spin-polarized particle beams and lastly to Bastian Aurand, Esin Aktan, Kerstin Schwind, Prof. Oswald Willi, Mirela Cerchez and Rajendra Prasad from the institute for experimental laser- and plasma physics at our university. Of course, the years in the institute would not have been as pleasant and entertaining without my colleagues: Thanks a lot to Götz Lehmann, Christoph Baumann, Vural Kaymak, Selym Villalba-Chávez, Alexander Voitkiv, Alina Golub, Fiona Grüll, Andreas Jacob, Marko Filipovic and Vadim Khudiakov. Also thanks to Ke Jiang (蒋轲), Xiaofei Shen (沈晓飞) and Zhenjiang Wang (王振江) for the entertaining year(s) although our time as colleagues was sadly restricted due to Covid-19. Further, for her support throughout the years, even before this PhD, I would like to thank my mother, Marion Reichwein, for going out of her way to make this possible. Tashakor, Bibi Mokadessa Abdul Rahman, for always being by my side and supporting me. And finally, for her ever-lasting help and support throughout the years both as a colleague and as my best friend: Tack så mycket, Alexandra Eckey!

Eigenständigkeitserklärung

Ich versichere an Eides Statt, dass die Dissertation von mir selbständig und ohne unzulässige fremde Hilfe unter Beachtung der „Grundsätze zur Sicherung guter wissenschaftlicher Praxis an der Heinrich-Heine-Universität Düsseldorf“ erstellt worden ist. Die Arbeit wurde bislang nicht in deutscher oder einer anderen Sprache veröffentlicht.

Düsseldorf, den 16.11.2022 _____

Lars Reichwein

Bibliography

[1] S. Chatrchyan et al. (CMS Collaboration), *"Observation of a new boson at a mass of 125 GeV with the CMS experiment at the LHC,"* Physics Letters B **716**, 30 (2012).

[2] Large Hadron Collider (LHC), https://home.cern/science/accelerators/large-hadron-collider, accessed 17.07.2022.

[3] Stanford Linear Accelerator Center (SLAC), https://www6.slac.stanford.edu/, accessed 17.07.2022.

[4] V. Malka, S. Fritzler, E. Lefebvre, M.-M. Aleonard, F. Burgy, J.-P. Chambaret, J.-F. Chemin, K. Krushelnick, G. Malka, S. P. D. Mangles, Z. Najmudin, M. Pittman, J.-P. Rousseau, J.-N. Scheurer, B. Walton, and A. E. Dangor, *"Electron acceleration by a wake field forced by an intense ultrashort laser pulse,"* Science **298**, 1596 (2002).

[5] H. H. Braun, S. Döbert, I. Wilson, and W. Wuensch, *"Frequency and temperature dependence of electrical breakdown at 21, 30, and 39 GHz,"* Physical Review Letters **90**, 224801 (2003).

[6] C. E. Clayton, K. A. Marsh, A. Dyson, M. Everett, A. Lal, W. P. Leemans, R. Williams, and C. Joshi, *"Ultrahigh-gradient acceleration of injected electrons by laser-excited relativistic electron plasma waves,"* Physical Review Letters **70**, 37 (1993).

[7] T. Tajima and J. M. Dawson, *"Laser electron accelerator,"* Physical Review Letters **43**, 267 (1979).

[8] M. N. Rosenbluth and C. S. Liu, *"Excitation of plasma waves by two laser beams,"* Physical Review Letters **29**, 701 (1972).

[9] D. Strickland and G. Mourou, *"Compression of amplified chirped optical pulses,"* Optics Communications **56**, 219 (1985).

[10] P. Chen, J. M. Dawson, R. W. Huff, and T. Katsouleas, *"Acceleration of electrons by the interaction of a bunched electron beam with a plasma,"* Physical Review Letters **54**, 693 (1985).

[11] E. Esarey, C. B. Schroeder, and W. P. Leemans, *"Physics of laser-driven plasma-based electron accelerators,"* Reviews of Modern Physics **81**, 1229 (2009).

[12] A. Pukhov and J. Meyer-ter Vehn, *"Laser wake field acceleration: the highly non-linear broken-wave regime,"* Applied Physics B: Lasers and Optics **74**, 355 (2002).

[13] J. Faure, Y. Glinec, A. Pukhov, S. Kiselev, S. Gordienko, E. Lefebvre, J.-P. Rousseau, F. Burgy, and V. Malka, *"A laser–plasma accelerator producing monoenergetic electron beams,"* Nature **431**, 541 (2004).

[14] O. Jansen, T. Tückmantel, and A. Pukhov, *"Scaling electron acceleration in the bubble regime for upcoming lasers,"* The European Physical Journal Special Topics **223**, 1017 (2014).

[15] J. B. Rosenzweig, B. Breizman, T. Katsouleas, and J. J. Su, *"Acceleration and focusing of electrons in two-dimensional nonlinear plasma wake fields,"* Physical Review A **44**, R6189 (1991).

[16] K. V. Lotov, *"Blowout regimes of plasma wakefield acceleration,"* Physical Review E **69**, 046405 (2004).

[17] A. J. Gonsalves, K. Nakamura, J. Daniels, C. Benedetti, C. Pieronek, T. C. H. de Raadt, S. Steinke, J. H. Bin, S. S. Bulanov, J. van Tilborg, C. G. R. Geddes, C. B. Schroeder, C. Tóth, E. Esarey, K. Swanson, L. Fan-Chiang, G. Bagdasarov, N. Bobrova, V. Gasilov, G. Korn, P. Sasorov, and W. P. Leemans, *"Petawatt laser guiding and electron beam acceleration to 8 GeV in a laser-heated capillary discharge waveguide,"* Physical Review Letters **122**, 084801 (2019).

[18] E. Brunetti, R. N. Campbell, J. Lovell, and D. A. Jaroszynski, *"High-charge electron beams from a laser-wakefield accelerator driven by a CO2 laser,"* Scientific Reports **12**, 6703 (2022).

[19] H. Ekerfelt, M. Hansson, I. G. González, X. Davoine, and O. Lundh, *"A tunable electron beam source using trapping of electrons in a density down-ramp in laser wakefield acceleration,"* Scientific Reports **7**, 12229 (2017).

[20] B. Hidding, G. Pretzler, J. B. Rosenzweig, T. Königstein, D. Schiller, and D. L. Bruhwiler, *"Ultracold Electron Bunch Generation via Plasma Photocathode Emission and Acceleration in a Beam-Driven Plasma Blowout,"* Physical Review Letters **108**, 035001 (2012).

[21] H. Daido, M. Nishiuchi, and A. S. Pirozhkov, *"Review of laser-driven ion sources and their applications,"* Reports on Progress in Physics **75**, 056401 (2012).

[22] A. Macchi, M. Borghesi, and M. Passoni, *"Ion acceleration by superintense laser-plasma interaction,"* Reviews of Modern Physics **85**, 751 (2013).

[23] Extreme Light Infrastructure Nuclear Physics (ELI-NP), `https://www.eli-np.ro/`, accessed 17.07.2022.

[24] Exawatt Center for Extreme Light Studies (XCELS), `https://xcels.ipfran.ru/`, accessed 17.07.2022.

[25] C. Glashausser, *"Nuclear physics with polarized beams,"* Annual Review of Nuclear and Particle Science **29**, 33 (1979).

[26] R. M. Kulsrud, H. P. Furth, E. J. Valeo, and M. Goldhaber, *"Fusion reactor plasmas with polarized nuclei,"* Physical Review Letters **49**, 1248 (1982).

[27] I. M. Ternov, *"Synchrotron radiation,"* Physics-Uspekhi **38**, 409 (1995).

[28] P. Fedorets, C. Zheng, R. Engels, I. Engin, H. Feilbach, U. Giesen, H. Glückler, C. Kannis, F. Klehr, M. Lennartz, H. Pfeifer, J. Pfennings, C. M. Schneider, N. Schnitzler, H. Soltner, R. Swaczyna, and M. Büscher, *"A high-density polarized 3he gas–jet target for laser–plasma applications,"* Instruments **6**, 18 (2022).

[29] Y. Wu, L. Ji, X. Geng, Q. Yu, N. Wang, B. Feng, Z. Guo, W. Wang, C. Qin, X. Yan, L. Zhang, J. Thomas, A. Hützen, M. Büscher, T. P. Rakitzis, A. Pukhov, B. Shen, and R. Li, *"Polarized electron-beam acceleration driven by vortex laser pulses,"* New Journal of Physics **21**, 073052 (2019).

[30] M. Roth and M. Schollmeier, *"Ion acceleration—target normal sheath acceleration,"* CERN Yellow Reports , Vol 1 (2016): Proceedings of the 2014 CAS (2016).

[31] V. Kaymak, E. Aktan, M. Cerchez, B. Elkin, M. Papenheim, R. Prasad, A. Pukhov, H.-C. Scheer, A.-M. Schroer, O. Willi, and B. Aurand, *"Boosted acceleration of protons by tailored ultra-thin foil targets,"* Scientific Reports **9**, 18672 (2019).

[32] S. V. Bulanov and T. Z. Esirkepov, *"Comment on collimated multi-MeV ion beams from high-intensity laser interactions with underdense plasma,"* Physical Review Letters **98**, 049503 (2007).

[33] T. Nakamura and K. Mima, *"Magnetic-dipole vortex generation by propagation of ultraintense and ultrashort laser pulses in moderate-density plasmas,"* Physical Review Letters **100**, 205006 (2008).

[34] U. Stroth, *Plasmaphysik* (Springer Berlin Heidelberg, 2018).

[35] O. Svelto, *Principles of Lasers* (Springer Science+Business Media, LLC, 2010).

[36] Z. Najmudin, *"Laser wakefield accelerators,"* CERN Yellow Reports , Vol 1 (2016): Proceedings of the 2014 CAS (2016).

[37] C. Baumann and A. M. Pukhov, *"Generation of attosecond electron packets in the interaction of ultraintense laguerre – gaussian laser beams with plasma,"* Quantum Electronics **47**, 194 (2017).

[38] M. Jirka, M. Vranic, T. Grismayer, and L. O. Silva, *"Scaling laws for direct laser acceleration in a radiation-reaction dominated regime,"* New Journal of Physics **22**, 083058 (2020).

[39] G. Breit and J. A. Wheeler, *"Collision of two light quanta,"* Physical Review **46**, 1087 (1934).

[40] B. Cros, *"Laser-driven plasma wakefield: Propagation effects,"* CERN Yellow Reports , Vol 1 (2016): Proceedings of the 2014 CAS (2016).

[41] S. Palaniyappan, B. M. Hegelich, H.-C. Wu, D. Jung, D. C. Gautier, L. Yin, B. J. Albright, R. P. Johnson, T. Shimada, S. Letzring, D. T. Offermann, J. Ren, C. Huang, R. Hörlein, B. Dromey, J. C. Fernandez, and R. C. Shah, *"Dynamics of relativistic transparency and optical shuttering in expanding overdense plasmas,"* Nature Physics **8**, 763 (2012).

[42] E. Esarey, P. Sprangle, J. Krall, and A. Ting, *"Overview of plasma-based accelerator concepts,"* IEEE Transactions on Plasma Science **24**, 252 (1996).

[43] G. A. Mourou, T. Tajima, and S. V. Bulanov, *"Optics in the relativistic regime,"* Review of Modern Physics **78**, 309 (2006).

[44] A. Pukhov and J. M. ter Vehn, *"Relativistic magnetic self-channeling of light in near-critical plasma: Three-dimensional particle-in-cell simulation,"* Physical Review Letters **76**, 3975 (1996).

[45] S. Rae, *"Ionization-induced defocusing of intense laser pulses in high-pressure gases,"* Optics Communications **97**, 25 (1993).

[46] P. Gibbon, *Short Pulse Laser Interactions with Matter* (Published by Imperial College Press and distributed by World Scientific Publishing Co., 2005).

[47] M. Born, E. Wolf, A. B. Bhatia, P. C. Clemmow, D. Gabor, A. R. Stokes, A. M. Taylor, P. A. Wayman, and W. L. Wilcock, *Principles of Optics* (Cambridge University Press, 1999).

[48] R. Marchand, R. Rankin, C. E. Capjack, and A. Birnboim, *"Diffraction, self-focusing, and the geometrical optics limit in laser produced plasmas,"* Physics of Fluids **30**, 1521 (1987).

[49] A. E. Siegman, *Lasers* (University Science Books, 1990) p. 1283.

[50] W. Kruer, *The Physics of Laser Plasma Interactions* (Westview Press, 2001) p. 206.

[51] B. Quesnel and P. Mora, *"Theory and simulation of the interaction of ultraintense laser pulses with electrons in vacuum,"* Physical Review E **58**, 3719 (1998).

[52] W. Lu, M. Tzoufras, C. Joshi, F. S. Tsung, W. B. Mori, J. Vieira, R. A. Fonseca, and L. O. Silva, *"Generating multi-GeV electron bunches using single stage laser wakefield acceleration in a 3D nonlinear regime,"* Physical Review Special Topics - Accelerators and Beams **10**, 061301 (2007).

[53] J. D. Sadler, C. Arran, H. Li, and K. A. Flippo, *"Overcoming the dephasing limit in multiple-pulse laser wakefield acceleration,"* Physical Review Accelerators and Beams **23**, 021303 (2020).

[54] L. Verra et al. (AWAKE Collaboration), *"Controlled growth of the self-modulation of a relativistic proton bunch in plasma,"* Physical Review Letters **129**, 024802 (2022).

[55] P. Muggli, *"Beam-driven, plasma-based particle accelerators,"* CERN Yellow Reports , Vol 1 (2016): Proceedings of the 2014 CAS (2016).

[56] B. Hidding, A. Beaton, L. Boulton, S. Corde, A. Doepp, F. A. Habib, T. Heinemann, A. Irman, S. Karsch, G. Kirwan, A. Knetsch, G. G. Manahan, A. M. de la Ossa, A. Nutter, P. Scherkl, U. Schramm, and D. Ullmann, in *Springer Proceedings in Physics* (Springer International Publishing, 2019) pp. 95–120.

[57] P. Chen, J. J. Su, J. M. Dawson, K. L. F. Bane, and P. B. Wilson, *"Energy transfer in the plasma wake-field accelerator,"* Physical Review Letters **56**, 1252 (1986).

[58] C. Huang, W. Lu, M. Zhou, C. E. Clayton, C. Joshi, W. B. Mori, P. Muggli, S. Deng, E. Oz, T. Katsouleas, M. J. Hogan, I. Blumenfeld, F. J. Decker, R. Ischebeck, R. H. Iverson, N. A. Kirby, and D. Walz, *"Hosing instability in the blow-out regime for plasma-wakefield acceleration,"* Physical Review Letters **99**, 255001 (2007).

[59] T. Mehrling, R. Fonseca, A. M. de la Ossa, and J. Vieira, *"Mitigation of the hose instability in plasma-wakefield accelerators,"* Physical Review Letters **118**, 174801 (2017).

[60] T. Mehrling, R. Fonseca, A. M. de la Ossa, and J. Vieira, *"Mechanisms for the mitigation of the hose instability in plasma-wakefield accelerators,"* Physical Review Accelerators and Beams **22**, 031302 (2019).

[61] I. Kostyukov, A. Pukhov, and S. Kiselev, *"Phenomenological theory of laser-plasma interaction in "bubble" regime,"* Physics of Plasmas **11**, 5256 (2004).

[62] A. G. R. Thomas, *"Scalings for radiation from plasma bubbles,"* Physics of Plasmas **17**, 056708 (2010).

[63] M. Chen, E. Esarey, C. B. Schroeder, C. G. R. Geddes, and W. P. Leemans, *"Theory of ionization-induced trapping in laser-plasma accelerators,"* Physics of Plasmas **19**, 033101 (2012).

[64] B. Shen, Y. Li, M. Y. Yu, and J. Cary, *"Bubble regime for ion acceleration in a laser-driven plasma,"* Physical Review E **76**, 055402 (2007).

[65] L. Yin, B. J. Albright, K. J. Bowers, D. Jung, J. C. Fernández, and B. M. Hegelich, *"Three-dimensional dynamics of breakout afterburner ion acceleration using high-contrast short-pulse laser and nanoscale targets,"* Physical Review Letters **107**, 045003 (2011).

[66] A. Macchi, *"Theory of light sail acceleration by intense lasers: an overview,"* High Power Laser Science and Engineering **2**, e10 (2014).

[67] M. Büscher, A. Hützen, L. Ji, and A. Lehrach, *"Generation of polarized particle beams at relativistic laser intensities,"* High Power Laser Science and Engineering **8**, e36 (2020).

[68] J. Park, S. S. Bulanov, J. Bin, Q. Ji, S. Steinke, J.-L. Vay, C. G. R. Geddes, C. B. Schroeder, W. P. Leemans, T. Schenkel, and E. Esarey, *"Ion acceleration in laser generated megatesla magnetic vortex,"* Physics of Plasmas **26**, 103108 (2019).

[69] G.-Z. Sun, E. Ott, Y. C. Lee, and P. Guzdar, *"Self-focusing of short intense pulses in plasmas,"* Physics of Fluids **30**, 526 (1987).

[70] S. Bulanov, E. Esarey, C. Schroeder, S. Bulanov, T. Z. Esirkepov, M. Kando, F. Pegoraro, and W. Leemans, *"Enhancement of maximum attainable ion energy in the radiation pressure acceleration regime using a guiding structure,"* Physical Review Letters **114**, 105003 (2015).

[71] S. S. Bulanov, V. Y. Bychenkov, V. Chvykov, G. Kalinchenko, D. W. Litzenberg, T. Matsuoka, A. G. R. Thomas, L. Willingale, V. Yanovsky, K. Krushelnick, and A. Maksimchuk, *"Generation of GeV protons from 1 PW laser interaction with near critical density targets,"* Physics of Plasmas **17**, 043105 (2010).

[72] T. Nakamura, S. V. Bulanov, T. Z. Esirkepov, and M. Kando, *"High-energy ions from near-critical density plasmas via magnetic vortex acceleration,"* Physical Review Letters **105**, 135002 (2010).

[73] A. Pukhov, *"Three-dimensional electromagnetic relativistic particle-in-cell code VLPL (virtual laser plasma lab),"* Journal of Plasma Physics **61**, 425 (1999).

[74] A. Pukhov, *"Particle-in-cell codes for plasma-based particle acceleration,"* CERN Yellow Reports , Vol 1 (2016): Proceedings of the 2014 CAS (2016).

[75] T. D. Arber, K. Bennett, C. S. Brady, A. Lawrence-Douglas, M. G. Ramsay, N. J. Sircombe, P. Gillies, R. G. Evans, H. Schmitz, A. R. Bell, and C. P. Ridgers, *"Contemporary particle-in-cell approach to laser-plasma modelling,"* Plasma Physics and Controlled Fusion **57**, 113001 (2015).

[76] R. Courant, K. Friedrichs, and H. Lewy, *"Über die partiellen Differenzengleichungen der mathematischen Physik,"* Mathematische Annalen **100**, 32 (1928).

[77] A. Pukhov, *"X-dispersionless maxwell solver for plasma-based particle acceleration,"* Journal of Computational Physics **418**, 109622 (2020).

[78] M. Filipovic, C. Baumann, and A. Pukhov, *"Suppression of errors in simulated ultrarelativistic bunch propagation using the x-dispersionless maxwell solver,"* Physical Review Accelerators and Beams **25**, 054405 (2022).

[79] C. Birdsall and A. Langdon, *Plasma Physics via Computer Simulation* (CRC Press, 2018).

[80] R. Cohen, A. Friedman, D. Grote, and J.-L. Vay, *"An implicit "drift-lorentz" mover for plasma and beam simulations,"* Nuclear Instruments and Methods in Physics

Research Section A: Accelerators, Spectrometers, Detectors and Associated Equipment **606**, 53 (2009).

[81] F. Li, V. K. Decyk, K. G. Miller, A. Tableman, F. S. Tsung, M. Vranic, R. A. Fonseca, and W. B. Mori, *"Accurately simulating nine-dimensional phase space of relativistic particles in strong fields,"* Journal of Computational Physics **438**, 110367 (2021).

[82] L. Reichwein, A. Golovanov, I. Y. Kostyukov, and A. Pukhov, *"Positron acceleration via laser-augmented blowouts in two-column plasma structures,"* arXiv:2110.05226 [physics] (2022).

[83] P. Mora and J. Thomas M. Antonsen, *"Kinetic modeling of intense, short laser pulses propagating in tenuous plasmas,"* Physics of Plasmas **4**, 217 (1997).

[84] I. Kostyukov, E. Nerush, A. Pukhov, and V. Seredov, *"A multidimensional theory for electron trapping by a plasma wake generated in the bubble regime,"* New Journal of Physics **12**, 045009 (2010).

[85] W. Lu, C. Huang, M. Zhou, M. Tzoufras, F. S. Tsung, W. B. Mori, and T. Katsouleas, *"A nonlinear theory for multidimensional relativistic plasma wave wakefields,"* Physics of Plasmas **13**, 056709 (2006).

[86] A. A. Golovanov, I. Y. Kostyukov, A. M. Pukhov, and J. Thomas, *"Generalised model of a sheath of a plasma bubble excited by a short laser pulse or by a relativistic electron bunch in transversely inhomogeneous plasma,"* Quantum Electronics **46**, 295 (2016).

[87] A. A. Golovanov, I. Y. Kostyukov, J. Thomas, and A. Pukhov, *"Analytic model for electromagnetic fields in the bubble regime of plasma wakefield in non-uniform plasmas,"* Physics of Plasmas **24**, 103104 (2017).

[88] J. Thomas, A. A. Golovanov, I. Y. Kostyukov, and A. M. Pukhov, *"Delta-layer model for the boundary of a bubble excited by an electron bunch or laser pulse in a plasma channel,"* Quantum Electronics **47**, 228 (2017).

[89] L. Reichwein, J. Thomas, A. Golovanov, I. Kostyukov, and A. Pukhov, *"Fixing E-field divergence in strongly non-linear wakefields in homogeneous plasma,"* Plasma Physics and Controlled Fusion **62**, 115017 (2020).

[90] B. Hidding, J. B. Rosenzweig, Y. Xi, B. O'Shea, G. Andonian, D. Schiller, S. Barber, O. Williams, G. Pretzler, T. Königstein, F. Kleeschulte, M. J. Hogan, M. Litos,

S. Corde, W. W. White, P. Muggli, D. L. Bruhwiler, and K. Lotov, *"Beyond injection: Trojan horse underdense photocathode plasma wakefield acceleration,"* in *AIP Conference Proceedings* (AIP, 2013).

[91] J. Thomas, I. Y. Kostyukov, J. Pronold, A. Golovanov, and A. Pukhov, *"Non-linear theory of a cavitated plasma wake in a plasma channel for special applications and control,"* Physics of Plasmas **23**, 053108 (2016).

[92] A. A. Golovanov, I. Y. Kostyukov, L. Reichwein, J. Thomas, and A. Pukhov, *"Excitation of strongly nonlinear plasma wakefield by electron bunches,"* Plasma Physics and Controlled Fusion **63**, 085004 (2021).

[93] N. Jain, T. Antonsen, and J. Palastro, *"Positron acceleration by plasma wakefields driven by a hollow electron beam,"* Physical Review Letters **115**, 195001 (2015).

[94] S. Corde, E. Adli, J. M. Allen, W. An, C. I. Clarke, C. E. Clayton, J. P. Delahaye, J. Frederico, S. Gessner, S. Z. Green, M. J. Hogan, C. Joshi, N. Lipkowitz, M. Litos, W. Lu, K. A. Marsh, W. B. Mori, M. Schmeltz, N. Vafaei-Najafabadi, D. Walz, V. Yakimenko, and G. Yocky, *"Multi-gigaelectronvolt acceleration of positrons in a self-loaded plasma wakefield,"* Nature **524**, 442 (2015).

[95] S. Gessner, E. Adli, J. M. Allen, W. An, C. I. Clarke, C. E. Clayton, S. Corde, J. P. Delahaye, J. Frederico, S. Z. Green, C. Hast, M. J. Hogan, C. Joshi, C. A. Lindstrøm, N. Lipkowitz, M. Litos, W. Lu, K. A. Marsh, W. B. Mori, B. O'Shea, N. Vafaei-Najafabadi, D. Walz, V. Yakimenko, and G. Yocky, *"Demonstration of a positron beam-driven hollow channel plasma wakefield accelerator,"* Nature Communications **7**, 11785 (2016).

[96] T. Silva, L. Amorim, M. Downer, M. Hogan, V. Yakimenko, R. Zgadzaj, and J. Vieira, *"Stable positron acceleration in thin, warm, hollow plasma channels,"* Physical Review Letters **127**, 104801 (2021).

[97] S. Diederichs, T. J. Mehrling, C. Benedetti, C. B. Schroeder, A. Knetsch, E. Esarey, and J. Osterhoff, *"Positron transport and acceleration in beam-driven plasma wakefield accelerators using plasma columns,"* Physical Review Accelerators and Beams **22**, 081301 (2019).

[98] S. Diederichs, C. Benedetti, E. Esarey, J. Osterhoff, and C. Schroeder, *"High-quality positron acceleration in beam-driven plasma accelerators,"* Physical Review Accelerators and Beams **23**, 121301 (2020).

[99] S. Diederichs, C. Benedetti, E. Esarey, M. Thévenet, J. Osterhoff, and C. B. Schroeder, *"Stable electron beam propagation in a plasma column,"* Physics of Plasmas **29**, 043101 (2022).

[100] S. Diederichs, C. Benedetti, M. Thévenet, E. Esarey, J. Osterhoff, and C. B. Schroeder, *"Self-stabilizing positron acceleration in a plasma column,"* arXiv:2206.11967 [physics] (2022).

[101] L. Reichwein, A. Pukhov, A. Golovanov, and I. Y. Kostyukov, *"Positron acceleration via laser-augmented blowouts in two-column plasma structures,"* Physical Review E **105**, 055207 (2022).

[102] D. E. Rivas, A. Borot, D. E. Cardenas, G. Marcus, X. Gu, D. Herrmann, J. Xu, J. Tan, D. Kormin, G. Ma, W. Dallari, G. D. Tsakiris, I. B. Földes, S. w. Chou, M. Weidman, B. Bergues, T. Wittmann, H. Schröder, P. Tzallas, D. Charalambidis, O. Razskazovskaya, V. Pervak, F. Krausz, and L. Veisz, *"Next generation driver for attosecond and laser-plasma physics,"* Scientific Reports **7**, 5224 (2017).

[103] N. E. Andreev, M. E. Veisman, S. P. Goreslavskii, and M. V. Chegotov, *"Residual electron momentum and energy in a gas ionized by a short high-power laser pulse,"* Plasma Physics Reports **27**, 278 (2001).

[104] F. Massimo, A. Beck, J. Derouillat, I. Zemzemi, and A. Specka, *"Numerical modeling of laser tunneling ionization in particle-in-cell codes with a laser envelope model,"* Physical Review E **102**, 033204 (2020).

[105] G.-B. Zhang, M. Chen, C. B. Schroeder, J. Luo, M. Zeng, F.-Y. Li, L.-L. Yu, S.-M. Weng, Y.-Y. Ma, T.-P. Yu, Z.-M. Sheng, and E. Esarey, *"Acceleration and evolution of a hollow electron beam in wakefields driven by a laguerre-gaussian laser pulse,"* Physics of Plasmas **23**, 033114 (2016).

[106] C. Baumann and A. Pukhov, *"Electron dynamics in twisted light modes of relativistic intensity,"* Physics of Plasmas **25**, 083114 (2018).

[107] W. K. H. Panofsky and W. A. Wenzel, *"Some considerations concerning the transverse deflection of charged particles in radio-frequency fields,"* Review of Scientific Instruments **27**, 967 (1956).

[108] S. Z. Li, E. Adli, R. J. England, J. Frederico, S. J. Gessner, M. J. Hogan, M. D. Litos, D. R. Walz, P. Muggli, W. An, C. E. Clayton, C. Joshi, W. Lu, K. A. Marsh, W. Mori, and N. Vafaei, *"Head erosion with emittance growth in PWFA,"* in *AIP Conference Proceedings* (AIP, 2013).

[109] W. An, M. Zhou, N. Vafaei-Najafabadi, K. A. Marsh, C. E. Clayton, C. Joshi, W. B. Mori, W. Lu, E. Adli, S. Corde, M. Litos, S. Li, S. Gessner, J. Frederico, M. J. Hogan, D. Walz, J. England, J. P. Delahaye, and P. Muggli, *"Strategies for mitigating the ionization-induced beam head erosion problem in an electron-beam-driven plasma wakefield accelerator,"* Physical Review Special Topics - Accelerators and Beams **16**, 101301 (2013).

[110] E. Wigner, *"On the interaction of electrons in metals,"* Physical Review **46**, 1002 (1934).

[111] J. Schiffer, *"Crystalline beams,"* in *Proceedings Particle Accelerator Conference* (IEEE, 1995).

[112] J. Thomas, M. M. Günther, and A. Pukhov, *"Beam load structures in a basic relativistic interaction model,"* Physics of Plasmas **24**, 013101 (2017).

[113] L. Reichwein, J. Thomas, and A. Pukhov, *"Two-dimensional structures of electron bunches in relativistic plasma cavities,"* Physical Review E **98**, 013201 (2018).

[114] L. D. Landau and E. M. Lifshitz, *The classical theory of fields*, 4th ed. (Elsevier Butterworth Heinemann, Amsterdam Heidelberg, 1975).

[115] J. H. Conway and N. J. A. Sloane, *Sphere Packings, Lattices and Groups* (Springer New York, 1999).

[116] A. Radzvilavičius and E. Anisimovas, *"Topological defect motifs in two-dimensional coulomb clusters,"* Journal of Physics: Condensed Matter **23**, 385301 (2011).

[117] L. Reichwein, *Struktur von Coulomb-Clustern im Bubble-Regime*, BestMasters (Springer Spektrum, Wiesbaden [Heidelberg], 2020).

[118] L. Reichwein, J. Thomas, and A. Pukhov, *"The filamented electron bunch of the bubble regime,"* Laser and Particle Beams **38**, 121 (2020).

[119] J. D. Jackson, *Klassische Elektrodynamik* (De Gruyter, 2013).

[120] M. Riedmiller and H. Braun, *"A direct adaptive method for faster backpropagation learning: the RPROP algorithm,"* in *IEEE International Conference on Neural Networks* (IEEE, 1993).

[121] N. Metropolis, A. W. Rosenbluth, M. N. Rosenbluth, A. H. Teller, and E. Teller, *"Equation of state calculations by fast computing machines,"* The Journal of Chemical Physics **21**, 1087 (1953).

[122] I. Wegener, *"Simulated annealing beats metropolis in combinatorial optimization,"* in *Automata, Languages and Programming* (Springer Berlin Heidelberg, 2005) pp. 589–601.

[123] L. Reichwein, J. Thomas, and A. Pukhov, *"Finite-emittance Wigner crystals in the bubble regime,"* Laser and Particle Beams **38**, 176 (2020).

[124] B. Aurand, L. Reichwein, K. M. Schwind, E. Aktan, M. Cerchez, V. Kaymak, L. Lessmann, R. Prasad, J. Thomas, T. Toncian, A. Khoukaz, A. Pukhov, and O. Willi, *"Spatial profile of accelerated electrons from ponderomotive scattering in hydrogen cluster targets,"* New Journal of Physics **24**, 033006 (2022).

[125] B. Aurand, S. Grieser, T. Toncian, E. Aktan, M. Cerchez, L. Lessmann, R. Prasad, A. Khoukaz, and O. Willi, *"A multihertz, kiloelectronvolt pulsed proton source from a laser irradiated continuous hydrogen cluster target,"* Physics of Plasmas **26**, 073102 (2019).

[126] S. Grieser, B. Aurand, E. Aktan, D. Bonaventura, M. Büscher, M. Cerchez, I. Engin, L. Leßmann, C. Mannweiler, R. Prasad, O. Willi, and A. Khoukaz, *"Nm-sized cryogenic hydrogen clusters for a laser-driven proton source,"* Review of Scientific Instruments **90**, 043301 (2019).

[127] B. Aurand, K. Schwind, T. Toncian, E. Aktan, M. Cerchez, L. Lessmann, C. Mannweiler, R. Prasad, A. Khoukaz, and O. Willi, *"Study of the parameter dependence of laser-accelerated protons from a hydrogen cluster source,"* New Journal of Physics **22**, 033025 (2020).

[128] M. Cerchez, R. Prasad, B. Aurand, A. L. Giesecke, S. Spickermann, S. Brauckmann, E. Aktan, M. Swantusch, M. Toncian, T. Toncian, and O. Willi, *"ARCTURUS laser: a versatile high-contrast, high-power multi-beam laser system,"* High Power Laser Science and Engineering **7**, e37 (2019).

[129] F. V. Hartemann, S. N. Fochs, G. P. L. Sage, N. C. Luhmann, J. G. Woodworth, M. D. Perry, Y. J. Chen, and A. K. Kerman, *"Nonlinear ponderomotive scattering of relativistic electrons by an intense laser field at focus,"* Physical Review E **51**, 4833 (1995).

[130] P. Monot, T. Auguste, L. A. Lompré, G. Mainfray, and C. Manus, *"Energy measurements of electrons submitted to an ultrastrong laser field,"* Physical Review Letters **70**, 1232 (1993).

[131] C. I. Moore, J. P. Knauer, and D. D. Meyerhofer, *"Observation of the transition from thomson to compton scattering in multiphoton interactions with low-energy electrons,"* Physical Review Letters **74**, 2439 (1995).

[132] G. Malka, E. Lefebvre, and J. L. Miquel, *"Experimental observation of electrons accelerated in vacuum to relativistic energies by a high-intensity laser,"* Physical Review Letters **78**, 3314 (1997).

[133] T. Auguste, P. D'Oliveira, S. Hulin, P. Monot, J. Abdallah, A. Y. Faenov, I. Y. Skobelev, A. I. Magunov, and T. A. Pikuz, *"The role of the prepulse in cluster heating by a high-power femtosecond laser pulse,"* Journal of Experimental and Theoretical Physics Letters **72**, 38 (2000).

[134] M. Mayr, L. Ceurvorst, M. Kasim, J. Sadler, B. Spiers, K. Glize, A. Savin, N. Bourgeois, F. Keeble, A. Ross, D. Symes, R. Aboushelbaya, R. Fonseca, J. Holloway, N. Ratan, R. Trines, R. Wang, R. Bingham, L. Silva, P. Burrows, M. Wing, P. Rajeev, and P. Norreys, *"Wakefields in a cluster plasma,"* Physical Review Accelerators and Beams **22**, 113501 (2019).

[135] M. Mayr, B. Spiers, R. Aboushelbaya, R. Paddock, J. Sadler, C. Sillett, R. Wang, K. Krushelnick, and P. Norreys, *"Nonlinear wakefields and electron injection in cluster plasma,"* Physical Review Accelerators and Beams **23**, 093501 (2020).

[136] E. Oz, S. Deng, T. Katsouleas, P. Muggli, C. D. Barnes, I. Blumenfeld, F. J. Decker, P. Emma, M. J. Hogan, R. Ischebeck, R. H. Iverson, N. Kirby, P. Krejcik, C. O'Connell, R. H. Siemann, D. Walz, D. Auerbach, C. E. Clayton, C. Huang, D. K. Johnson, C. Joshi, W. Lu, K. A. Marsh, W. B. Mori, and M. Zhou, *"Ionization-induced electron trapping in ultrarelativistic plasma wakes,"* Physical Review Letters **98**, 084801 (2007).

[137] M. Burkardt, C. A. Miller, and W.-D. Nowak, *"Spin-polarized high-energy scattering of charged leptons on nucleons,"* Reports on Progress in Physics **73**, 016201 (2009).

[138] U. Camerini, D. Cline, J. Learned, A. K. Mann, and L. K. Resvanis, *"Measurement of the radiative electron polarization in a 2.4-GeV storage ring,"* Physical Review D **12**, 1855 (1975).

[139] L. Reichwein, A. Hützen, M. Büscher, and A. Pukhov, *"On the robustness of spin polarization for magnetic vortex accelerated proton bunches in density down-ramps,"* Plasma Physics and Controlled Fusion **63**, 085011 (2021).

[140] L. Reichwein, M. Büscher, and A. Pukhov, *"Acceleration of spin-polarized proton beams via two parallel laser pulses,"* arXiv:2201.11534 [physics] (2022).

[141] S. R. Mane, Y. M. Shatunov, and K. Yokoya, *"Spin-polarized charged particle beams in high-energy accelerators,"* Reports on Progress in Physics **68**, 1997 (2005).

[142] J. Thomas, A. Hützen, A. Lehrach, A. Pukhov, L. Ji, Y. Wu, X. Geng, and M. Büscher, *"Scaling laws for the depolarization time of relativistic particle beams in strong fields,"* Physical Review Accelerators and Beams **23**, 064401 (2020).

[143] V. Bargmann, L. Michel, and V. L. Telegdi, *"Precession of the polarization of particles moving in a homogeneous electromagnetic field,"* Physical Review Letters **2**, 435 (1959).

[144] L. H. Thomas, *"The motion of the spinning electron,"* Nature **117**, 514 (1926).

[145] F. Schwabl, *Quantenmechanik für Fortgeschrittene (QM II)* (Springer Berlin Heidelberg, 2008).

[146] W. Gerlach and O. Stern, *"Der experimentelle Nachweis der Richtungsquantelung im Magnetfeld,"* Zeitschrift für Physik **9**, 349 (1922).

[147] Y. Wu, L. Ji, X. Geng, Q. Yu, N. Wang, B. Feng, Z. Guo, W. Wang, C. Qin, X. Yan, L. Zhang, J. Thomas, A. Hützen, A. Pukhov, M. Büscher, B. Shen, and R. Li, *"Polarized electron acceleration in beam-driven plasma wakefield based on density down-ramp injection,"* Physical Review E **100**, 043202 (2019).

[148] Z. Nie, F. Li, F. Morales, S. Patchkovskii, O. Smirnova, W. An, N. Nambu, D. Matteo, K. A. Marsh, F. Tsung, W. B. Mori, and C. Joshi, *"In-situ generation of high-energy spin-polarized electrons in a beam-driven plasma wakefield accelerator,"* Physical Review Letters **126**, 054801 (2021).

[149] A. Hützen, J. Thomas, A. Lehrach, T. Rakitzis, A. Pukhov, L. Ji, Y. Wu, R. Engels, and M. Büscher, *"Simulation of polarized beams from laser-plasma accelerators,"* Journal of Physics: Conference Series **1596**, 012013 (2020).

[150] L. Jin, M. Wen, X. Zhang, A. Hützen, J. Thomas, M. Büscher, and B. Shen, *"Spin-polarized proton beam generation from gas-jet targets by intense laser pulses,"* Physical Review E **102**, 011201 (2020).

[151] A. Sharma, *"High energy electron and proton acceleration by circularly polarized laser pulse from near critical density hydrogen gas target,"* Scientific Reports **8**, 2191 (2018).

[152] A. Macchi, C. Livi, and A. Sgattoni, *"Radiation pressure acceleration: perspectives and limits,"* Journal of Instrumentation **12**, C04016 (2017).

[153] Y. Wu, L. Ji, X. Geng, J. Thomas, M. Büscher, A. Pukhov, A. Hützen, L. Zhang, B. Shen, and R. Li, *"Spin filter for polarized electron acceleration in plasma wakefields,"* Physical Review Applied **13**, 044064 (2020).

[154] D. J. Kennedy, S. J. Seltzer, R. Jiménez-Martínez, H. L. Ring, N. S. Malecek, S. Knappe, E. A. Donley, J. Kitching, V. S. Bajaj, and A. Pines, *"An optimized microfabricated platform for the optical generation and detection of hyperpolarized 129Xe,"* Scientific Reports **7**, 43994 (2017).

[155] Q.-L. Dong, Z.-M. Sheng, and J. Zhang, *"Self-focusing and merging of two copropagating laser beams in underdense plasma,"* Physical Review E **66**, 027402 (2002).

[156] T. W. Huang, C. T. Zhou, R. X. Bai, L. B. Ju, K. Jiang, T. Y. Long, H. Zhang, S. Z. Wu, and S. C. Ruan, *"Electron acceleration induced by interaction of two relativistic laser pulses in underdense plasmas,"* Physical Review E **98**, 053207 (2018).

[157] R. X. Bai, C. T. Zhou, T. W. Huang, L. B. Ju, S. Z. Wu, H. Zhang, M. Y. Yu, B. Qiao, S. C. Ruan, and X. T. He, *"Interaction features of two ultra-intense laser pulses self-trapped in underdense plasmas,"* AIP Advances **10**, 025313 (2020).